

**Effect of H₂ Pressure on Hydrogen
Absorption and Granular Iron Corrosion
Rates**

by

Emily Bronwyn Taylor

A thesis

presented to the University of Waterloo

in fulfillment of the

thesis requirement for the degree of

Master of Science

in

Earth and Environmental Sciences

Waterloo, Ontario, Canada, 2013

© Emily Bronwyn Taylor 2013

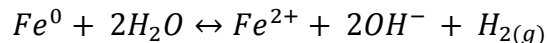
Author's Declaration

I hereby declare that I am the sole author of this thesis. This is a true copy of my thesis, including any required final revisions, as accepted by my examiners.

I understand that my thesis may be made electronically available to the public.

Abstract

Hydrogen gas production occurs in permeable reactive iron barriers (PRBs) due to the anaerobic corrosion of granular iron:



Once produced, this hydrogen gas can have detrimental physical effects on PRB performance. Corrosion-produced hydrogen may accumulate in pore spaces within the PRB, thereby reducing the porosity and permeability. It may also escape the PRB system, representing a lost electron resource that may otherwise be used in reductive remediation reactions. In addition to these physical effects of hydrogen on PRB performance, chemical interactions between hydrogen and iron also occur. Hydrogen may become absorbed by the iron and stored as an electron resource within lattice imperfections. It may also interact with iron surfaces to influence the corrosion rate of the iron. These chemical interactions between hydrogen and iron may impact the reactivity of the iron granules and therefore affect PRB performance. Currently, the chemical effects of hydrogen on PRB performance remain largely unexplored. In this study, the effect of hydrogen on iron reactivity was investigated by considering hydrogen absorption into iron and hydrogen induced changes to iron corrosion rates.

Hydrogen absorption by iron creates a stored electron resource within the iron granules. Release of this stored hydrogen from trapping sites represents an additional electron resource that may be used in contaminant degradation reactions. Therefore, improved hydrogen absorption may contribute to increased iron reactivity. Hydrogen absorption by granular irons has been largely unexplored in PRB performance investigations and the effect of hydrogen absorption on contaminant remediation remains unknown. In this study, an investigation of the factors governing hydrogen absorption by three granular irons, H₂OmetTM56, H₂OmetTM58 and H₂OmetTM86 was conducted. The results demonstrated that rapidly corroding H₂OmetTM86 absorbed hydrogen at a higher *rate* than the other more slowly corroding irons. The presence of an oxide film on H₂OmetTM56 appeared to improve the *proportion* of hydrogen absorption compared to the bare irons. Ultrasonic treatment was explored as potential method of release of trapped hydrogen for improved iron reactivity. Ultrasonic treatment appeared to be unsuccessful

at releasing stored hydrogen from trapping sites, but further investigations into different ultrasound conditions as well as other methods of hydrogen release could prove useful.

Hydrogen gas may also influence iron reactivity by interacting with iron surfaces to alter the corrosion rate of the iron. This may occur by processes such as hydrogen enhanced anodic dissolution, hydrogen induced cracking, enhanced pitting susceptibility and reduction of iron oxides by hydrogen gas. In this study, the effect of hydrogen on iron corrosion rates was assessed by treating two iron materials (H₂OmetTM56 and Connelly) under high pressures of hydrogen for 14 d, then comparing the post-treatment corrosion rates of hydrogen treated irons to the post-treatment corrosion rates of corresponding irons treated under low hydrogen pressures for the same period. The results demonstrated that the post-treatment corrosion rate of high hydrogen treated H₂OmetTM56 iron was lower than the post-treatment corrosion rate of low hydrogen treated H₂OmetTM56 iron. Hydrogen treatment did not appear to affect the post-treatment corrosion rates of Connelly iron. The effect of hydrogen on the corrosion rate of H₂OmetTM56 iron may be a result of hydrogen enhanced anodic dissolution. The presence of a continuous oxide film on Connelly iron appeared to inhibit the effect of hydrogen enhanced anodic dissolution on Connelly iron corrosion rates. The effects of iron oxide reduction by hydrogen and hydrogen induced pitting corrosion were also considered.

Acknowledgements

I first wish to thank my supervisor, Dr. Eric J. Reardon, for his considerable insight and contributions into this work as well as his guidance and support along the way. Your kindness and patience are truly inspirational. Congratulations on an outstanding career and best of luck in your retirement.

I also wish to thank my committee members, Dr. David W. Blowes and Dr. Richard T. Amos, whose suggestions into this work have been extremely helpful and very much appreciated.

Special thanks are extended to Colin Guthrie and Luning Fu for their assistance in navigating the intricacies of graduate studies at the University of Waterloo as well as to Emily Stephenson for her help in conducting iron corrosion experiments.

I also wish to thank my family for their unwavering support throughout my life and my time here at the University of Waterloo. I would not be where I am today had you not always been just a phone call away.

The author also wishes to acknowledge funding for this project provided by NSERC (Natural Sciences and Engineering Research Council of Canada) as well as the generous donation of iron materials by Quebec Metal Powders of Rio Tinto.

Table of Contents

Author's Declaration	ii
Abstract	iii
Acknowledgements	v
List of Tables	viii
List of Figures	ix
1 INTRODUCTION	1
1.1 Background	1
1.2 Thesis Objectives	4
2 HYDROGEN ABSORPTION AND STORAGE	5
2.1 Background	5
2.2 Methods	6
2.2.1 <i>Materials</i>	6
2.2.2 <i>Reaction Apparatus</i>	7
2.2.3 <i>Reaction Procedure</i>	8
2.2.4 <i>Ultrasound Experiments</i>	12
2.3 Results and Discussion	13
2.3.1 <i>H₂OmetTM 56 Iron</i>	13
2.3.2 <i>H₂OmetTM 58 Iron</i>	13
2.3.3 <i>H₂OmetTM 86 Iron</i>	13
2.3.4 <i>Effect of Corrosion Rate on Hydrogen Absorption</i>	16
2.3.5 <i>Effect of Oxide Film on Hydrogen Absorption</i>	23
2.3.6 <i>Ultrasonic Treatment</i>	26
2.4 Conclusion	31
3 EFFECT OF HYDROGEN ON IRON CORROSION RATES	33
3.1 Background	33
3.2 Methods	34
3.2.1 <i>Materials</i>	34
3.2.2 <i>Hydrogen Treatment Experiments</i>	34
3.2.3 <i>Iron Oxidation Experiments</i>	35
3.3 Results and Discussion	36

3.3.1	<i>H₂OmetTM 56 Iron</i>	36
3.3.2	<i>Connelly Iron</i>	38
3.3.3	<i>Scanning Electron Microscope (SEM) Analysis</i>	41
3.3.4	<i>Hydrogen Enhanced Anodic Dissolution</i>	44
3.3.5	<i>Reduction of Iron Oxides</i>	47
3.3.6	<i>Hydrogen Induced Pitting</i>	53
3.3.7	<i>Implications for PRB Design</i>	55
3.4	Conclusion.....	56
4	SUMMARY OF CONCLUSIONS	58
5	RECOMMENDED FUTURE WORK	60
	Appendix A - Materials	61
	Appendix B - Reaction Apparatus	66
	Appendix C - Chapter 2.0 Supplemental Information	71
	Appendix D - Chapter 3.0 Supplemental Information.....	75
	References.....	80

List of Tables

Table 2.1: Summary of H ₂ Omet TM iron surface areas and physical appearances.	7
---	---

List of Figures

Figure 2.1: Example hydrogen pressure curve with discontinuities due to the addition or removal of hydrogen gas.....	9
Figure 2.2: Example apparent rate curve determined from the pressure readings in Figure 2.1 and Equation 2.2. The apparent rate curve only accounts for hydrogen that entered the gas phase and the water phase.....	10
Figure 2.3: Example corrected corrosion rate curve with discontinuities removed using Equation 2.5. The corrected corrosion rate curve accounts for hydrogen entering the gas phase, water phase and absorbed by the hydrogen.	12
Figure 2.4: Corrected and apparent corrosion rate curves for a 300 h corrosion run using H ₂ Omet TM 56 iron. A k value of $0.13 \text{ mmol kg}^{-1} \text{ d}^{-1} \text{ kPa}^{-0.5}$ was used to remove discontinuities from the apparent corrosion rate curve. Approximately 85% of the hydrogen was absorbed into H ₂ Omet TM 56.	14
Figure 2.5: Corrected and apparent corrosion rate curves for a 500 h corrosion run using H ₂ Omet TM 58 iron. A k value of $0.30 \text{ mmol kg}^{-1} \text{ d}^{-1} \text{ kPa}^{-0.5}$ was used to remove discontinuities from the apparent corrosion rate curve. Approximately 30% of the hydrogen was absorbed into H ₂ Omet TM 58.	15
Figure 2.6: Corrected and apparent corrosion rate curves for a 200 h corrosion run using H ₂ Omet TM 86 iron. A k value of $0.39 \text{ mmol kg}^{-1} \text{ d}^{-1} \text{ kPa}^{-0.5}$ was used to remove discontinuities from the apparent corrosion rate curve, however a single k value was not effective at removing all discontinuities. Less than 30% of the hydrogen was absorbed into H ₂ Omet TM 86.	16
Figure 2.7: Relationship between the k value effective at removing a given discontinuity and the corrosion rate immediately before the discontinuity for several discontinuities throughout the three H ₂ Omet TM corrosion rate curves. A strong linear relationship exists between the two values ($R^2 = 0.99$).....	17
Figure 2.8: Proposed relationship between <i>apparent</i> k , k'' , and corrosion rate. Below R_{\min} , hydrogen does not accumulate at iron surfaces and k'' is equal to k . Above R_{\min} hydrogen accumulation results in an increase in k' and therefore an increase in k''	19
Figure 2.9: Comparison of corrosion rate curves and k'' values for each of the H ₂ Omet TM irons over time. k'' is used to represent the rate of hydrogen entry normalized to the ambient pressure in the reaction cell. H ₂ Omet TM 56 demonstrates the lowest rate of hydrogen entry followed by H ₂ Omet TM 58 and H ₂ Omet TM 86 respectively.	22

Figure 2.10: Comparison of hydrogen absorption proportions of H₂OmetTM56, H₂OmetTM58, H₂OmetTM86, Alfa Aesar and Connelly iron. The values were calculated for the irons after 50 h of corrosion. The results demonstrate that the oxidized irons absorb a greater proportion of the produced hydrogen than the pure iron materials..... 24

Figure 2.11: XRD analysis on "as received" H₂OmetTM56, H₂OmetTM58 and H₂OmetTM86 irons demonstrates that H₂OmetTM56 contains magnetite/maghemite while H₂OmetTM58 and H₂OmetTM86 are composed predominately of iron metal..... 25

Figure 2.12: Comparison of corrosion rate curves for low-treated H₂OmetTM56 iron under control conditions (black) and submerged in an ultrasonic water bath (white). The variability in the ultrasound corrosion rate curve is due to temperature fluctuations of the water bath as a result of the cavitation process. The ultrasound corrosion rate curve is significantly (95% confidence) higher than the control corrosion rate curve. 28

Figure 2.13: Comparison of corrosion rate curves for high-treated H₂OmetTM56 iron under control conditions (black) and submerged in an ultrasonic water bath (white). The ultrasound corrosion rate curve is significantly (95% confidence) higher than the control corrosion rate curve..... 29

Figure 2.14: Comparison of the difference between the ultrasound and control corrosion rate curves for low and high hydrogen pressure treated H₂OmetTM56. No significant difference (95% confidence) between the low and high treated samples was observed indicating that ultrasonic treatment did not facilitate hydrogen release. 30

Figure 3.1: Post-treatment corrected and apparent corrosion rate curves for H₂OmetTM56 iron treated under low pressures of hydrogen for 14 d..... 37

Figure 3.2: Post-treatment corrected and apparent corrosion rate curves for H₂OmetTM56 iron treated under high pressures of hydrogen for 14 d. 37

Figure 3.3: Comparison of post-treatment corrected rate curves for low and high treated H₂OmetTM56 iron. The post-treatment corrected corrosion rate of low treated H₂OmetTM iron was a factor of two higher than the post-treatment corrected corrosion rate of high treated H₂OmetTM iron. 38

Figure 3.4: Post-treatment corrected and apparent corrosion rate curves for Connelly iron treated under low pressures of hydrogen for 14 d. 39

Figure 3.5: Post-treatment corrected and apparent corrosion rate curves for Connelly iron treated under high pressures of hydrogen for 14 d. 39

Figure 3.6: Comparison of post-treatment corrected rate curves for low and high treated Connelly iron. No significant difference in the post-treatment corrosion rates of the two samples was observed. 40

Figure 3.7: SEM photographs of low pressure treated H₂OmetTM56 iron (top) and high pressure treated H₂OmetTM56 iron (bottom). The images demonstrate more oxide crystals and the presence of tubercles on the high pressure treated iron indicating that the high treated iron has reached a more advanced stage of iron corrosion than the low pressure treated iron. 41

Figure 3.8: SEM photographs of low pressure treated H₂OmetTM56 iron (top) and high pressure treated H₂OmetTM56 iron (bottom). The images demonstrate a more uniform and extensive oxide film (gray) on the high hydrogen treated iron and more areas of exposed iron metal (white) on the low hydrogen treated iron. 42

Figure 3.9: Comparison of post-treatment corrected corrosion rate curves for low and high treated Alfa Aesar iron following 7 d of treatment at low and high hydrogen pressures. High hydrogen treatment resulted in a decreased post-treatment corrosion rate of Alfa Aesar iron..... 45

Figure 3.10: Comparison of treatment period corrosion rates for Alfa Aesar iron treated at low and intermediate hydrogen pressures. Intermediate hydrogen pressures resulted in a more rapid increase and subsequent decline to lower hydrogen evolution rate than low hydrogen pressures. 46

Figure 3.11: Comparison of Alfa Aesar iron corrected corrosion rate curves for the baseline run with no oxygen addition, X run with 43 mL of oxygen addition and 2X run with 86 mL of oxygen addition. The hydrogen evolution rate increased with increasing oxygen addition and the effect was sustained for at least 200 h of corrosion. 49

Figure 3.12: Comparison of Alfa Aesar iron corrected corrosion rate curves for the X run with 43 mL of oxygen addition and the 2X run with 86 mL of oxygen addition. The hydrogen evolution rate increased with increasing oxygen addition and the effect was sustained for at least 500 h of corrosion. 50

Figure 3.13: The hydrogen evolution rate of the 2X corrosion run above the baseline run was approximately twice the hydrogen evolution rate of the X corrosion run above the baseline run for the entire duration of the 200 h reaction. This indicates no hydrogen consumption by iron oxide reduction..... 52

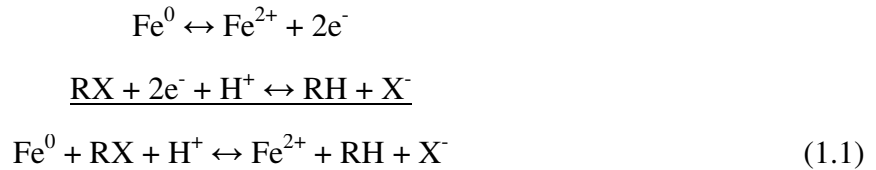
Figure 3.14: Microscope image of low-treated (left) and high-treated (right) Connelly iron. More areas of exposed iron metal are observed on Connelly iron that was treated under high hydrogen pressure conditions than on Connelly iron that was treated under low hydrogen pressure conditions. This is indicative of hydrogen induced pitting corrosion..... 54

1 INTRODUCTION

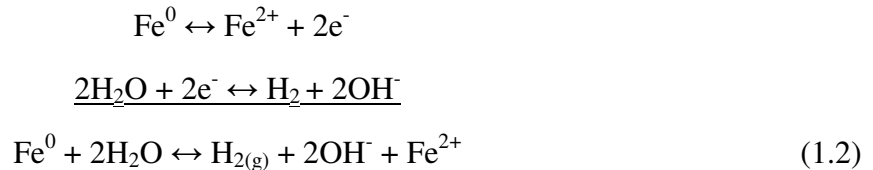
1.1 Background

Remediation of contaminants in groundwater is an environmental challenge due to the intricacies of groundwater flow system characterization and considerable variety of target contaminants involved. Traditional technologies for groundwater remediation consist of pump-and-treat systems in which contaminated water is extracted from the ground and treated at the surface before reinjection. In addition to high capital and operational costs, a study conducted in 1994 determined that 68 of 77 investigated pump-and-treat cleanup sites fell short of remediation goals (National Research Council, 1994). This identified a need for more effective, in-situ approaches to groundwater remediation. The first successful field-scale implementation of a permeable reactive iron barrier (PRB) at the Canadian Forces Base Borden in 1990 introduced PRB technology as a viable and cost-effective alternative for the remediation of a variety of groundwater contaminants (Gillham and O'Hannesin, 1994). Since this time, extensive research has focused on the effectiveness of PRB systems for groundwater treatment (e.g. Blowes et al., 2000, Vogan et al., 1999, O'Hannesin and Gillham, 1998, Cantrell et al., 1995, Matheson and Tratnyek, 1994 and others).

Permeable reactive iron barriers operate on the premise of contaminant reduction by zero-valent iron (ZVI) particles (O'Hannesin and Gillham, 1998, Matheson and Tratnyek, 1994). With a reduction potential of -0.440V for the $\text{Fe}^{2+}/\text{Fe}^0$ redox couple, ZVI is capable of reducing many groundwater contaminants including, but not limited to, dissolved nutrients such as nitrate and sulfate (Robertson et al., 2008, Gandhi et al., 2002) dissolved metals such as Cr, U, and As (Lien et al., 2005, Blowes et al., 2000, Puls et al., 1999a, Cantrell et al., 1995) and chlorinated industrial solvents such as trichloroethene (TCE), dichloroethylene (DCE) and vinyl chloride (VC) (Jeen et al., 2006, Puls et al., 1999b, Vogan et al., 1999). When contaminants come into contact with the PRB, the contaminant is removed by reductive immobilization, precipitation or transformation (Blowes et al., 2000, Matheson and Tratnyek, 1994). A general reaction for the reductive transformation of a chlorinated hydrocarbon is as follows:



In an analogous reaction that is independent of the remediation reaction, iron reduces water molecules according to the following process.



Reaction 1.2 is known as anaerobic iron corrosion. As a result of anaerobic iron corrosion, hydrogen gas is introduced into the PRB.

Hydrogen gas production can impart important changes on PRB performance (Jeen et al., 2012, Amos and Mayer, 2006, Zhang and Gillham, 2005 and others). Corrosion-produced hydrogen may escape the PRB system, representing a lost electron resource that could otherwise be used in remediation reactions. Hydrogen may also accumulate in the PRB, reducing the porosity and permeability. In bench-scale column experiments, it was observed that hydrogen gas produced by iron corrosion could accumulate to 10% of the initial porosity of the column, reducing the hydraulic conductivity by approximately one order of magnitude (Zhang and Gillham, 2005). In field-scale PRBs, decreases in porosity of up to 5% as a result of $\text{H}_{2(\text{g})}$ accumulation have been observed (Henderson and Demond, 2011). In some cases, estimated porosity losses due to hydrogen gas accumulation of as high as 10% to 15% (Mackenzie et al., 1999) and even 20% (Repta, 2001) have been presented.

Although the majority of studies on the effects of hydrogen production on PRB performance have been concerned with the physical effects of hydrogen, hydrogen may also have chemical effects on PRB performance. For decades, scientists have studied the effects of hydrogen on construction materials such as iron and steel (e.g. Oriani, 1993, Iyer and Pickering, 1990, Johnson, 1988, Hirth, 1980) however, with a few notable exceptions (Reardon, 2013, Zhao and Reardon, 2012), it is rare that that this knowledge is applied in permeable reactive barrier design.

One process by which hydrogen gas may influence iron reactivity is by becoming absorbed by the iron, creating a stored electron resource within the iron lattice that may be used in remediation reactions. Although the effects of hydrogen absorption on the strength and ductility of metal construction materials such as iron and steel have been extensively documented in corrosion science literature (Oriani, 1993, Zakroczymski, 1985), hydrogen absorption by granular irons used in PRB applications remains largely unexplored. In Chapter 2, rates and proportions of hydrogen absorption of three granular irons were considered to evaluate factors governing hydrogen absorption by iron. Possible methods of hydrogen release were also investigated.

Hydrogen may also affect PRB performance by altering the corrosion rates of the iron granules. This can occur by hydrogen enhanced anodic dissolution (Yu et al., 2003, Qiao and Luo, 1998), hydrogen induced cracking (Timmins, 1997), hydrogen enhanced pitting corrosion (Schweitzer, 2010) and reduction of surface films (Pineau et al., 2007, Yu et al., 2002). These processes may alter iron corrosion rates by accelerating the iron dissolution reaction, increasing the surface area of the granules, exposing bare iron surfaces or reducing the passivity of the oxide film. The effect of hydrogen on iron corrosion rates was explored in Chapter 3.

1.2 Thesis Objectives

The purpose of this thesis was to investigate potential influences of hydrogen on granular iron reactivity. This was done by evaluating iron corrosion rate curves developed using hydrogen evolution in closed reaction vessels over time. The objectives of this thesis are outlined as follows:

1. Evaluate the factors governing hydrogen absorption by iron and potential methods of release of stored hydrogen.
2. Investigate the effect of hydrogen on the corrosion rates of granular iron materials.

2 HYDROGEN ABSORPTION AND STORAGE

2.1 Background

When hydrogen gas is produced by anaerobic corrosion of iron in PRBs, a portion of the produced gas escapes the PRB. Since escaping hydrogen contains remediation-capable electrons, the removal of hydrogen gas from the PRB represents a lost electron resource that may otherwise be used in reductive remediation reactions (Reardon, 2013). In addition, hydrogen can further affect PRB performance by accumulating in pore spaces, reducing the porosity and permeability of the PRB. However, a portion of the corrosion-produced hydrogen gas is absorbed and stored within the iron at lattice imperfections such as microcracks and crystal boundaries. Hydrogen absorption mitigates the negative physical effects of hydrogen gas production on PRB performance and creates a stored electron resource within the iron that may be used in reductive remediation reactions. The amount of absorbed hydrogen within metals can be substantial. Reardon (2013) estimated that for a typical PRB with a porosity of 40%, density of 7 kg/m^3 , residence time of 1 d and hydrogen entry rate of $0.5 \text{ mmol kg}^{-1} \text{ d}^{-1}$, enough hydrogen is stored within the iron to dechlorinate 220 mg TCE for every litre of groundwater that flows through the PRB. Therefore, hydrogen absorption may have an important effect on iron reactivity and PRB performance.

Hydrogen absorption by metals has been extensively documented in corrosion science literature (Johnson, 1988, Hirth, 1980 and others) due to various effects of hydrogen absorption on common construction materials such as iron and steel (Timmins, 1997). For hydrogen absorption into metals to occur, atomic hydrogen must become adsorbed on the surface of the metal. This occurs by dissociative adsorption ($\frac{1}{2}H_2 + M \leftrightarrow MH_{ads}$) (Sieverts, 1929) or electrochemical deposition ($H_2O + e^- \leftrightarrow H_{ads} + OH^-$) (Peing and Wu, 2003). A portion of this adsorbed hydrogen combines on the metal surface either chemically (Tafel Reaction: $2H_{ads} \leftrightarrow H_2$) or electrochemically (Heyrovsky Reaction: $H_{ads} + H_2O + e^- \leftrightarrow H_2 + OH^-$) to produce hydrogen gas. However, some H_{ads} diffuses into the iron material as absorbed hydrogen ($H_{ads} \leftrightarrow H_{abs}$) (Dafft et al., 1979) and becomes stored at lattice imperfections (Oriani, 1993, Zakroczymski, 1985).

Although the process of hydrogen absorption by metal construction materials is well understood, the factors governing rates and proportions of hydrogen absorption by granular iron materials remain largely unexplored. Since hydrogen absorption may influence granular iron reactivity, the factors governing hydrogen absorption should be considered in PRB design. In this study, factors governing hydrogen absorption by three iron materials, H₂OmetTM56, H₂OmetTM58 and H₂OmetTM86, were evaluated using corrosion rate curves developed from hydrogen evolution rates in closed reaction vessels over time. Ultrasonic treatment as a possible method of hydrogen release was also considered.

2.2 Methods

2.2.1 Materials

Hydrogen absorption by three irons of the H₂OmetTM series produced by Quebec Metal Powders Ltd. (QMP) of Rio Tinto were evaluated. The H₂OmetTM series of irons are high purity granular irons designed for contaminant degradation in PRBs, injection sites or source zone treatment applications. The irons are formed when high purity molten iron is cooled and granulated by use of medium to high-pressure water jets. The granules are then dried, screened and packaged (H₂OmetTM: Groundwater Remediation the Natural Way, 2010). Samples were introduced to the reaction cells "as received" without heat or surface treatment.

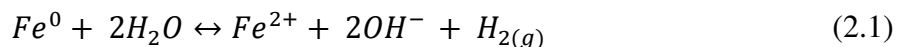
The three irons investigated were H₂OmetTM56, H₂OmetTM58 and H₂OmetTM86. H₂OmetTM56 iron is dark in appearance (Figure A1) and is of intermediate particle size between H₂OmetTM58 and H₂OmetTM86 irons (Table A1). The surface area of H₂OmetTM56 is 0.17 m²/g as determined by multi-point Brunauer-Emmett-Teller (BET) surface area analysis. H₂OmetTM58 is lighter in appearance than H₂OmetTM56 (Figure A2) and has the coarsest particle size (Table A3). The BET surface area of H₂OmetTM58 is 0.079 m²/g. H₂OmetTM86 is the iron with the lightest appearance (Figure A3) and the finest particle size distribution (Table A5). The BET surface area of H₂OmetTM86 iron was determined to be 0.10 m²/g. Chemical compositions of the three materials are included in Table A2, Table A4 and Table A6 for H₂OmetTM56, H₂OmetTM58 and H₂OmetTM86 respectively. H₂OmetTM iron surface areas and physical appearances are summarized in Table 2.1.

Table 2.1: Summary of H₂Omet™ iron surface areas and physical appearances.

	H ₂ Omet™56	H ₂ Omet™58	H ₂ Omet™86
BET Surface Area	0.17 m ² /g	0.079 m ² /g	0.10 m ² /g
Physical Appearance			

2.2.2 Reaction Apparatus

Iron corrosion rates were evaluated by monitoring hydrogen evolution in 150 mL stainless steel reaction vessels over time (Figure B1). Hydrogen evolution can be used as an indicator of corrosion rate due to hydrogen production by the anaerobic iron corrosion reaction.



Stainless steel reaction vessels were chosen for the experiments because stainless steel is resistant to hydrogen absorption (Reardon, 1995, Peden et al., 1986). The reaction cells were outfitted with Swagelok fittings to allow for addition and removal of hydrogen gas, void space determination and pressure measurements which were taken using an Omega PX319-015AV pressure transducer (Figure B2).

Pressure readings were collected using either a LabJack U6-Pro data acquisition (DAQ) board connected to DasyLab software (Figure B3 and Figure B4) or a Strawberry Tree 16 bit data acquisition board connected to WorkBench PC software (Figure B5 and Figure B6). Pressure readings were collected once per minute and reaction cells were immersed in a constant temperature water bath maintained at 25±0.1⁰C for the duration of the experiment (Figure B7).

After the addition of a known quantity of granular iron (M_{Fe}) to the stainless steel reaction vessel, reaction cells were sealed and connected to the DAQ system. The void space (V_{VS}) was

determined in duplicate by evacuating the cells using a Two Stage High Vacuum Pump (Edwards Ltd.) to a reading of 0 ± 1 kPa and adding analytical grade oxygen-free nitrogen gas to atmospheric pressure using a 50 mL dry-sealed syringe. Reaction cells were then removed from the DAQ system and particles were saturated with deionized (DI) water. After ten minutes of saturation, the water was drained and the particles were saturated with 0.002 M $\text{Na}_2\text{B}_4\text{O}_7 \cdot 10\text{H}_2\text{O}$ solution. $\text{Na}_2\text{B}_4\text{O}_7 \cdot 10\text{H}_2\text{O}$ buffer solutions are widely used in studies of iron corrosion because they have the same pH that is established in a pure iron/water system under anaerobic conditions due to saturation with respect to $\text{Fe}(\text{OH})_{2(s)}$ (pH=9.2). Sodium and borate ions do not promote iron corrosion, so $\text{Na}_2\text{B}_4\text{O}_7 \cdot 10\text{H}_2\text{O}$ solutions provide a stable, representative pH of an iron/water system in long term corrosion tests. After two 10 min treatments with $\text{Na}_2\text{B}_4\text{O}_7 \cdot 10\text{H}_2\text{O}$ solution, excess solution was flushed from the cell by connecting the cell to a nitrogen supply and draining the solution from an opening at the bottom of the cell. The remaining water in the cell ($M_{\text{H}_2\text{O}}$) was determined gravimetrically. The cells were reconnected to the DAQ system and reevacuated. This marked the beginning of the corrosion reaction.

2.2.3 Reaction Procedure

Hydrogen pressure measurements were collected for the duration of the corrosion reaction to produce a curve of hydrogen pressure over time. An example hydrogen pressure curve is shown in Figure 2.1. Discontinuities in the pressure curve were created by the addition or removal of hydrogen gas throughout the corrosion reaction. The purpose of the discontinuities is addressed later in this section.

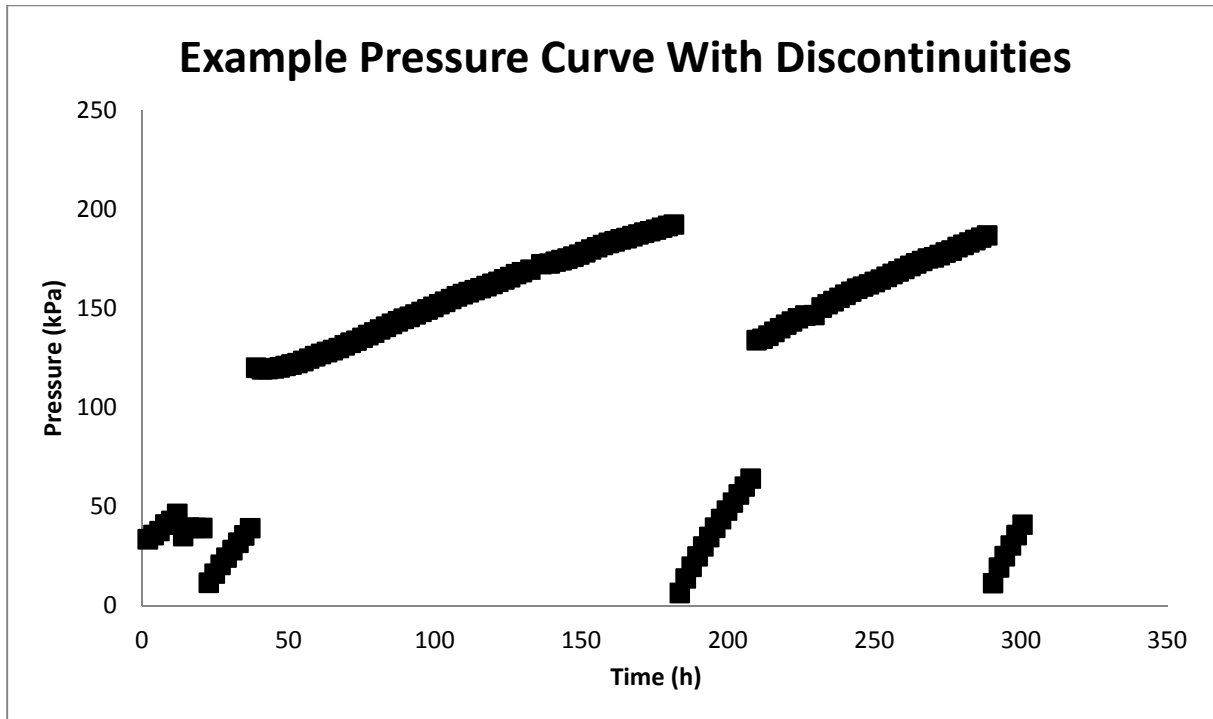


Figure 2.1: Example hydrogen pressure curve with discontinuities due to the addition or removal of hydrogen gas.

From the hydrogen pressure readings, an *apparent corrosion rate* curve was developed using Equation 2.2.

$$R_{app} = 10^3 \left[\frac{V_g}{RT} (P_{H_2(T_2)} - P_{H_2(T_1)}) + K_H M_{H_2O} (P_{H_2(T_2)} - P_{H_2(T_1)}) \right] / [M_{Fe} (T_2 - T_1)] \quad (2.2)$$

Where V_g is the volume of the void space, K_H is Henry's law constant for hydrogen in water, M_{H_2O} is the mass of the water and M_{Fe} is the mass of the iron. An example apparent rate curve is shown in Figure 2.2.

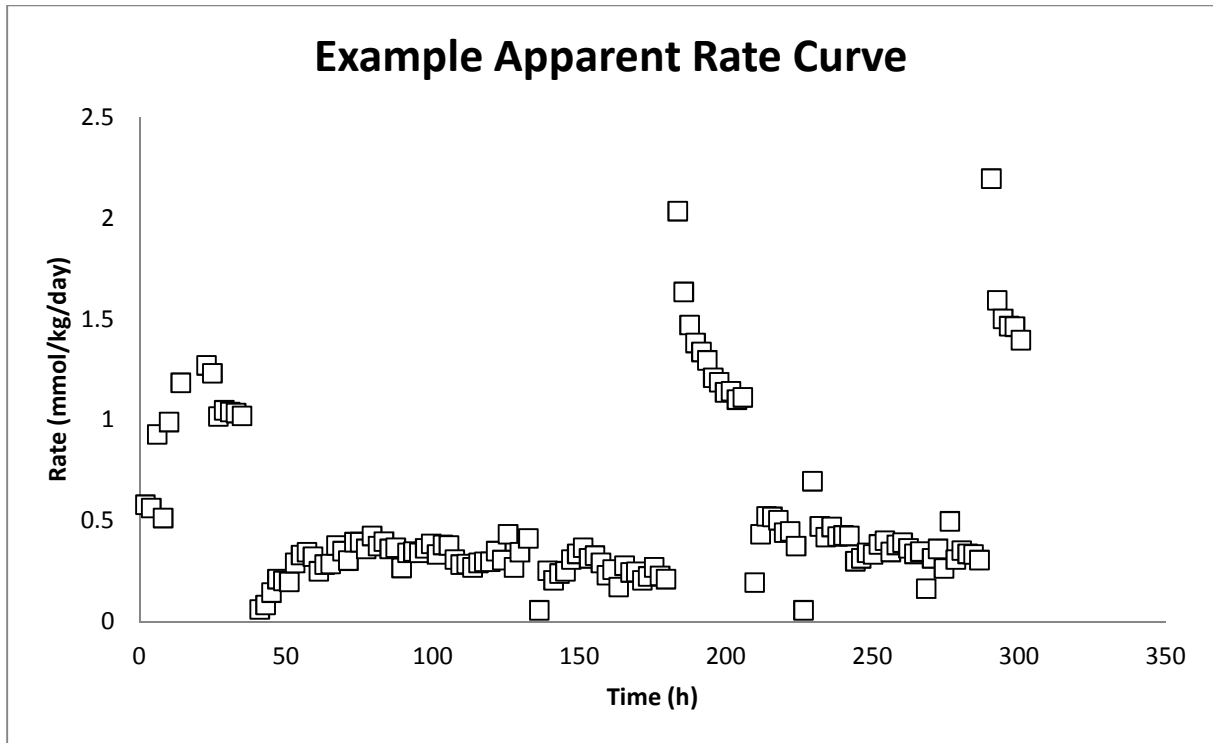


Figure 2.2: Example apparent rate curve determined from the pressure readings in Figure 2.1 and Equation 2.2. The apparent rate curve only accounts for hydrogen that entered the gas phase and the water phase.

The apparent rate curve accounts for hydrogen entering the gas phase, from the first term in Equation 2.2 which is based on the ideal gas law, and hydrogen entering the water phase, from the second term in Equation 2.2 which is based on Henry's law. However, during hydrogen production at iron surfaces, a portion of the corrosion-produced hydrogen enters the iron lattice. This absorbed hydrogen is not accounted for in the apparent corrosion rate curve.

The discontinuities in the pressure curve created by the addition or removal of hydrogen to or from the reaction cell were used to account for the hydrogen that entered the iron lattice as follows. According to a variation of Sieverts' law (Sieverts, 1929), the rate of hydrogen absorption by metals exhibits a square root dependence on the ambient hydrogen pressure (Equation 2.3).

$$R_{entry} = kP_{H_2}^{0.5} \quad (2.3)$$

Therefore, if hydrogen gas is removed from the reaction cell, the pressure of hydrogen in the cell decreases as does the rate of hydrogen absorption into the iron. The decreased rate of hydrogen absorption into the iron causes more hydrogen to enter the gas and water phases and therefore results in an increased apparent corrosion rate. Conversely, if hydrogen gas is added to the reaction cell, the pressure of the cell increases resulting in an increased rate of hydrogen entry into the iron. This produces a decrease in the apparent rate curve. The response of the hydrogen entry rate into iron samples by these pressure changes is immediate resulting in the development of sharp discontinuities in the apparent corrosion rate curve.

Since the overall corrosion of the iron is independent of the reaction cell pressure, the overall rate of hydrogen production is uniform. Therefore, by considering all of the hydrogen produced, including hydrogen that entered the gas phase, water phase and the iron lattice, the discontinuities in the apparent rate curve can be removed and a smooth corrosion rate curve can be established. The total rate of hydrogen production is equal to the apparent corrosion rate, which accounts for hydrogen entering the gas phase and water phase, plus the rate of hydrogen absorption by the iron (Equation 2.4). Since the rate of hydrogen absorption by the iron is equal to $kP_{H_2}^{0.5}$, Equation 2.5 was used to remove discontinuities from the apparent corrosion rate curve.

$$R_{corr} = R_{app} + R_{entry} \quad (2.4)$$

$$R_{corr} = R_{app} + kP_{H_2}^{0.5} \quad (2.5)$$

The removal of discontinuities in the apparent rate curve was achieved using Equation 2.5 by substituting different k values using a trial and error approach until the rate curve was smooth. Student's t-tests were used to determine whether the trial and error approach was a valid method for selecting k values. Once the k value that removed the discontinuity was selected, 12 corrosion rate measurements 5 minutes apart were taken from before and after the discontinuity. Due to degassing of hydrogen from the water phase immediately following the evacuation, values within the first two hours following the discontinuity were not included. Using these values, independent average corrosion rates were calculated for before and after the discontinuity. A Student's t-test determined whether the two values were significantly different. This approach was used for the first discontinuity presented in Table C1 for each of the three H₂Omet™ irons. The results of the Student's t-tests are included in Appendix C. In all cases, the Student's t-tests

revealed that the values were not significantly different. Therefore, trial and error was considered to be a valid method for the removal of discontinuities from the apparent corrosion rate curves.

With the proper k value chosen and the discontinuities removed, the curve was referred to as a *corrected corrosion rate curve*. An example corrected corrosion rate curve is shown in Figure 2.3.

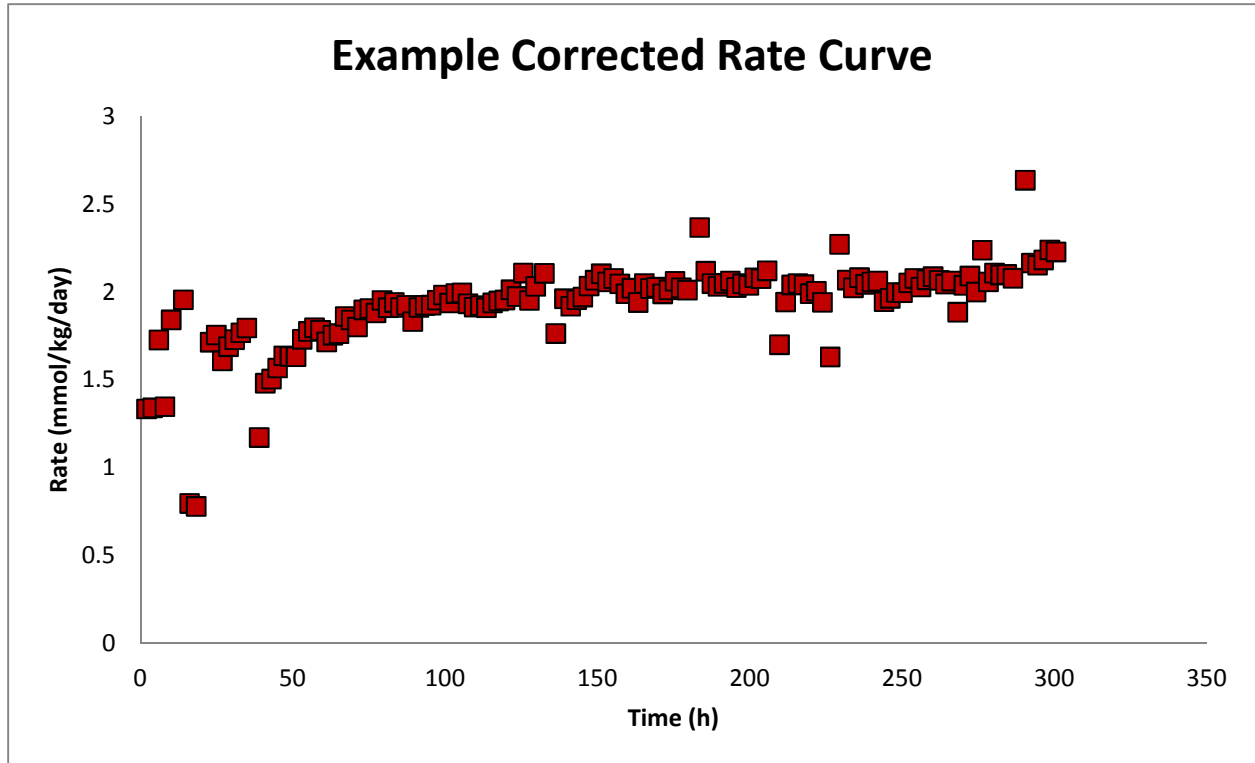


Figure 2.3: Example corrected corrosion rate curve with discontinuities removed using Equation 2.5. The corrected corrosion rate curve accounts for hydrogen entering the gas phase, water phase and absorbed by the hydrogen.

Once the apparent corrosion rate curve and the corrected corrosion rate curve were developed, the area under the apparent corrosion rate curve represented the hydrogen that entered the gas and aqueous phases and the area under the corrected corrosion rate curve represented the total hydrogen generated. Therefore, the hydrogen absorbed into the iron was approximated from the area between the two curves.

2.2.4 *Ultrasound Experiments*

To determine if ultrasonic treatment can release stored hydrogen from lattice imperfections such as microcracks and crystal boundaries, experiments were conducted to compare measured

hydrogen evolution in a control reaction cell to hydrogen evolution in a corresponding reaction cell that was exposed to ultrasonic treatment. Ultrasonic treatment consisted of suspending the cells in a Branson 5200 ultrasonic bath and running the bath on 30 min intervals. After each interval the bath was emptied and refilled with DI water to return the bath to 25⁰C as quickly as possible.

2.3 Results and Discussion

Corrosion rate curves for H₂OmetTM56, H₂OmetTM58 and H₂OmetTM86 irons were established using hydrogen evolution rates in closed reaction vessels over time.

2.3.1 H₂OmetTM56 Iron

The H₂OmetTM56 corrosion rate curve is shown in Figure 2.4. A k value of 0.13 mmol kg⁻¹ d⁻¹ kPa^{-0.5} removed the discontinuities from the apparent rate curve. The corrected corrosion rate of H₂OmetTM56 iron reached a steady-state value of approximately 2 mmol kg⁻¹ d⁻¹ after 50 h and remained constant for the remainder of the 200 h corrosion experiment. The corrosion rate of H₂OmetTM56 iron was the lowest of the three irons studied. This is likely due to the presence of an oxide film on H₂OmetTM56 iron as revealed by X-ray diffraction (XRD) analysis (see Figure 2.11). Using the area under the corrected rate curve to represent the total hydrogen produced and the area under the apparent rate curve to represent the hydrogen that entered the gaseous and aqueous phases, it was determined that H₂OmetTM56 iron absorbed approximately 85% of the produced hydrogen.

2.3.2 H₂OmetTM58 Iron

The H₂OmetTM58 corrosion rate curve is shown in Figure 2.5. A k value of 0.30 mmol kg⁻¹ d⁻¹ kPa^{-0.5} removed the discontinuities from the apparent rate curve. The corrected corrosion rate of H₂OmetTM58 iron increased to approximately 10 mmol kg⁻¹ d⁻¹ after 100 h before declining to a steady-state corrosion rate of approximately 7.5 mmol kg⁻¹ d⁻¹ by 500 h. The corrosion rate of H₂OmetTM58 was intermediate between the three irons studied. H₂OmetTM58 iron absorbed approximately 30% of the produced hydrogen, far less than H₂OmetTM56 iron.

2.3.3 H₂OmetTM86 Iron

The H₂OmetTM86 corrosion rate curve is shown in Figure 2.6. A k value of 0.39 mmol kg⁻¹ d⁻¹ kPa^{-0.5} removed discontinuities from the early time (t<50 h) apparent rate curve however a single

k value was not effective at removing discontinuities from the entire rate curve. A k value of $1.0 \text{ mmol kg}^{-1} \text{ d}^{-1} \text{ kPa}^{-0.5}$ was required to remove later time discontinuities. The inability of a single k value to remove discontinuities from a changing corrosion rate curve is due to a relationship between k and corrosion rate. This relationship is discussed in Section 2.3.4. Using a k value of $0.39 \text{ mmol kg}^{-1} \text{ d}^{-1} \text{ kPa}^{-0.5}$, the corrected corrosion rate of $\text{H}_2\text{Omet}^{\text{TM}}86$ iron increased to above $30 \text{ mmol kg}^{-1} \text{ d}^{-1}$ by 200 h. In addition to demonstrating the highest corrosion rate of the $\text{H}_2\text{Omet}^{\text{TM}}$ irons, $\text{H}_2\text{Omet}^{\text{TM}}86$ demonstrated unique corrosion behaviour in which the corrosion rate increased, plateaued, then continued to increase rapidly for the duration of the corrosion experiment. The high corrosion rate of $\text{H}_2\text{Omet}^{\text{TM}}86$ may be attributed to the fine particle size distribution and absence of an initial oxide film on the iron. The unique corrosion behaviour may be attributed to an accelerating effect of hydrogen on the corrosion rate of the iron. The effect of hydrogen on iron corrosion rates is discussed in detail in Chapter 3. $\text{H}_2\text{Omet}^{\text{TM}}86$ iron absorbed less than 30% of the produced hydrogen gas, the least of the three irons.

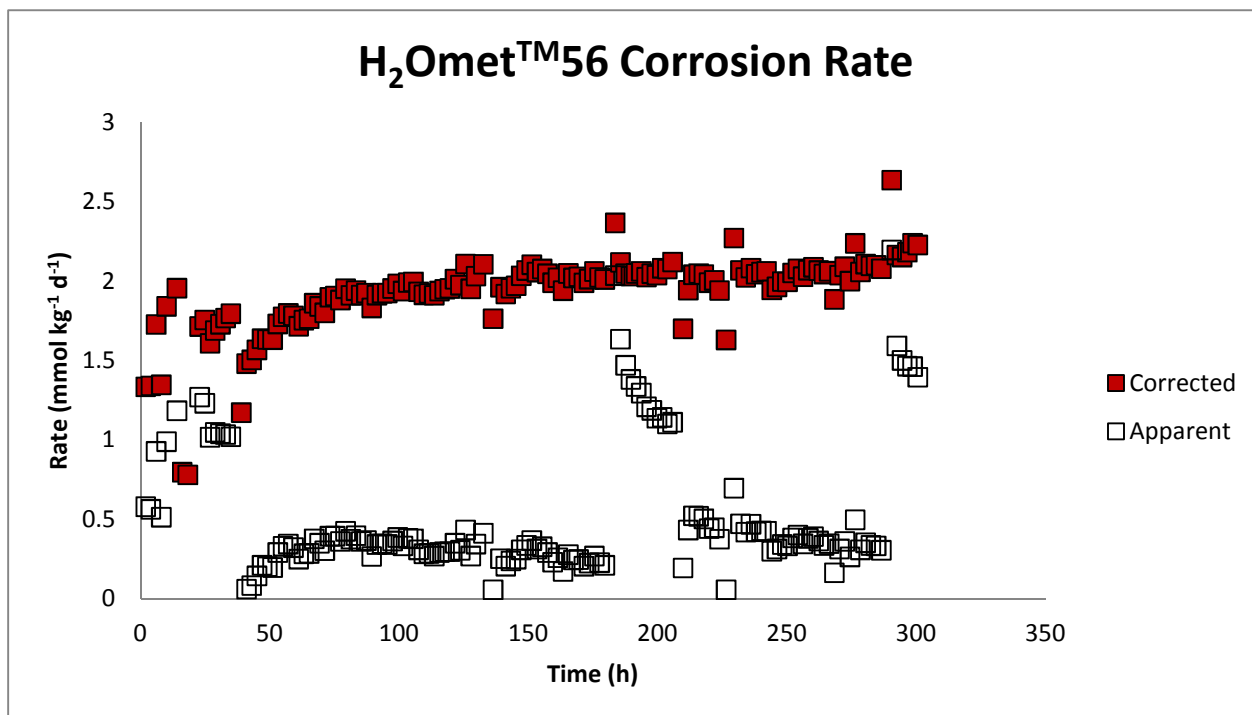


Figure 2.4: Corrected and apparent corrosion rate curves for a 300 h corrosion run using $\text{H}_2\text{Omet}^{\text{TM}}56$ iron. A k value of $0.13 \text{ mmol kg}^{-1} \text{ d}^{-1} \text{ kPa}^{-0.5}$ was used to remove discontinuities from the apparent corrosion rate curve. Approximately 85% of the hydrogen was absorbed into $\text{H}_2\text{Omet}^{\text{TM}}56$.

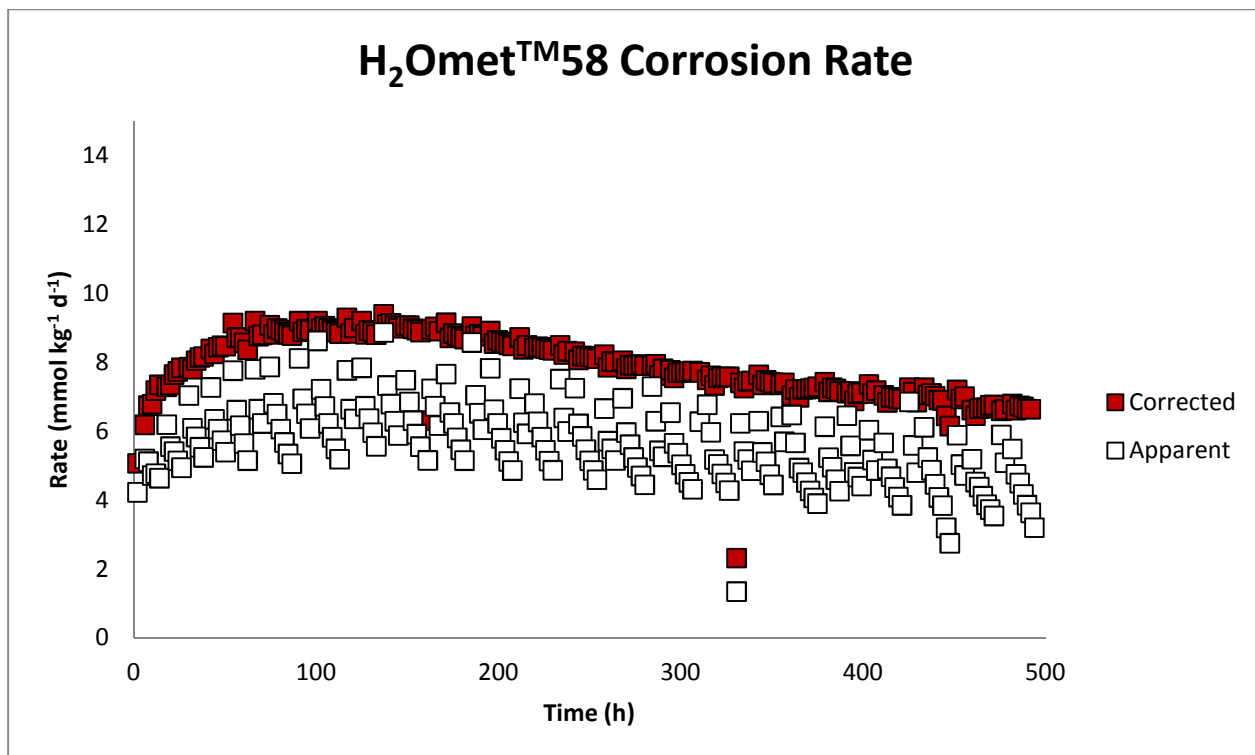


Figure 2.5: Corrected and apparent corrosion rate curves for a 500 h corrosion run using H₂Omet™58 iron. A k value of $0.30 \text{ mmol kg}^{-1} \text{ d}^{-1} \text{ kPa}^{-0.5}$ was used to remove discontinuities from the apparent corrosion rate curve. Approximately 30% of the hydrogen was absorbed into H₂Omet™58.

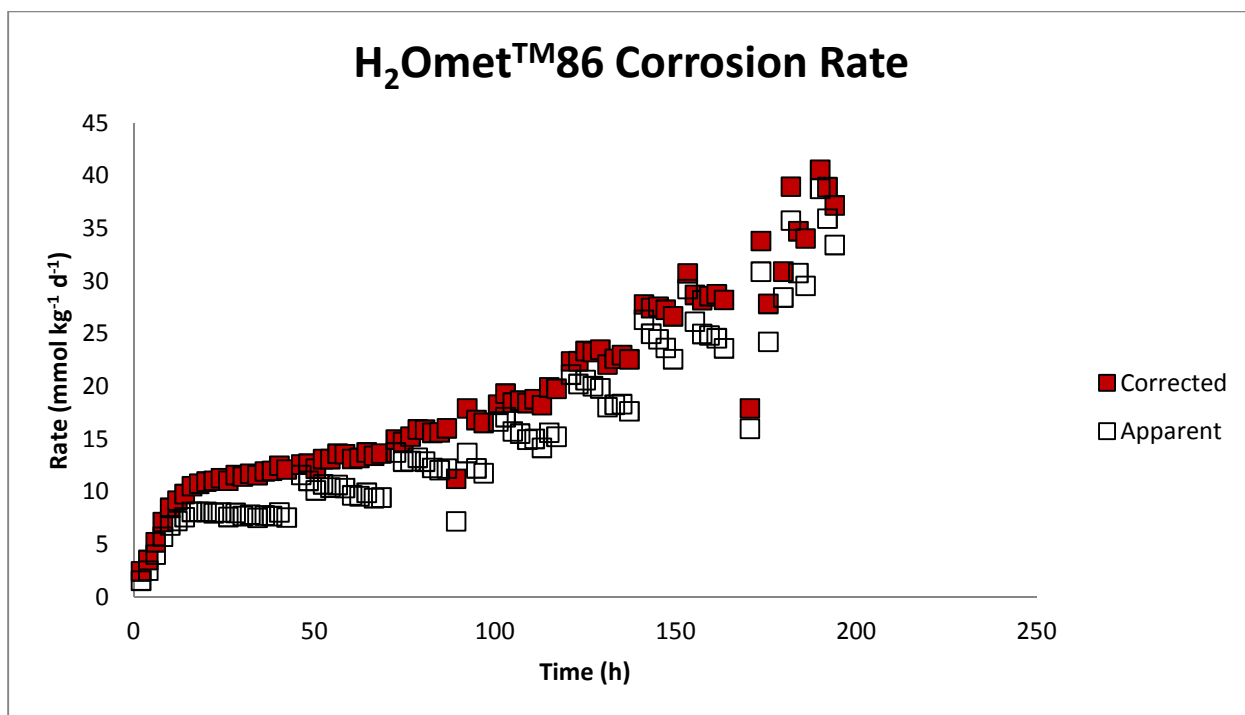


Figure 2.6: Corrected and apparent corrosion rate curves for a 200 h corrosion run using H₂OmetTM86 iron. A k value of $0.39 \text{ mmol kg}^{-1} \text{ d}^{-1} \text{ kPa}^{-0.5}$ was used to remove discontinuities from the apparent corrosion rate curve, however a single k value was not effective at removing all discontinuities. Less than 30% of the hydrogen was absorbed into H₂OmetTM86.

2.3.4 Effect of Corrosion Rate on Hydrogen Absorption

When removing discontinuities from the H₂OmetTM86 apparent corrosion rate curve, it was noted that a single k value was not effective at removing all discontinuities. In general, discontinuities during higher corrosion rates required larger k values than discontinuities during lower corrosion rates.

To evaluate the relationship between k and corrosion rate, the k values effective at removing a discontinuity were plotted against the corrected corrosion rate immediately before the discontinuity for several discontinuities throughout the three H₂OmetTM corrosion rate curves. The corrosion rate before the discontinuity is more representative of the actual corrosion rate of the iron than the corrosion rate after the discontinuity because when hydrogen is removed from a reaction cell to create a discontinuity, rapid diffusion of hydrogen gas out of the water phase causes the corrosion rate to very briefly appear higher than the actual value (Reardon, 1995). For H₂OmetTM56, one discontinuity was chosen because one constant corrosion rate continued over the duration of the H₂OmetTM56 reaction. For H₂OmetTM58, values were obtained from three

discontinuities to represent three areas of distinctly different corrosion rates (early time, peak corrosion rate and late time). For H₂OmetTM86 iron, it was possible to obtain values from six discontinuities with different corrosion rates due to the rapidly changing corrosion rate of H₂OmetTM86 over the duration of the reaction. The *k* and corrosion rate values are provided in Table C1. Figure 2.7 shows that the relationship between *k* and corrosion rate is linear ($R^2 = 0.990$).

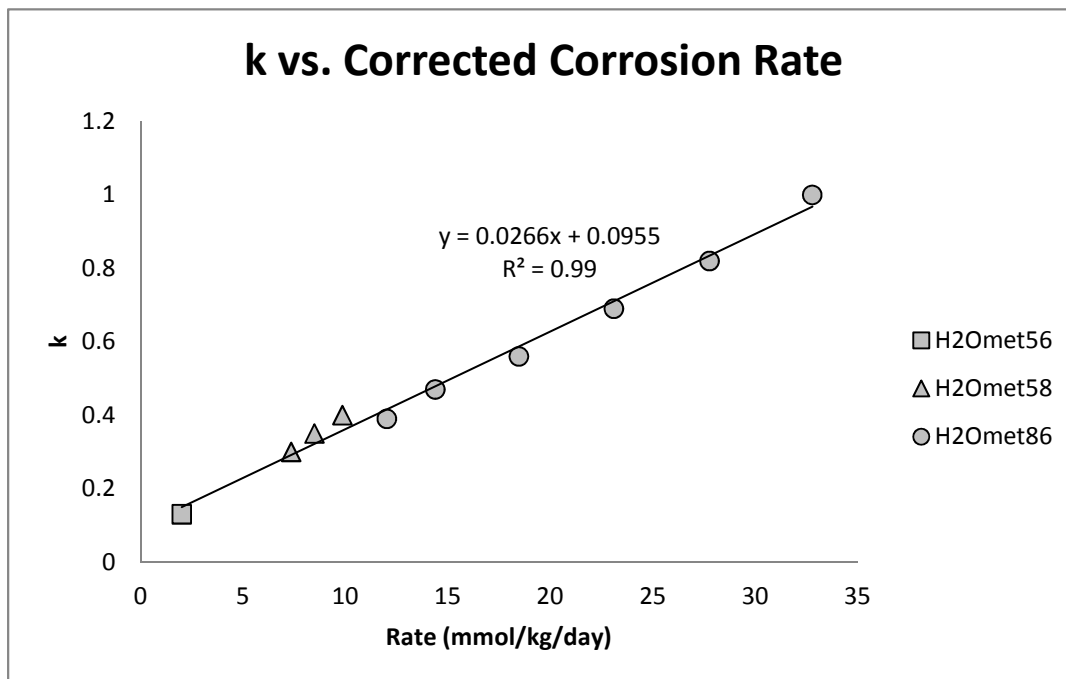


Figure 2.7: Relationship between the *k* value effective at removing a given discontinuity and the corrosion rate immediately before the discontinuity for several discontinuities throughout the three H₂OmetTM corrosion rate curves. A strong linear relationship exists between the two values ($R^2 = 0.99$).

All of the H₂OmetTM irons appear to follow a similar relationship. To evaluate whether this relationship is generally applicable to many irons, possible causes for the relationship were considered. One possible explanation for the increasing value of *k* with increasing corrosion rate is accumulation of hydrogen gas at iron surfaces. When the rate of hydrogen production exceeds the rate at which hydrogen can diffuse away from the iron surface, hydrogen accumulates at the surface of the granules, resulting in higher effective pressures at iron surfaces. Since the rate of hydrogen absorption is related to the square root of the hydrogen pressure (Equation 2.3), higher pressures at iron surfaces result in higher rates of hydrogen absorption. Higher rates of hydrogen

absorption are obtained from Equation 2.3 by substituting higher k values. Therefore, as corrosion rate increases, hydrogen accumulates at iron surfaces causing an increase in the rate of hydrogen absorption which is observed as an increase in the value of k .

However, k is an intrinsic property of the iron determined by the physicochemical characteristics such as method of production, milling history, number of lattice defects and properties of the oxide film (Reardon, 2013). Therefore, k should be a constant value, independent of corrosion rate. The observed relationship between k and corrosion rate is actually an artifact of using k to compensate for underestimation of the effective hydrogen pressures at iron surfaces. The ambient pressure at the pressure transducer is used in Equation 2.3 to calculate the rate of hydrogen entry, and since the pressure transducer does not detect pressure changes occurring at iron surfaces, accumulated effective hydrogen pressures are not considered in the calculation. These increased effective pressures are compensated for by increasing the value of k . Therefore, the k value used in Equation 2.3 is more accurately described as an *apparent* k value (k'') that is a combination of the intrinsic properties of the iron (k) and a correction factor (k') that accounts for accumulation of hydrogen at iron surfaces ($k'' = k + k'$).

Some of the features of the relationship between k'' and corrosion rate are shown in Figure 2.8. One such feature is R_{\min} , the minimum corrosion rate for which the relationship is valid. Below R_{\min} , the rate of hydrogen production is lower than the rate of hydrogen diffusion away from the iron granule so hydrogen accumulation does not occur. Since k' accounts for hydrogen accumulation, below R_{\min} k' is negligible and so k'' is equal to k . Since k is a constant, intrinsic property of the iron, below R_{\min} a zero-slope relationship exists between k'' and corrosion rate. As corrosion rate increases above R_{\min} , the rate of hydrogen production exceeds the rate of hydrogen diffusion and hydrogen begins to accumulate at the iron surface. This causes the correction factor, k' , to increase, producing the observed positive relationship between k'' and corrosion rate.

Because the rate of increase of k' is due to accumulated hydrogen at the iron surface, and not due to the intrinsic properties of the iron, the rate of increase should be consistent between irons. However, the magnitude of k is governed by the intrinsic properties of the iron, so a vertical shift in the relationship should occur between irons with different k values. No vertical shift was

observed between the three H₂OmetTM irons as all irons fell along the same linear regression line (Figure 2.7). However, all of the H₂OmetTM irons were formed by a similar manufacturing process (H₂OmetTM: Groundwater Remediation the Natural Way, 2010) and therefore may have similar intrinsic k values. Figure 2.8 illustrates this concept with the black line representing one iron and the gray line representing another iron with a different k value. Both irons demonstrate the same rate of increase of k'' with increasing corrosion rate, but the irons are vertically shifted due to differing intrinsic k values.

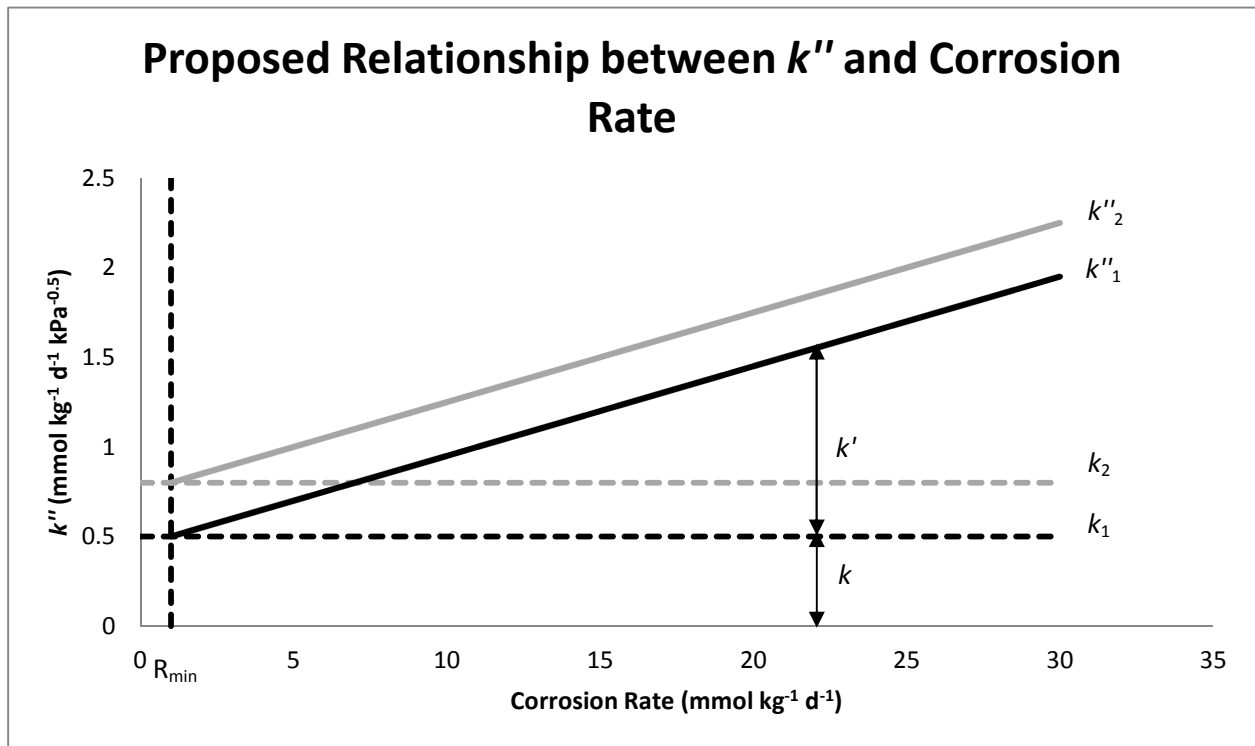


Figure 2.8: Proposed relationship between *apparent* k , k'' , and corrosion rate. Below R_{\min} , hydrogen does not accumulate at iron surfaces and k'' is equal to k . Above R_{\min} hydrogen accumulation results in an increase in k' and therefore an increase in k'' .

A general equation capable of removing discontinuities from the H₂OmetTM apparent rate curves was developed using the relationship in Figure 2.7 and the concepts illustrated in Figure 2.8. The relationship was developed beginning with Equation 2.6, the regression line from Figure 2.7, setting the equation equal to the *apparent* k value, referred to as k'' . Then, k was substituted as the y-intercept to account for the vertical shift in the relationship resulting from the different k values of different irons. R_{\min} was also incorporated to account for the horizontal shift in the relationship that is caused by hydrogen accumulation beginning at the minimum corrosion rate at

which the rate of hydrogen production exceeds the rate of hydrogen diffusion away from the iron surface.

$$k'' = 0.0266 \cdot R_{corr} + 0.0955 \quad (2.6)$$

$$k'' = 0.0266 \cdot (R_{corr} - R_{min}) + k \quad (2.7)$$

By substituting Equation 2.7 for k in Equation 2.5 ($R_{corr} = R_{app} + kP_{H_2}^{0.5}$) and assuming R_{min} is small, a simplified equation (Equation 2.8) was obtained. The assumption that R_{min} is small is reasonable because H₂OmetTM56 plots along the k'' versus corrosion rate regression line in Figure 2.7. Therefore, 2 mmol kg⁻¹ d⁻¹ is larger than R_{min} because it plots along the increasing linear relationship and not the zero-slope relationship that exists below R_{min} . Because R_{min} is smaller than 2 mmol kg⁻¹ d⁻¹, and 2 mmol kg⁻¹ d⁻¹ is small compared to the corrosion rates in Figure 2.7, it is reasonable to assume that R_{min} is small. R_{min} is likely that R_{min} is smaller than 2 mmol kg⁻¹ d⁻¹ however further research is required to determine the actual value of R_{min} . The simplified Equation 2.8 is as follows.

$$R_{corr} = R_{app} + (0.0266 \cdot R_{corr} + k)P_{H_2}^{\frac{1}{2}} \quad (2.8)$$

Rearranging Equation 2.8 for R_{corr} results in Equation 2.9.

$$R_{corr} = \frac{R_{app} + kP_{H_2}^{\frac{1}{2}}}{1 - 0.0266 \cdot P_{H_2}^{\frac{1}{2}}} \quad (2.9)$$

Equation 2.9 follows a similar form to Equation 2.10 which was proposed by Reardon (2005) as a possible improvement to the original Equation 2.5.

$$R_{corr} = \frac{R_{app} + kP_{H_2}^{\frac{1}{2}}}{1 - \alpha} \quad (2.10)$$

Equation 2.9 was used to remove the discontinuities from the H₂OmetTM corrosion rate curves. The corrected corrosion rate curves are shown in Figure 2.9. For H₂OmetTM56 and H₂OmetTM58, Equation 2.9 removed discontinuities as effectively as Equation 2.5. For H₂OmetTM86, Equation 2.9 significantly improved the removal of discontinuities from the apparent corrosion rate curve. For all of the H₂OmetTM irons, a k value of 0.08 mmol kg⁻¹ d⁻¹ kPa^{-0.5} was used. A common k value between the H₂OmetTM irons explains the observation that all of the H₂OmetTM irons followed a similar k versus corrosion rate relationship (Figure 2.7). Further research is required to determine whether Equation 2.9 applies generally to many iron materials, however the equation is valid for the three H₂OmetTM irons studied.

Presented alongside the corrected corrosion rate curves in Figure 2.9 are corresponding plots of k'' versus time for each of the H₂OmetTM irons. Equation 2.6 was used to calculate the value of k'' in these plots. Since the rate of hydrogen absorption is directly related to k (or k'') and the reaction cell pressure (Equation 2.3), these plots represent the rate of hydrogen absorption normalized to the pressure in the reaction cell. The importance of normalizing hydrogen absorption to the reaction cell pressure is discussed in more detail in the following section. Figure 2.9 shows that H₂OmetTM56 iron, the iron with the lowest corrosion rate, absorbed hydrogen at the lowest rate. H₂OmetTM86 iron, the iron with the highest corrosion rate, absorbed hydrogen at the highest rate. The corrosion rate of H₂OmetTM58 was intermediate between the other two irons as was its hydrogen absorption rate. In general, the rate of hydrogen absorption appears to be related to the overall corrosion rate of the iron.

The lower hydrogen absorption *rate* of H₂OmetTM56 iron does not contradict the findings in Section 2.3.1 that H₂OmetTM56 iron absorbed the highest *proportion* of corrosion-produced hydrogen. The factors governing *proportions* of hydrogen absorption by the H₂OmetTM irons are considered in the following section.

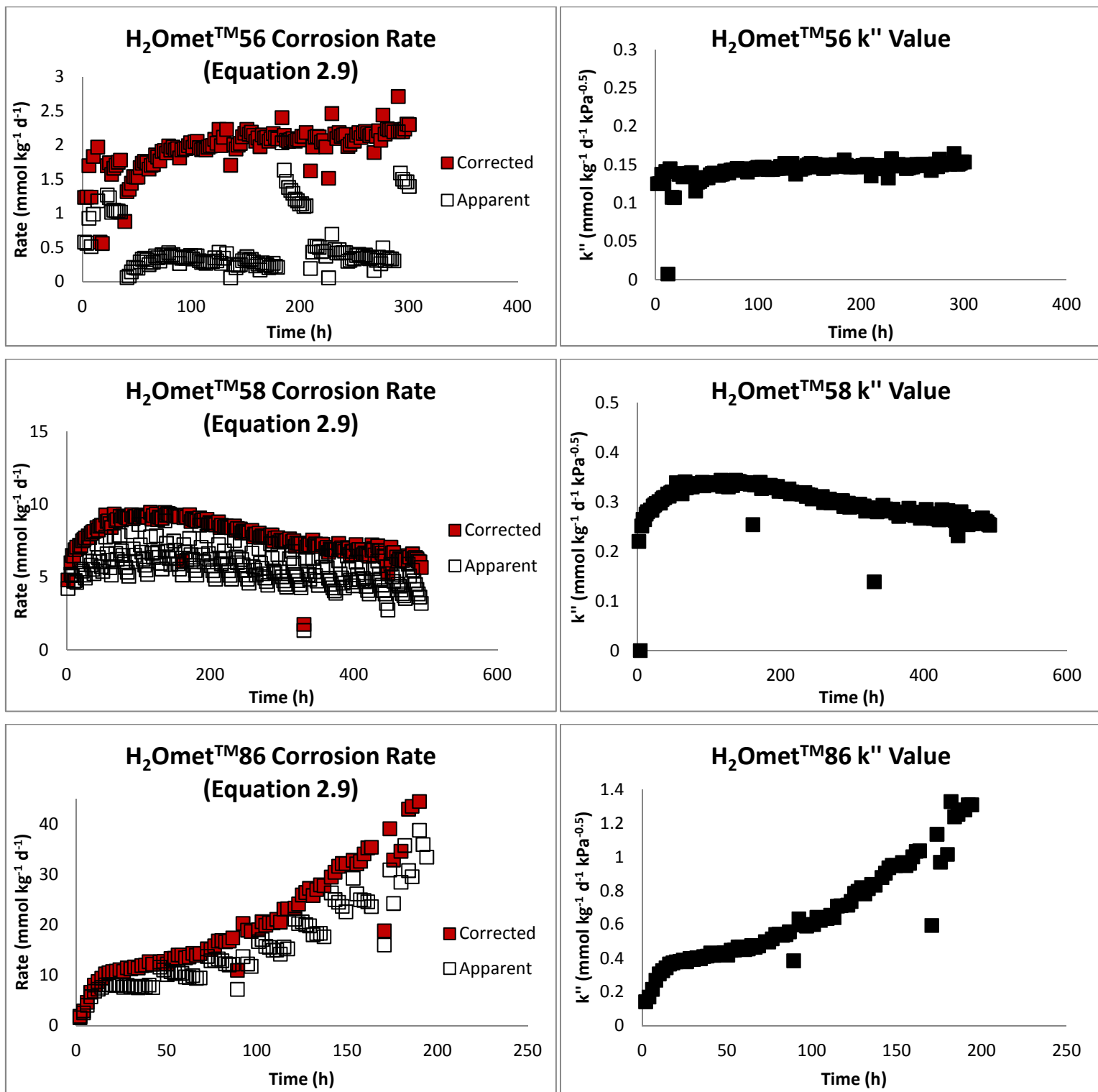


Figure 2.9: Comparison of corrosion rate curves and k'' values for each of the H₂Omet™ irons over time. k'' is used to represent the rate of hydrogen entry normalized to the ambient pressure in the reaction cell. H₂Omet™56 demonstrates the lowest rate of hydrogen entry followed by H₂Omet™58 and H₂Omet™86 respectively.

2.3.5 Effect of Oxide Film on Hydrogen Absorption

In Section 2.3.4, the *rate* of hydrogen absorption was found to be related to the overall corrosion rate of the iron. Factors governing the *proportion* of corrosion-produced hydrogen absorbed by the iron lattice are evaluated in this section.

Hydrogen proportions were calculated using the ratio of the rate of hydrogen absorption to the total rate of hydrogen production (Equation 2.12). However, the rate of hydrogen absorption depends on the ambient pressure in the reaction cell (Equation 2.3), and because different corrosion reactions have different reaction cell pressures over time, comparison of the proportions of hydrogen absorption between irons must be normalized to reaction cell pressure. To normalize the proportion of hydrogen absorption to pressure, it is convenient to choose unit pressure (1 kPa). Then the hydrogen absorption proportion reduces to the ratio of k and the total rate of hydrogen production (R_{corr}) as shown in Equation 2.12.

$$Proportion\ Entry = \frac{R_{entry}}{R_{corr}} = \frac{kP_{H_2}^{\frac{1}{2}}}{R_{corr}} = \frac{k}{R_{corr}} \quad (2.12)$$

Hydrogen absorption proportions for five irons were determined by taking the k value effective at removing the first discontinuity divided by the corrosion rate immediately before the first discontinuity. The results are shown in Figure 2.10.

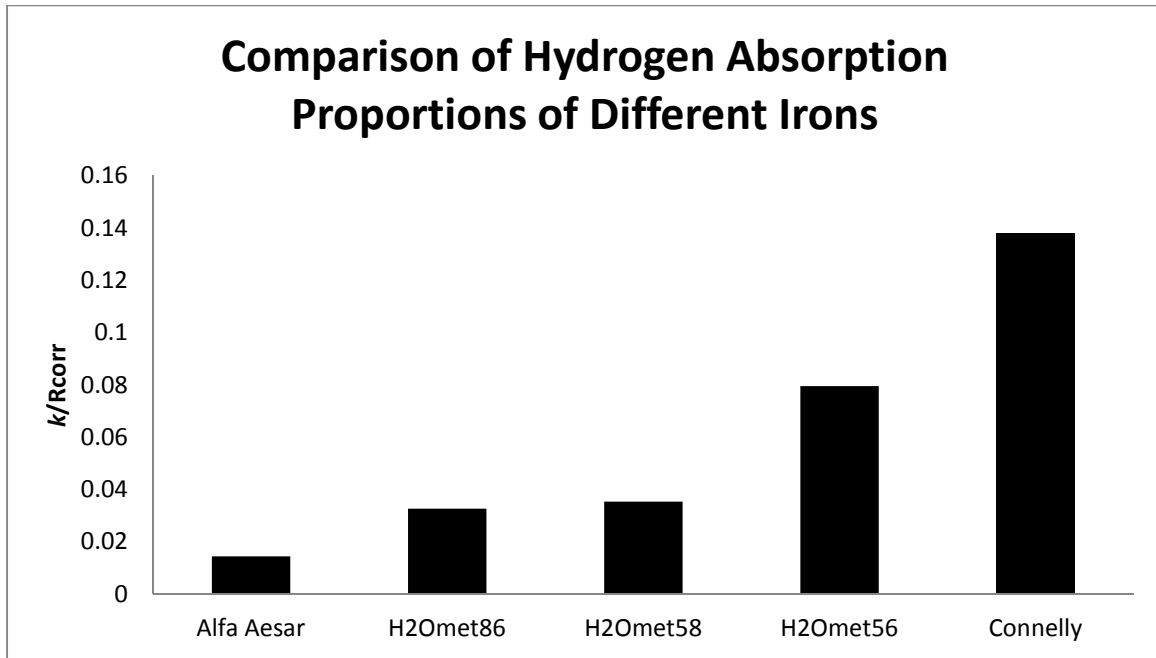


Figure 2.10: Comparison of hydrogen absorption proportions of H₂OmetTM56, H₂OmetTM58, H₂OmetTM86, Alfa Aesar and Connelly iron. The values were calculated for the irons after 50 h of corrosion. The results demonstrate that the oxidized irons absorb a greater proportion of the produced hydrogen than the pure iron materials.

Of the H₂OmetTM irons, the hydrogen absorption proportion of H₂OmetTM56 iron is higher than the hydrogen absorption proportions of H₂OmetTM58 and H₂OmetTM86. X-ray diffraction (XRD) analysis on the “as received” H₂OmetTM irons revealed that H₂OmetTM56 contained sizeable amounts of magnetite/maghemite while the other two irons were predominately composed of iron metal (Figure 2.11).

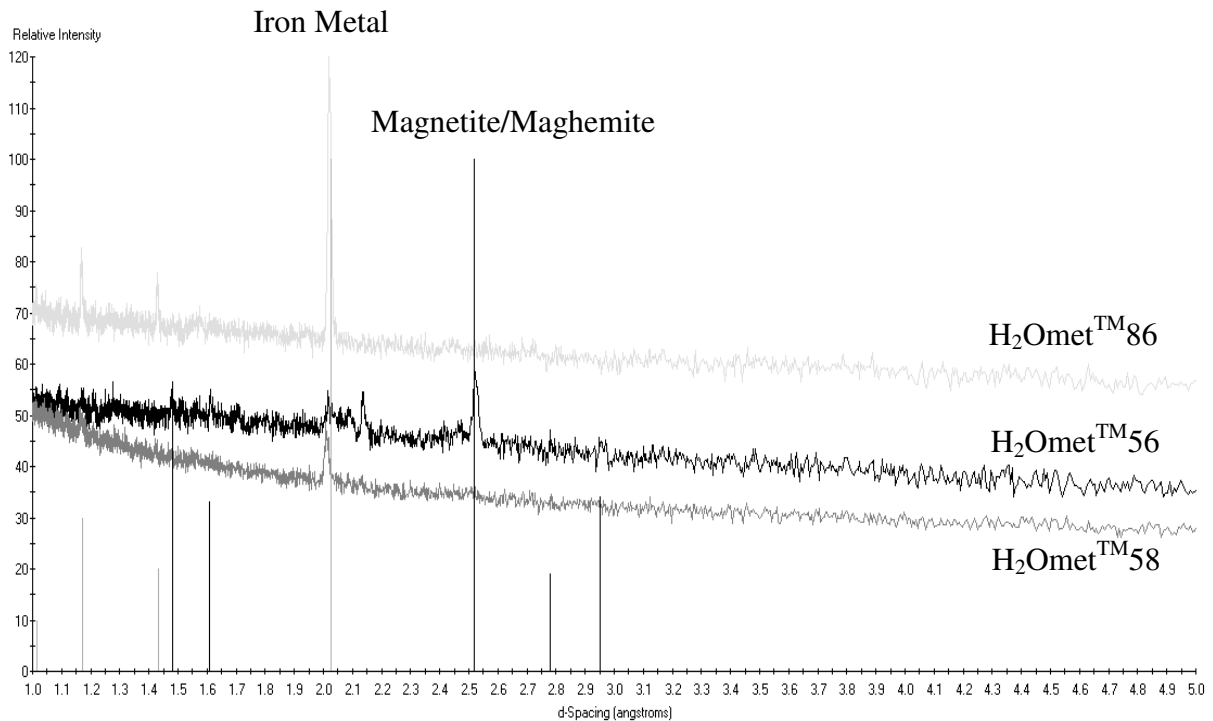


Figure 2.11: XRD analysis on "as received" H₂Omet[™]56, H₂Omet[™]58 and H₂Omet[™]86 irons demonstrates that H₂Omet[™]56 contains magnetite/maghemite while H₂Omet[™]58 and H₂Omet[™]86 are composed predominately of iron metal.

The presence of an oxide film may increase the hydrogen absorption proportion of an iron. Hydrogen gas is produced at the iron/oxide interface and must diffuse away from the iron surface to enter the aqueous phase (and gas phase if present). The presence of an oxide film would slow the diffusion of hydrogen away from the iron surface and should enhance the residence times and thus the proportion of hydrogen entering the iron lattice.

The hydrogen absorption proportions of the other two irons in Figure 2.10, Connelly and Alfa Aesar, lend further support to the proposed effect of oxide films on hydrogen absorption proportions. Connelly iron, the iron with the highest hydrogen absorption proportion, is a heavily oxidized iron (Figure A4) with an oxide film consisting of hematite and magnetite (Ritter et al., 2002). The higher absorption proportion of Connelly iron compared to H₂Omet[™]56 iron may be due to the degree of oxidation as the Connelly film is continuous and extensive while the H₂Omet[™]56 film is discontinuous as revealed by SEM images (see Figure 3.8). In contrast, Alfa Aesar iron, a 99.98% Fe unoxidized granular iron (Figure A5), demonstrates the lowest hydrogen absorption proportion of the irons. In general, the oxidized irons (Connelly and H₂Omet[™]56)

demonstrate higher hydrogen absorption proportions than the unoxidized irons (H₂OmetTM86, H₂OmetTM58 and Alfa Aesar).

2.3.6 Ultrasonic Treatment

Absorption of hydrogen into metals provides a reservoir of stored electrons within the iron that may be used in remediation reactions. However, use of these stored electrons requires release of hydrogen atoms from trapping sites within the iron lattice. Zhao and Reardon (2012) investigated the use of trapped hydrogen for the remediation of contaminants by comparing TCE degradation rates of irons that were charged at high hydrogen pressures to those of irons that were maintained at low pressures of hydrogen. The results of a series of batch experiments on QMP and Connelly iron indicated no significant difference in contaminant degradation rates between low and high hydrogen pressure treated irons. The authors attributed this to the high binding energies of hydrogen stored in the iron and suggested that certain physical, chemical or microbiological methods may be required to release trapped hydrogen for use in remediation reactions. In this section, the potential of ultrasonic treatment for release of stored hydrogen from lattice imperfections such as microcracks and crystal boundaries was investigated.

Sonochemistry (the chemistry of ultrasound) is based on the transfer of energy from an acoustic transducer to water molecules which alternately compress and stretch. This creates pressure differentials in the liquid and results in the formation of cavitation microbubbles. (Peters, 1996, Mason and Lorimer, 1988). Large pressure differentials between the bubbles and the surrounding liquid cause the bubbles to collapse, generating high temperatures and pressures (Suslick and Price, 1999, Gong and Hart, 1998). The localized temperatures and pressures associated with cavitation bubble collapse can be a unique method of driving chemical reactions (Suslick and Price, 1999).

Ultrasonic treatment may be capable of removing trapped hydrogen from iron lattice imperfections. One process by which cavitation may facilitate the release of trapped hydrogen from iron is by generating temperatures higher than those required for hydrogen release from imperfections such as grain boundaries (111⁰C), dislocations (214⁰C) and microvoids (305⁰C) (Choo and Lee, 1982). Alternatively, cavitation near the iron-solution interface can produce high-velocity water jets that penetrate the iron surface (Suslick and Price, 1999). These water jets can impart physical disturbances on the iron and may facilitate hydrogen release.

Ultrasound has been previously used in groundwater treatment for different applications. Previous researchers have demonstrated that ultrasonic treatment can improve the remediation of organic contaminants such as TCE, chloroform and carbon tetrachloride by enhancing contaminant desorption, decomposition and volatilization (Thangavadivel et al., 2010, Wu et al., 1995). Geiger et al. (2003) were among the first to implement ultrasound technology on a field-scale by lowering submergible resonators into wells with the objective of removing mineral precipitates and corrosion products from the PRB. At this time, however, ultrasonic treatment has not been applied to PRBs for the purpose of hydrogen release.

Use of ultrasonic treatment for the removal of trapped hydrogen was investigated by comparing hydrogen evolution rates during ultrasonic treatment to corresponding hydrogen evolution rates under control conditions. H₂OmetTM56 iron was chosen for the ultrasound experiments due to its ability to absorb large proportions of corrosion-produced hydrogen. Figure 2.12 contains a pair of control and ultrasound treated hydrogen evolution rate curves. A k value of $0.18 \text{ mmol kg}^{-1} \text{ d}^{-1} \text{ kPa}^{-0.5}$ was used to remove discontinuities from the control apparent rate curve and a k value of $0.30 \text{ mmol kg}^{-1} \text{ d}^{-1} \text{ kPa}^{-0.5}$ was used to remove discontinuities from the ultrasound treated apparent rate curve.

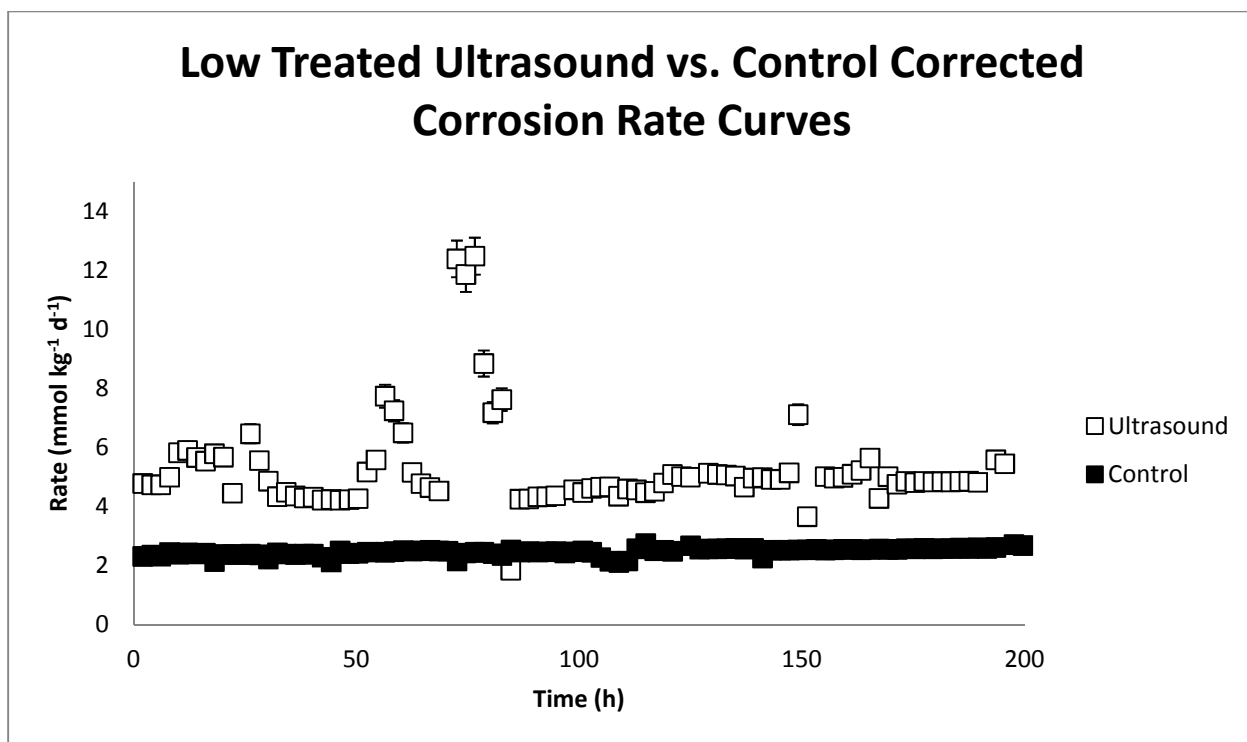


Figure 2.12: Comparison of corrosion rate curves for low-treated H₂OmetTM56 iron under control conditions (black) and submerged in an ultrasonic water bath (white). The variability in the ultrasound corrosion rate curve is due to temperature fluctuations of the water bath as a result of the cavitation process. The ultrasound corrosion rate curve is significantly (95% confidence) higher than the control corrosion rate curve.

Figure 2.12 demonstrates that the ultrasound treated hydrogen evolution rate curve is significantly higher (95% confidence) than the control hydrogen evolution rate curve. The higher hydrogen evolution rate of the ultrasound treated run may be due to hydrogen release from the iron, however other factors may also have produced the observed increase. Repositioning of particles within the reaction cells due to physical disturbances caused by the ultrasonic treatment would expose areas of fresh iron thus increasing the corrosion rate. Ultrasonic treatment may also remove oxide species from the granules, which would expose areas of bare iron metal and increase the corrosion rate of the iron. Although the temperature bath was run on intervals and refilled between intervals in an attempt to maintain a temperature of 25⁰C, heat generated by cavitation resulted in fluctuations in the water temperature of the bath and caused major variability in the ultrasound treated rate curve. These temperature fluctuations create a challenge in interpreting the ultrasound treated corrosion rate data.

To determine whether the higher hydrogen evolution rate of the ultrasound treated run was due to hydrogen release or to other factors, the irons were treated at low and high hydrogen pressures for 14 d before the cells were evacuated and hydrogen evolution rate curves were collected. Assuming that the higher hydrogen evolution rate of the ultrasound treated sample observed in Figure 2.12 was due to hydrogen release from lattice imperfections, the high treated iron should contain more absorbed hydrogen and therefore release more hydrogen resulting in a greater increase in the ultrasound treated apparent hydrogen evolution rate above the control rate compared to the low treated iron.

The ultrasound and control hydrogen evolution rate curves from Figure 2.12 were collected following a low hydrogen pressure treatment period. These hydrogen evolution rate curves were compared to similar rate curves that were collected following a high hydrogen pressure treatment period (Figure 2.13). In Figure 2.13, a k value of $0.11 \text{ mmol kg}^{-1} \text{ d}^{-1} \text{ kPa}^{-0.5}$ was used to remove discontinuities from the control apparent rate curve and a k value of $0.21 \text{ mmol kg}^{-1} \text{ d}^{-1} \text{ kPa}^{-0.5}$ was used to remove discontinuities from the ultrasound treated apparent rate curve.

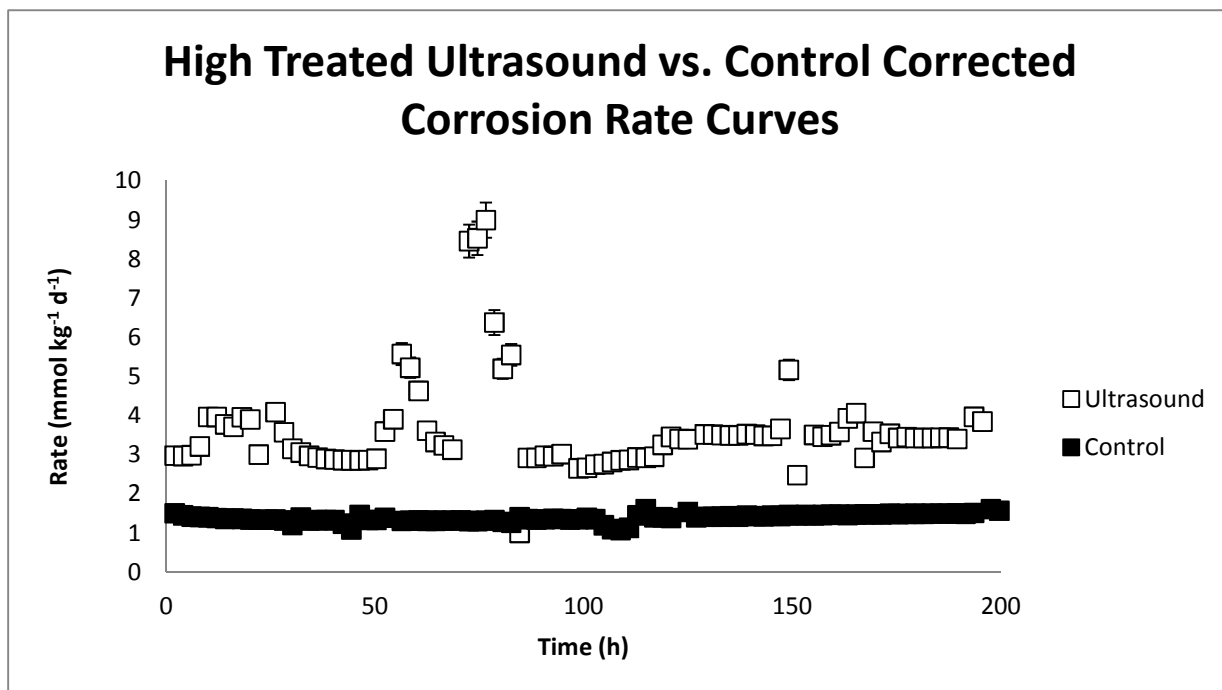


Figure 2.13: Comparison of corrosion rate curves for high-treated H₂OmetTM56 iron under control conditions (black) and submerged in an ultrasonic water bath (white). The ultrasound corrosion rate curve is significantly (95% confidence) higher than the control corrosion rate curve.

To evaluate the ability for ultrasonic treatment to release lattice stored hydrogen, the increase in hydrogen evolution rate of the ultrasound treated, high pressure treated iron above the hydrogen evolution rate of the control, high pressure treated iron was compared to the increase in the hydrogen evolution rate of the ultrasound treated, low pressure treated iron above the hydrogen evolution rate of the control, low pressure treated iron. The results are shown in Figure 2.14.

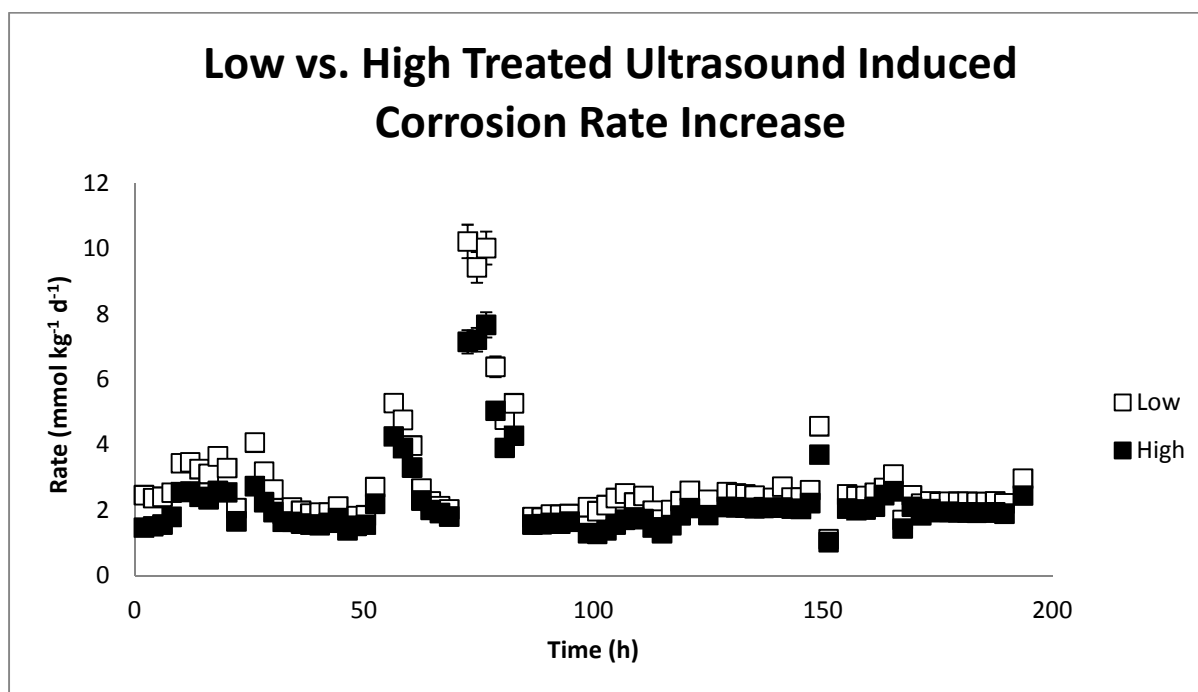


Figure 2.14: Comparison of the difference between the ultrasound and control corrosion rate curves for low and high hydrogen pressure treated H₂OmetTM56. No significant difference (95% confidence) between the low and high treated samples was observed indicating that ultrasonic treatment did not facilitate hydrogen release.

The ultrasound induced increase in the hydrogen evolution rate of the high treated sample was not larger than the ultrasound induced increase in the hydrogen evolution rate of the low treated sample. This similarity indicates that the increase in hydrogen evolution rate due to ultrasonic treatment observed in Figure 2.12 and 2.13 was not due to hydrogen release from the iron. Therefore ultrasonic treatment does not appear to be capable of facilitating hydrogen release. Other factors, such as repositioning of the iron granules or removal of the oxide film could explain the increased corrosion rate under ultrasound conditions. It was observed that the iron granules were repositioned in the reaction cells following ultrasonic treatment. This may have created cavities between iron granules and resulted in increased exposed surface area and

therefore increased hydrogen evolution rates of the ultrasound treated samples. Temperature fluctuations during the reactions make it difficult to properly interpret the corrosion rate data.

Although ultrasonic treatment did not appear to facilitate hydrogen release from the H₂Omet™ iron under the conditions of this study, similar studies on different irons and at different ultrasound frequencies could prove useful. Further studies aimed at reducing the temperature variability during the corrosion run could also be beneficial. One possible method for reducing the effect of temperature on the hydrogen evolution rate data is to run the ultrasound bath or an ultrasonic probe on shorter intervals to prevent the temperature from increasing substantially during the ultrasonic interval and allowing the water to return to 25°C between intervals.

2.4 Conclusion

Absorption of hydrogen gas generated by the anaerobic corrosion of iron has favourable effects on the performance of PRBs by mitigating reduction to porosity and permeability and preventing hydrogen from escaping the PRB. Hydrogen absorption also creates a stored electron resource within the iron for use in remediation reactions. However, utilization of stored hydrogen for groundwater remediation is an emerging field and many details must be elucidated before the viability of the technology can be appropriately assessed. In this study, factors governing hydrogen absorption by three H₂Omet™ irons and two other iron samples were investigated using hydrogen evolution rate curves. Ultrasound as a potential method for enhancing hydrogen release was also discussed.

Rates of hydrogen absorption were observed to be related to the overall corrosion rate of the iron as indicated by a linear increase in k with increasing corrosion rate. The observed relationship between k and corrosion rate was attributed to hydrogen pressure accumulation at iron surfaces due to the rate of hydrogen production exceeding the rate of hydrogen diffusion away from the iron surface.

The proportion of corrosion-produced hydrogen that was absorbed by the iron appeared to be influenced by the presence of an oxide film on the iron granules. Irons with oxide films were observed to absorb higher proportions of hydrogen than irons with bare iron surfaces. Higher proportions of hydrogen absorption in the presence of oxide films may be a result of longer residence times of hydrogen at iron surfaces due to a slowed diffusion process.

Ultrasonic treatment was evaluated as a potential method of release of lattice stored hydrogen. Preliminary results demonstrated that ultrasonic treatment was not effective at removing hydrogen from H₂OmetTM56 iron under the conditions of the study, however temperature variations introduced challenges in the interpretation of the corrosion rate curves. Further work aimed at reducing temperature variability during ultrasound treatment and investigating different irons and different ultrasonic frequencies could prove useful. In addition to ultrasonic treatment, further research should include evaluation of chemical and microbiological methods of hydrogen release.

3 EFFECT OF HYDROGEN ON IRON CORROSION RATES

3.1 Background

The extensive body of literature on hydrogen-metal interactions demonstrates that hydrogen can physically and chemically affect metal properties (Johnson, 1988, Hirth, 1980). As a result of these effects, changes to the corrosion rate of the metal may occur. Since iron corrosion rates influence PRB performance, hydrogen induced changes to corrosion rates should be considered in evaluations of PRB performance. In this chapter, the effect of hydrogen gas on the corrosion rates of H₂OmetTM56 and Connelly irons were evaluated. H₂OmetTM56 and Connelly iron were considered because both irons have applications in PRBs.

Influence of hydrogen on iron corrosion rates may occur by a variety of mechanisms. Absorption of hydrogen by iron, known as hydrogen embrittlement (HE), results in accumulation of hydrogen within iron and may facilitate a process known as hydrogen induced cracking (HIC) (Timmins, 1997). HIC increases the exposed surface area of the iron and therefore would be expected to increase corrosion rate. Even in cases where absorbed hydrogen concentrations are not sufficient to cause HIC, hydrogen enhanced anodic dissolution may occur (Mao and Li, 1998). Hydrogen enhanced anodic dissolution refers to the accelerated dissolution of iron in the presence of hydrogen (Qiao and Luo, 1998). Hydrogen may also influence iron oxide film properties. The stability and thickness of oxide films has been observed to decrease in the presence of hydrogen (Yu et al., 2003, Yu et al., 2002). Hydrogen can render oxide films more susceptible to pitting corrosion (Ningshen et al., 2006) and can facilitate the reduction of iron oxides within passive films, significantly altering oxide film composition (Pineau et al., 2007) and therefore iron corrosion rate.

All of these effects of hydrogen on iron have important implications on PRB performance. In this chapter, the effects of sustained hydrogen contact on the corrosion rates of two irons with applications in PRBs were investigated. H₂OmetTM56 iron and Connelly iron were treated at low and high hydrogen pressures for 14 d after which corrosion rate curves were collected. Possible mechanisms for the observed effect of hydrogen treatment on iron corrosion rates as well as implications of the findings to PRB design considerations were evaluated.

3.2 Methods

3.2.1 Materials

Two irons with applications in PRBs were used to evaluate the effect of hydrogen treatment on iron corrosion rate: H₂OmetTM56 iron and Connelly iron. H₂OmetTM56 iron contains a magnetite/maghemite surface coating (see Figure 2.11) and has a BET surface area of 0.17 m²/g. The physical appearance, particle size distribution and chemical composition of H₂OmetTM56 iron are included in Figure A1, Table A1 and Table A2 respectively. Connelly iron contains a highly oxidized ferric oxide surface coating as evidenced by its reddish-brown physical appearance (Figure A4). The Connelly iron tested is composed of 89.8% Fe and 2.85% C with a surface area of 1.22 m²/g (Zhao, 2010).

To evaluate potential mechanisms for the observed effect of hydrogen on iron corrosion rate, additional hydrogen treatment experiments were conducted using 99.98% pure Alfa Aesar iron granules. The surface area of Alfa Aesar iron is 5.08x10⁻⁴ m²/g based on the assumption of a cubic shape and average grain size of 1.5 mm for each granule. The physical appearance of Alfa Aesar iron is shown in Figure A5.

3.2.2 Hydrogen Treatment Experiments

The hydrogen treatment corrosion experiments were conducted according to the procedure described in Chapter 2 with a few exceptions. After preparing the cells as described in Chapter 2 and evacuating both cells, the high treatment cell was pressurized with analytical grade hydrogen to approximately 400 kPa while the low treatment cell was left under evacuated conditions. To maintain low hydrogen pressure conditions in the low treatment cell, the cell was frequently evacuated using a Two Stage High Vacuum Pump (Edwards Ltd.). To maintain high hydrogen pressure conditions in the high treatment cell, hydrogen was added to the cell if sufficient hydrogen was absorbed by the iron to reduce the pressure below approximately 200 kPa.

To allow for measurements of pressures above the burst pressure of the 0-15AV pressure transducer (approximately 300 kPa), the high treatment cell was outfitted with an Omega PX302-050AV pressure transducer (burst pressure of approximately 600 kPa). An Omega PX319-015AV pressure transducer was used for the low treatment cell. The cells were maintained at low

and high hydrogen pressures for 14 d before both cells were evacuated. This evacuation marked the beginning of the post-treatment corrosion experiments.

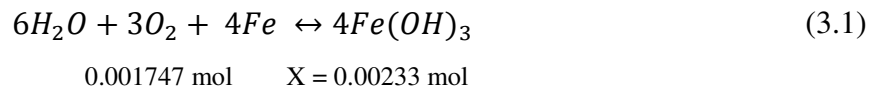
To prevent oxidation of the irons following the corrosion experiment, used iron was stored in Mason jars flushed with analytical grade prepurified nitrogen. The samples were then dried using a Two Stage High Vacuum Pump (Edwards Ltd.) prior to scanning electron microscope (SEM) analysis.

3.2.3 Iron Oxidation Experiments

To determine whether reduction of iron oxides by hydrogen gas occurred under the temperature and pressure conditions of the corrosion experiments, a series of iron oxidation experiments were conducted using Alfa Aesar iron. Initially, a baseline corrosion rate curve was collected for Alfa Aesar iron and used to determine the total hydrogen produced during 200 h of corrosion. This value was denoted as X moles of hydrogen gas.

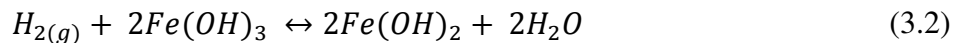
A second Alfa Aesar corrosion experiment was then conducted in which enough oxygen was added to produce X moles of Fe(OH)₃. The amount of oxygen required was calculated as follows:

$$X = 0.00233 \text{ mol H}_2$$



$$V = \frac{nRT}{p} = \frac{(0.001747 \text{ mol})(8.3144621 \text{ L kPa mol}^{-1} \text{ K}^{-1})(298.15 \text{ K})}{(101.1 \text{ kPa})} = 0.043 \text{ L}$$

Therefore, X moles of Fe(OH)₃ were produced by the addition of 43 mL of O_{2(g)} to the reaction cell at the beginning of the corrosion reaction. Based on the reaction for gaseous reduction of iron oxides by hydrogen gas (Equation 3.2), X moles of Fe(OH)₃ would consume half of the hydrogen gas produced during the reaction. This would result in a corrosion rate for the oxidation reaction of half the baseline corrosion rate.



Similarly, in a second oxidation experiment, 86 mL of oxygen was added to the reaction cell to produce $2X$ moles of $\text{Fe}(\text{OH})_3$. According to Equation 3.2, $2X$ moles of $\text{Fe}(\text{OH})_3$ would consume all of the hydrogen produced by the corrosion reaction.

3.3 Results and Discussion

$\text{H}_2\text{Omet}^{\text{TM}}56$ and Connelly irons were treated under low and high hydrogen pressures for 14 d after which corrosion rate curves were established to investigate the effect of hydrogen treatment on iron corrosion rates.

3.3.1 $\text{H}_2\text{Omet}^{\text{TM}}56$ Iron

The corrected corrosion rate curves for the post-treatment period for low and high treated $\text{H}_2\text{Omet}^{\text{TM}}56$ iron are presented in Figure 3.1 and Figure 3.2. A k value of $0.18 \text{ mmol kg}^{-1} \text{ d}^{-1} \text{ kPa}^{-0.5}$ removed discontinuities from the low treated $\text{H}_2\text{Omet}^{\text{TM}}56$ apparent rate curve while a k value of $0.11 \text{ mmol kg}^{-1} \text{ d}^{-1} \text{ kPa}^{-0.5}$ removed discontinuities from the high treated $\text{H}_2\text{Omet}^{\text{TM}}56$ apparent rate curve.

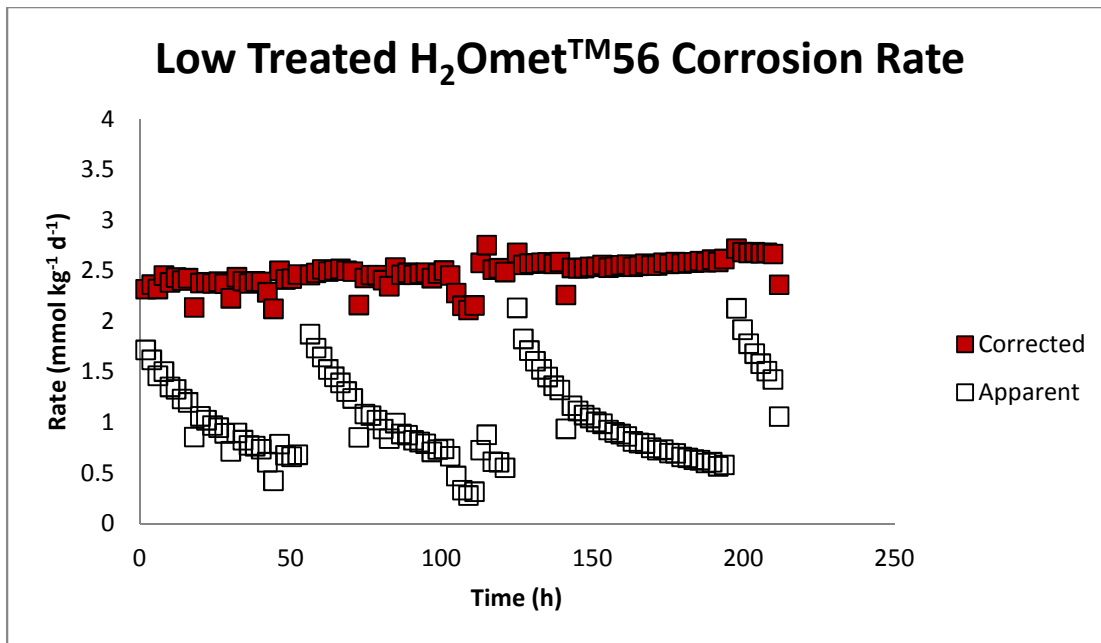


Figure 3.1: Post-treatment corrected and apparent corrosion rate curves for H₂Omet™56 iron treated under low pressures of hydrogen for 14 d.

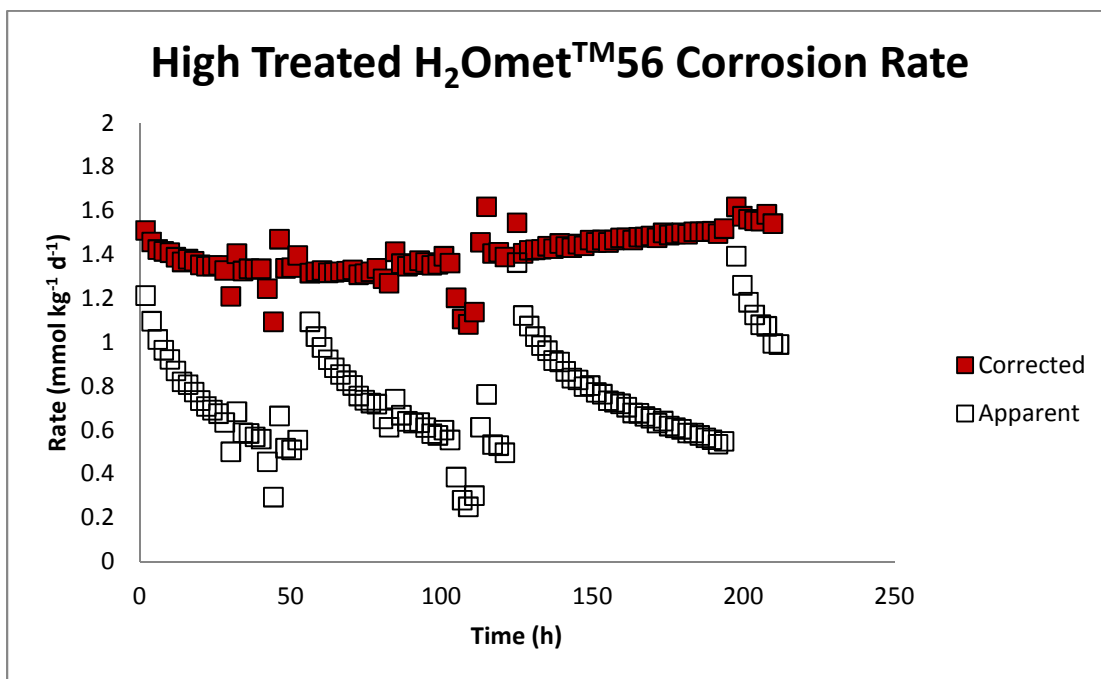


Figure 3.2: Post-treatment corrected and apparent corrosion rate curves for H₂Omet™56 iron treated under high pressures of hydrogen for 14 d.

The corrosion rate of the low treated H₂OmetTM56 iron was significantly (95% confidence) higher than the corrosion rate of the high treated H₂OmetTM56 iron (Figure 3.3).

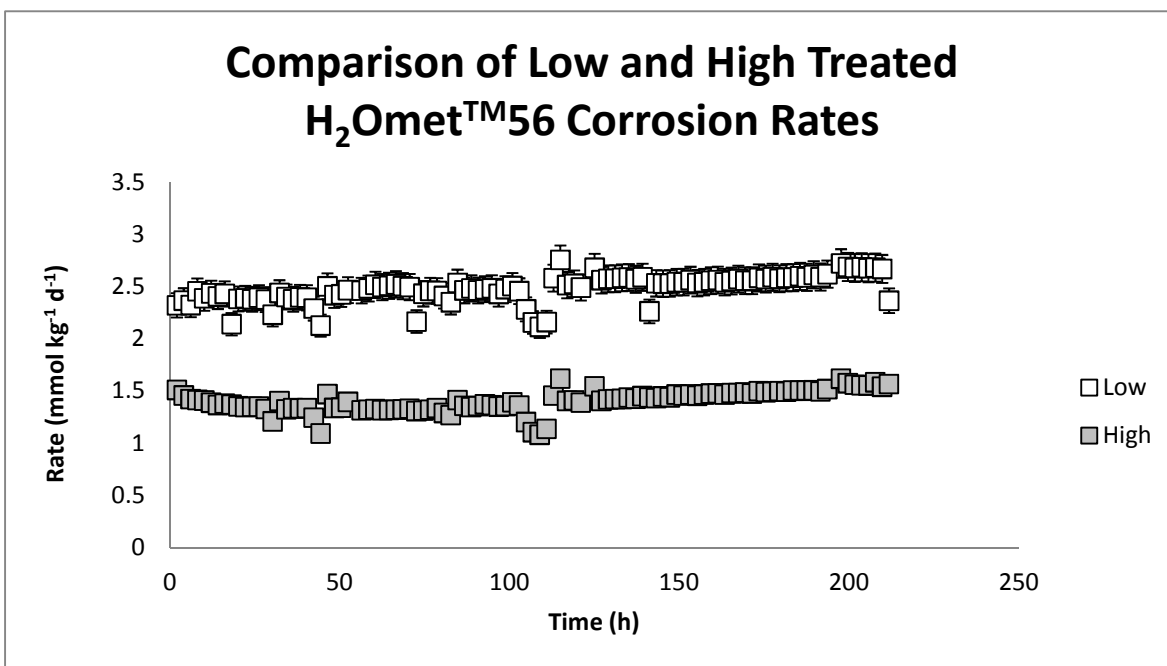


Figure 3.3: Comparison of post-treatment corrected rate curves for low and high treated H₂OmetTM56 iron. The post-treatment corrected corrosion rate of low treated H₂OmetTM iron was a factor of two higher than the post-treatment corrected corrosion rate of high treated H₂OmetTM iron.

3.3.2 Connelly Iron

The post-treatment corrected corrosion rate curves for low and high treated Connelly iron are presented in Figure 3.4 and Figure 3.5 respectively. A k value of $0.070 \text{ mmol kg}^{-1} \text{ d}^{-1} \text{ kPa}^{-0.5}$ removed discontinuities from the low treated Connelly apparent rate curve and a k value of $0.060 \text{ mmol kg}^{-1} \text{ d}^{-1} \text{ kPa}^{-0.5}$ removed discontinuities from the high treated Connelly apparent rate curve. The negative apparent rates indicate that the rate of hydrogen absorption was greater than the rate of hydrogen production during those periods.

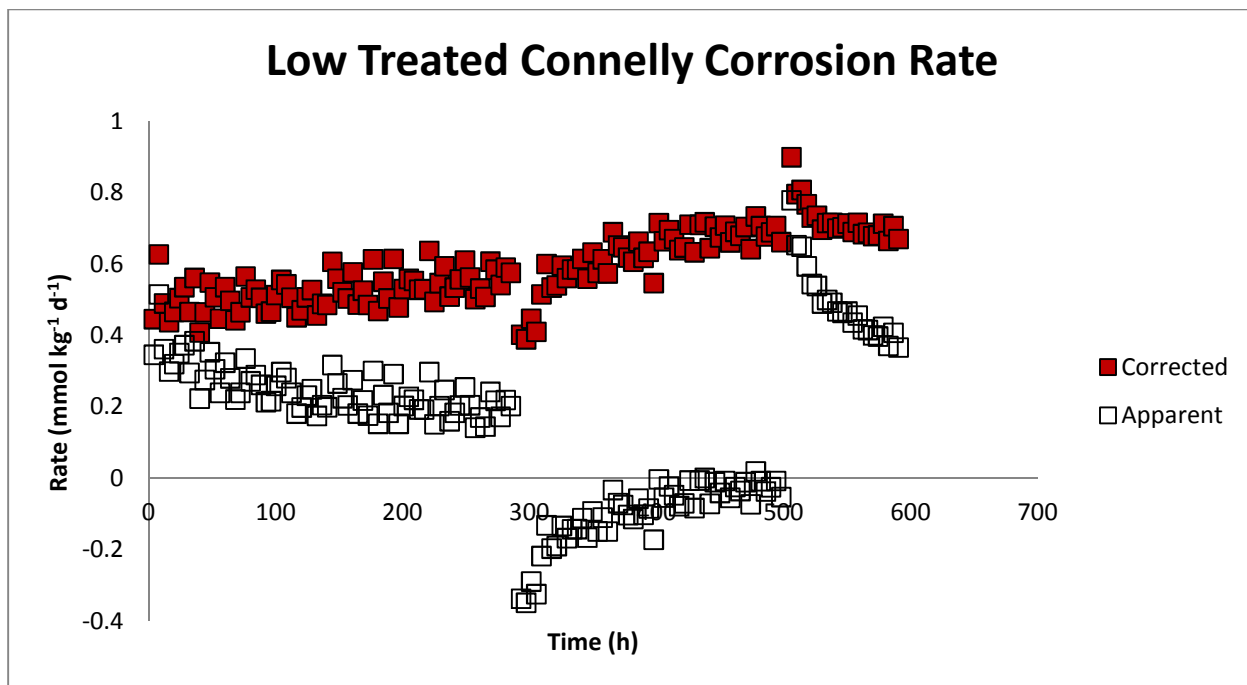


Figure 3.4: Post-treatment corrected and apparent corrosion rate curves for Connelly iron treated under low pressures of hydrogen for 14 d.

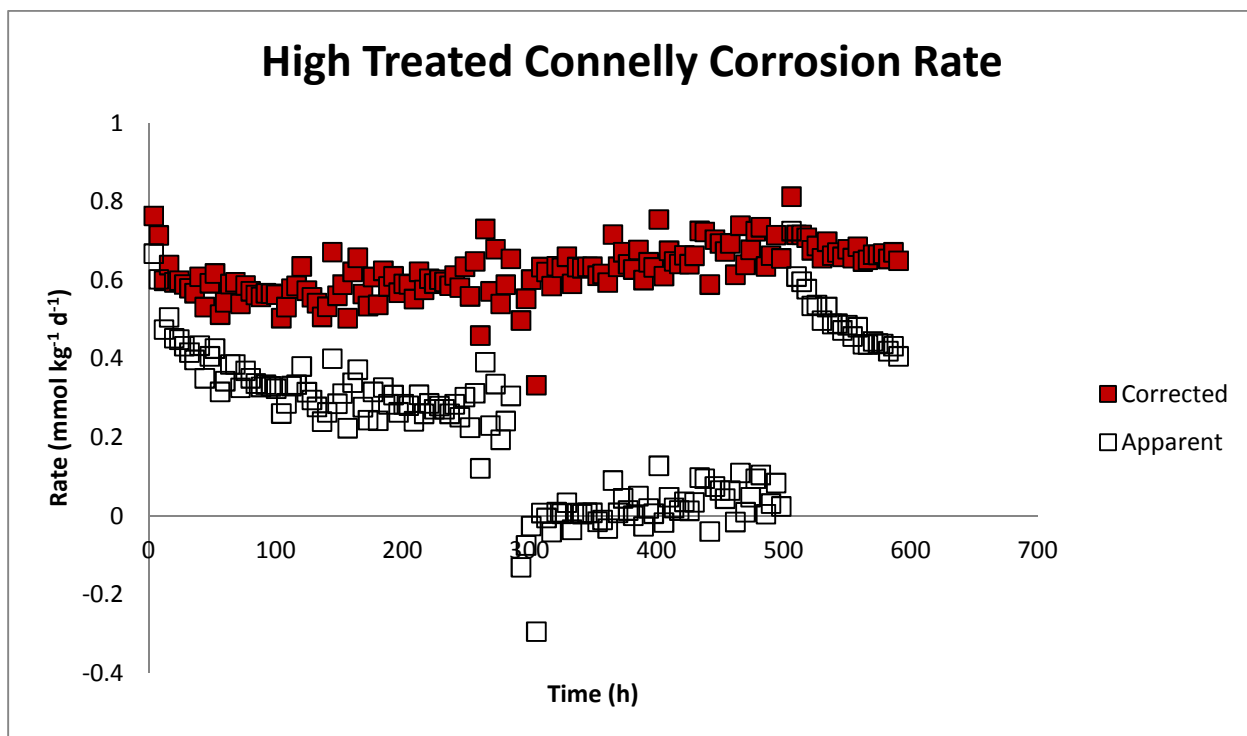


Figure 3.5: Post-treatment corrected and apparent corrosion rate curves for Connelly iron treated under high pressures of hydrogen for 14 d.

The corrosion rates of low and high treated Connelly iron did not differ significantly (95% confidence) except for at early time when the high treated Connelly corrosion rate exceeded than the low treated Connelly corrosion rate (Figure 3.6).

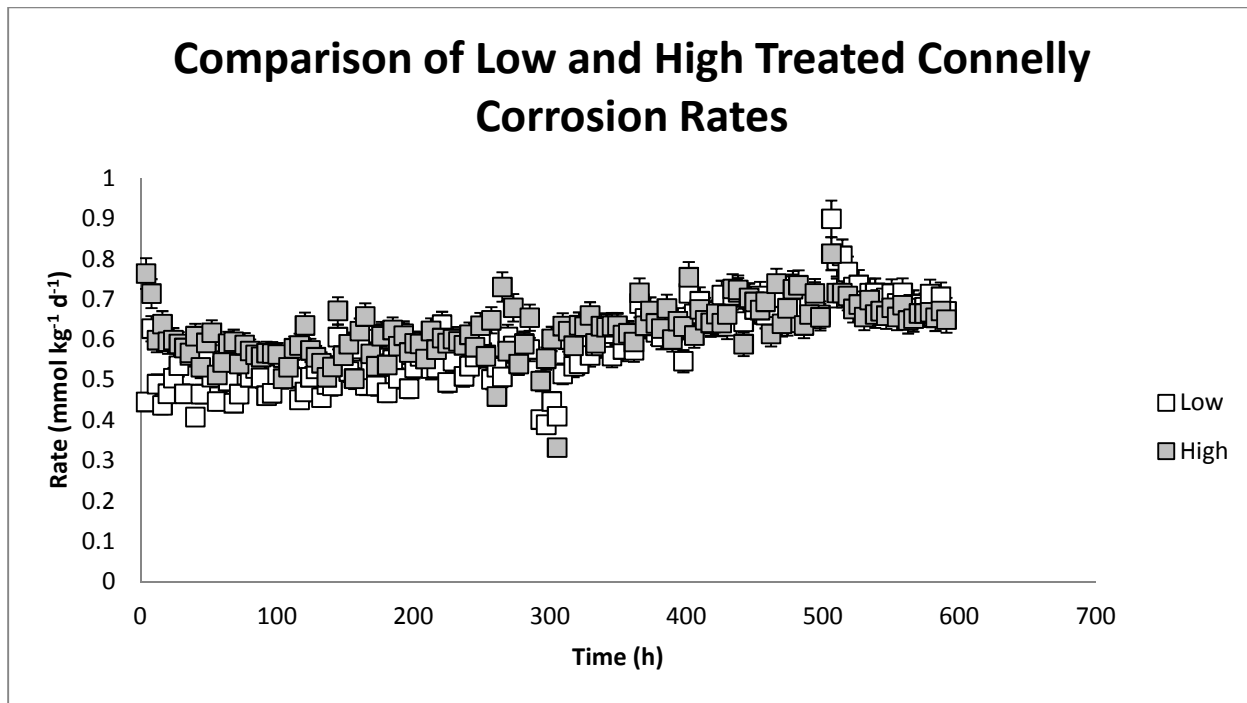


Figure 3.6: Comparison of post-treatment corrected rate curves for low and high treated Connelly iron. No significant difference in the post-treatment corrosion rates of the two samples was observed.

The observations from Figure 3.1 to 3.6 are summarized as follows:

1. The post-treatment corrosion rate of low treated H₂OmetTM56 iron was higher than the post-treatment corrosion rate of high treated H₂OmetTM56 iron.
2. There was no difference between the post-treatment corrosion rates of low and high treated Connelly iron.

A discussion of potential explanations for the effect of hydrogen treatment on H₂OmetTM56 and Connelly iron corrosion rates is included in the following sections.

3.3.3 Scanning Electron Microscope (SEM) Analysis

SEM analysis was conducted on low and high treated H₂OmetTM56 irons following the corrosion experiments to investigate possible causes for the reduced corrosion rate of high treated H₂OmetTM56 iron. The SEM images are included in Figure 3.7 and Figure 3.8.

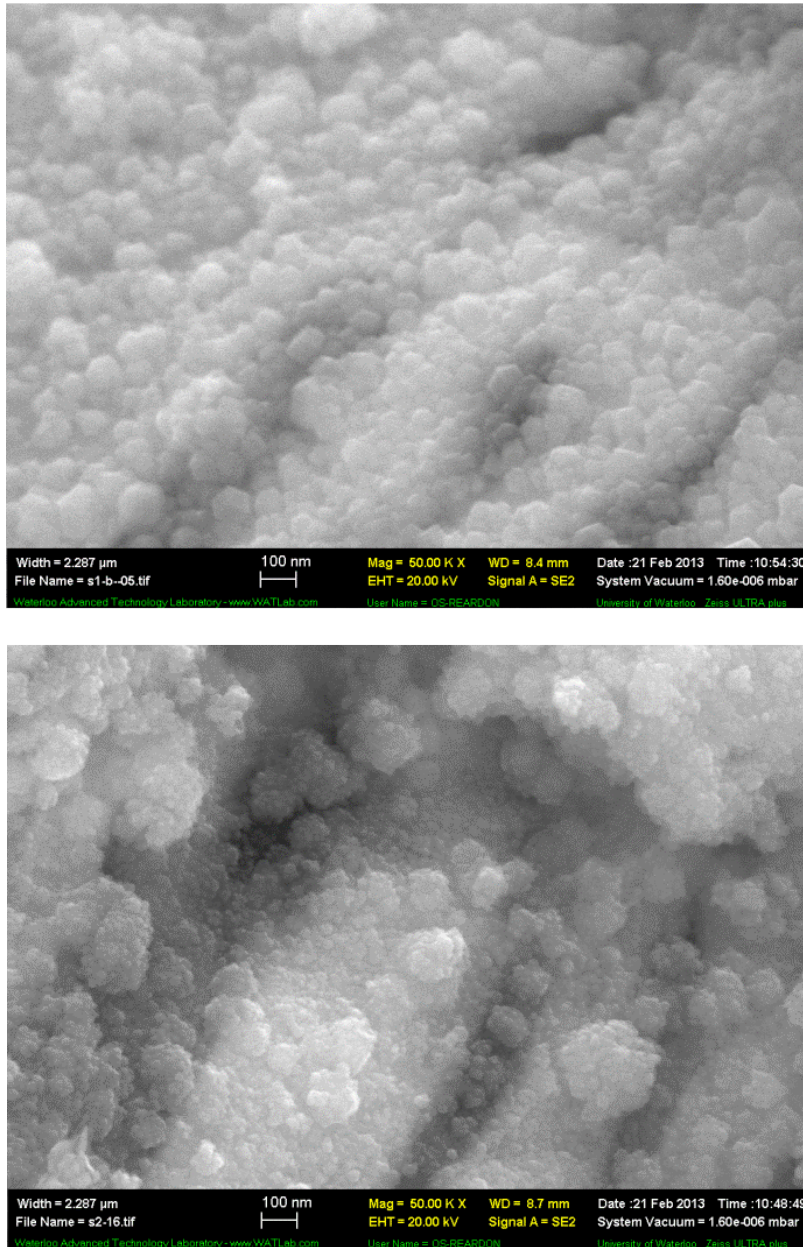


Figure 3.7: SEM photographs of low pressure treated H₂OmetTM56 iron (top) and high pressure treated H₂OmetTM56 iron (bottom). The images demonstrate more oxide crystals and the presence of tubercles on the high pressure treated iron indicating that the high treated iron has reached a more advanced stage of iron corrosion than the low pressure treated iron.

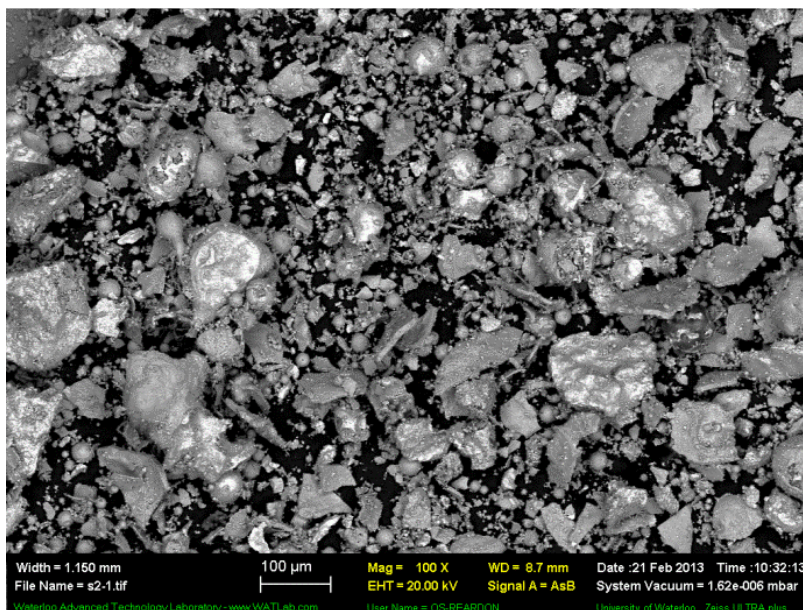
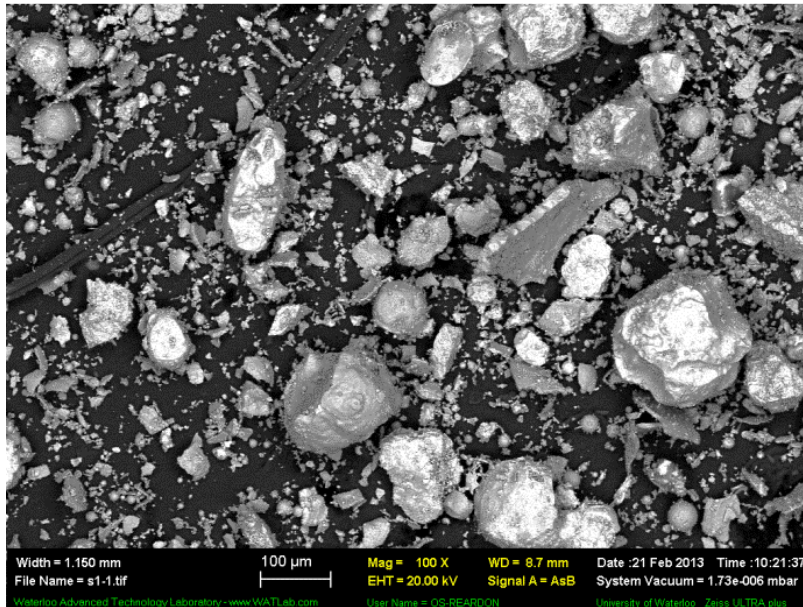


Figure 3.8: SEM photographs of low pressure treated H₂OmetTM56 iron (top) and high pressure treated H₂OmetTM56 iron (bottom). The images demonstrate a more uniform and extensive oxide film (gray) on the high hydrogen treated iron and more areas of exposed iron metal (white) on the low hydrogen treated iron.

Figure 3.7 indicates that the iron oxide surface coating of the high pressure treated H₂OmetTM56 iron contains oxide clusters known as tubercles while the low pressure treated iron does not. The presence of tubercles is indicative of a later stage of iron corrosion (Sarin, 2004a). Although corrosion begins relatively uniformly, as the reaction proceeds thicker areas of oxide film develop above anodic sites. Anodic sites are regions where the iron dissolution reaction occurs. Although the thick oxide film above anodic sites prevents oxidizers, in this case water, from reaching the iron surface, oxidizers can travel to thinner areas of the oxide film causing electron transfer through the iron from anodic sites to oxidant rich areas. This allows the iron dissolution reaction to proceed at anodic sites, releasing Fe²⁺ ions into the thick oxide film layer above the anodic sites. Here, the Fe²⁺ ions encounter anions such as OH⁻ and precipitate as (hydr)oxide species such as Fe(OH)₂. This results in further oxide deposition in the already thick oxide locations above anodic sites and the formation of tubercles such as those observed in Figure 3.7. Since tubercles form following continued corrosion, the presence of these structures on the high treated iron and their absence on the low treated iron suggest that the high treated iron achieved a more advanced stage of iron corrosion than the low treated iron in the same time period.

Figure 3.8 also suggests more advanced iron corrosion on the high hydrogen treated iron compared to the low treated iron. From Figure 3.8, the low treated H₂OmetTM56 iron contains more exposed metallic iron (white) and therefore a less extensive oxide film (gray) than the high treated H₂OmetTM56 iron. Since continued corrosion results in oxide film precipitation, the more extensive oxide film on the high treated iron indicates a more advanced stage of iron corrosion.

Oxide film precipitation occurs by a dissolution-precipitation process in which Fe⁰ dissolves as Fe²⁺ and subsequently precipitates as FeOH before conversion to Fe₃O₄ (Odziemkowski et al., 1998). Therefore, enhanced iron dissolution during high hydrogen treatment is a possible explanation for the increased oxide film precipitation on the high hydrogen treated iron compared to the low hydrogen treated iron. Through a process known as hydrogen enhanced anodic dissolution, hydrogen is capable of accelerating the dissolution of metals such as iron and steel (Yu et al., 2003, Qiao and Luo, 1998). In the following section, hydrogen enhanced anodic dissolution is discussed as a possible explanation for the observed effect of hydrogen on iron corrosion rates. The subsequent sections consider the possible influences of two other effects of hydrogen-iron interactions: reduction of iron oxides and hydrogen induced pitting corrosion.

3.3.4 *Hydrogen Enhanced Anodic Dissolution*

Hydrogen enhanced anodic dissolution describes the accelerated dissolution of metals in the presence of hydrogen. This effect of hydrogen on metal dissolution was proposed by Qiao and Luo (1998) and has since been observed by subsequent researchers (Huang et al., 2011, Dan et al., 2010, Yu et al., 2003, Mao and Li, 1998). Although not well understood, it is thought that hydrogen enhanced anodic dissolution occurs due to accumulation of hydrogen within the metal which causes changes to the internal energy and entropy associated with the dissolution reaction (Mao and Li, 1998).

To evaluate whether hydrogen enhanced anodic dissolution is a potential explanation for the observed difference in the post-treatment corrosion rates of low and high hydrogen treated H₂OmetTM56 iron, hydrogen treatment experiments were carried out on 99.98% pure Alfa Aesar iron (see *Methods*). Although many of the processes by which hydrogen affects iron corrosion require the presence of a surface film (hydrogen induced pitting corrosion, reduction of iron oxides), hydrogen enhanced anodic dissolution has been documented to occur on bare metals (Gu et al., 1999). The surface of Alfa Aesar iron is initially bare, so decrease in the post-treatment corrosion rate of high pressure treated Alfa Aesar iron would provide evidence for hydrogen enhanced anodic dissolution as a possible mechanism for the observed effect of hydrogen treatment on H₂OmetTM56 iron corrosion rates. No decrease in the post-treatment corrosion rate of high treated Alfa Aesar iron would suggest that a process causing changes to the oxide film is responsible for the observed effect.

Alfa Aesar iron was treated under low and high hydrogen pressures for 7 d. Figure 3.9 compares the post-treatment corrected corrosion rates of low and high treated Alfa Aesar iron.

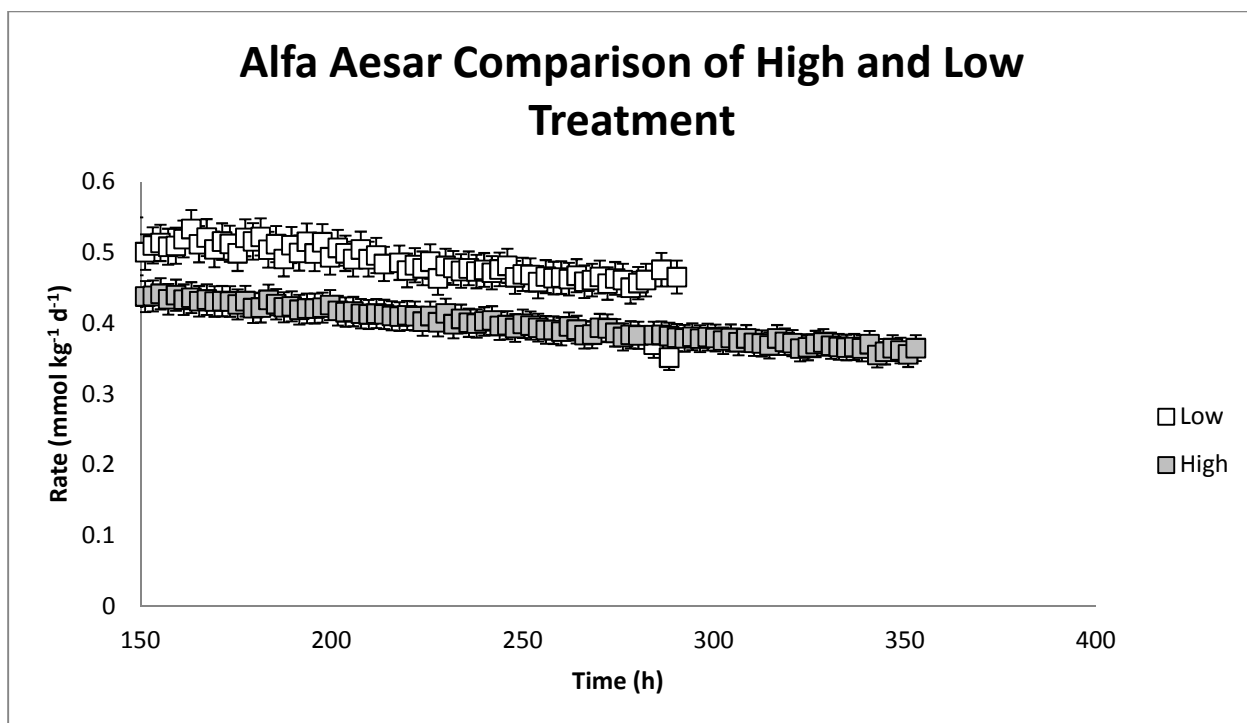


Figure 3.9: Comparison of post-treatment corrected corrosion rate curves for low and high treated Alfa Aesar iron following 7 d of treatment at low and high hydrogen pressures. High hydrogen treatment resulted in a decreased post-treatment corrosion rate of Alfa Aesar iron.

The post-treatment corrosion rate of high treated Alfa Aesar iron was significantly (95% confidence) lower than the post-treatment corrosion rate of low treated Alfa Aesar iron over 300 h (Figure 3.9). This is similar to what was observed for H₂OmetTM56 iron, although not as pronounced. The less pronounced effect of hydrogen on Alfa Aesar iron corrosion rates may be due to the lower surface area of Alfa Aesar iron and the lower treatment period for Alfa Aesar iron compared to H₂OmetTM56 iron. The similar response of the two irons to hydrogen treatment provides evidence for hydrogen enhanced anodic dissolution as a possible explanation for the decreased corrosion rate of the high treated irons. As Alfa Aesar iron is a bare iron with no initial oxide present, other mechanisms of hydrogen influence on corrosion rate (hydrogen induced pitting corrosion, reduction of iron oxides) are not viable explanations, however hydrogen enhanced anodic dissolution can occur on bare metal surfaces and remains a possible explanation for the observed effect.

The corrosion behaviour of the irons during the treatment period can also be used to evaluate hydrogen enhanced anodic dissolution as a possible explanation for the reduced corrosion rate of

high treated H₂Omet™56. Due to a leak in the high treated reaction vessel during the high treatment period, a corrosion rate curve for the hydrogen treatment period of high treated Alfa Aesar iron was not available. However, an intermediate Alfa Aesar treatment run in which hydrogen pressures were maintained between approximately 100 kPa and 150 kPa was also conducted. The post-treatment corrosion rate of the Alfa Aesar intermediate treated iron demonstrated a similar response to hydrogen treatment as was observed in the post-treatment corrosion rate of the high treated Alfa Aesar iron although the response was smaller in magnitude. Therefore, the treatment period for the intermediate treated iron is considered to be a muted representation of the treatment period for the high treated iron. Figure 3.10 compares the corrosion rates during the treatment period for low and intermediate hydrogen pressure treated Alfa Aesar iron.

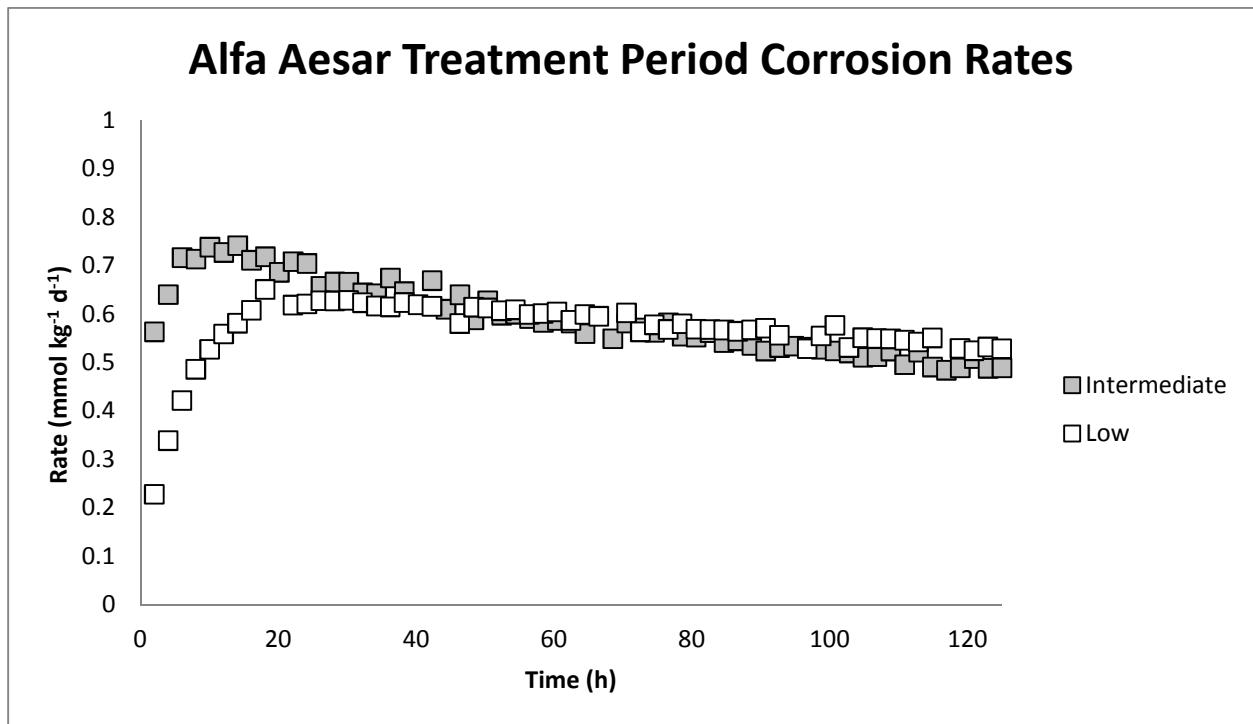


Figure 3.10: Comparison of treatment period corrosion rates for Alfa Aesar iron treated at low and intermediate hydrogen pressures. Intermediate hydrogen pressures resulted in a more rapid increase and subsequent decline to lower hydrogen evolution rate than low hydrogen pressures.

The hydrogen evolution rate curves included in Figure 3.10 indicate that the intermediate hydrogen treated iron peaked higher and then declined more rapidly than the iron treated at low hydrogen pressures. The higher peak in the hydrogen evolution rate of the intermediate treated

iron compared to the low treated iron indicates initially accelerated iron corrosion in the intermediate hydrogen treated sample. Hydrogen enhanced anodic dissolution is a possible explanation for the accelerated corrosion in the presence of hydrogen. Because iron corrosion results in the accumulation of corrosion products which passivate metal surfaces, hydrogen enhanced anodic dissolution may also explain the more rapid decline in the corrosion rate of intermediate treated iron. As the oxide film formed more rapidly on the intermediate treated iron than on the low treated iron, the corrosion rate declined more rapidly eventually resulting in a lower long-term corrosion rate of the intermediate treated iron compared to the low treated iron.

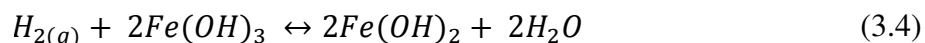
Connelly iron did not demonstrate the same decrease in corrosion rate after high hydrogen pressure treatment as H₂OmetTM56 iron. This could be due to the extensive ferric oxide film on Connelly iron which may have prevented hydrogen from penetrating to the bare iron surface and enhancing anodic dissolution. Ritter et al. (2002) performed normal Raman spectroscopic measurements (NRS) on dry Connelly iron and discovered hematite and magnetite in all observed locations and maghemite in some additional locations. These observations, and the reddish-brown physical appearance of Connelly iron, are evidence that an extensive ferric oxide film exists on "as received" Connelly iron. In contrast, SEM photographs of low treated H₂OmetTM56 iron revealed areas of exposed iron metal on the iron surface even after 500 h of corrosion (Figure 3.8). Therefore, hydrogen may have accumulated on the exposed iron surfaces of H₂OmetTM56 iron, facilitating hydrogen enhanced anodic dissolution, whereas hydrogen was prevented from penetrating to the iron metal on Connelly iron by the continuous ferric oxide film.

Based on these results, hydrogen enhanced anodic dissolution remains a possible explanation for the observed effects of hydrogen treatment on the corrosion rates of H₂OmetTM56 and Connelly iron. However, some other potential effects of hydrogen on iron corrosion may also be important. One such effect, the reduction of iron oxides by hydrogen, is discussed in the following section.

3.3.5 Reduction of Iron Oxides

The reduction of iron oxides by hydrogen may have also influenced H₂OmetTM56 and Connelly iron corrosion rates. Therefore, it is important to consider whether reduction of iron oxides by hydrogen occurs under the reaction conditions considered in this study.

One process by which hydrogen reduces iron oxides is by gaseous reduction. Gaseous reduction of iron oxides has been extensively studied in corrosion science literature (Pineau et al., 2006, Wagner et al., 2006, Sastri et al., 1982 and others). Most previous studies consider the reductive properties of hydrogen at temperatures that are not relevant to PRB applications (>200⁰C), however it has recently been questioned whether hydrogen gas can reduce iron oxides under the pressure and temperature conditions of PRBs (Reardon, 2013). An example reaction for the reduction of ferric hydroxide to ferrous hydroxide by gaseous hydrogen is as follows:



An experiment was conducted using 99.98% pure Alfa Aesar iron to determine whether gaseous reduction of iron oxides is possible under the temperature and pressure conditions of the corrosion experiments (see *Iron Oxidation Experiments*). Briefly, three corrosion experiments were conducted: one using "as received" Alfa Aesar iron, a second using Alfa Aesar iron with X moles of iron oxides produced by the addition of 43 mL of oxygen and a third using Alfa Aesar iron with 2X moles of iron oxides produced by the addition of 86 mL of oxygen. Reduction of iron oxides by hydrogen would result in the consumption half of the produced hydrogen gas in the reaction containing X moles of iron oxides and the apparent hydrogen evolution rate would be accordingly reduced. Reduction of iron oxides by hydrogen would result in the consumption of all of the produced hydrogen gas in the reaction containing 2X moles of iron oxides. Figure 3.11 shows the results of the iron oxidation experiments.

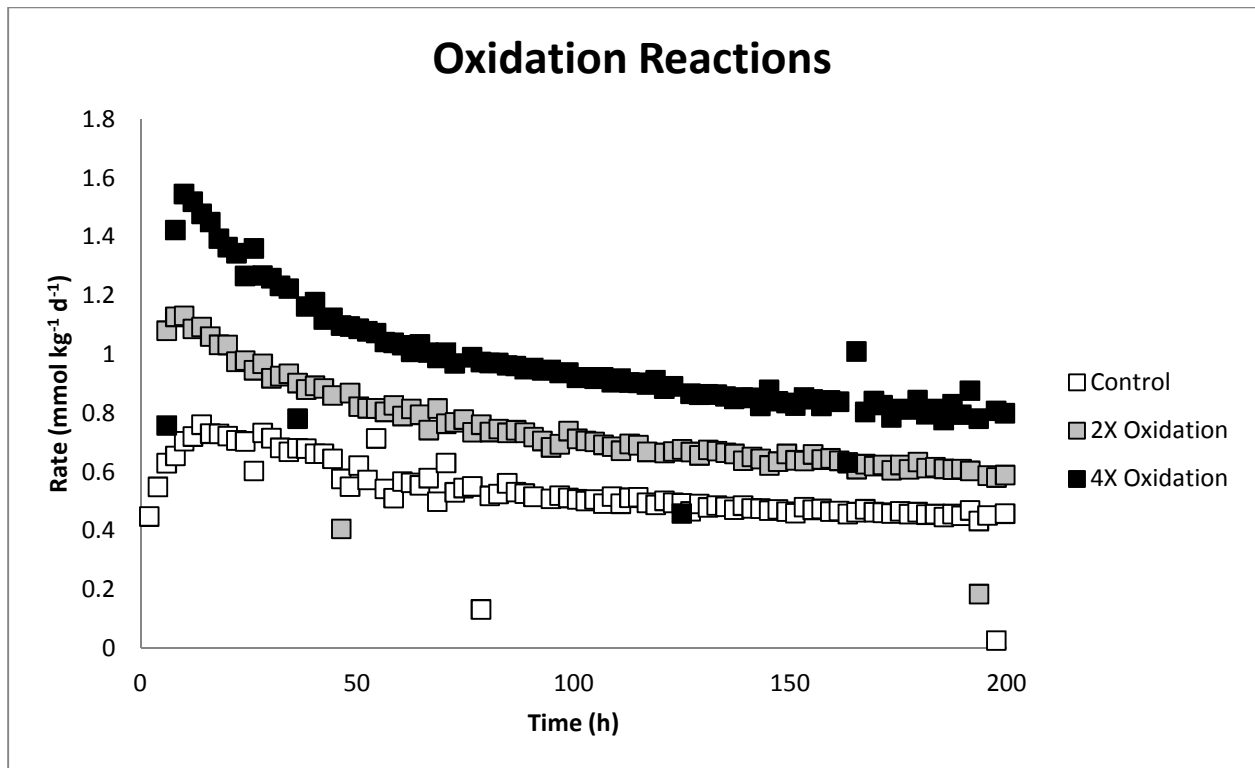


Figure 3.11: Comparison of Alfa Aesar iron corrected corrosion rate curves for the baseline run with no oxygen addition, X run with 43 mL of oxygen addition and 2X run with 86 mL of oxygen addition. The hydrogen evolution rate increased with increasing oxygen addition and the effect was sustained for at least 200 h of corrosion.

The presence of iron oxides in the X and 2X corrosion runs of Alfa Aesar iron did not cause a reduction the overall corrosion rates of the irons as would be expected under conditions of gaseous iron oxide reduction (Figure 3.11). Instead an increase in the corrosion rate was observed for both oxidized samples. This suggests an accelerating effect of oxygen on iron corrosion rates.

Previous researchers have demonstrated an increase in the corrosion rate of iron in the presence of dissolved oxygen (Sarin et al., 2004b, Foroulis et al., 1979) and have attributed this effect to the cathodic reduction of oxygen on iron surfaces. However, for cathodic reduction of oxygen to occur, oxygen must remain present in the system. During the iron oxidation experiments it was observed that all added oxygen was consumed within 1 h of addition to the reaction cell. Therefore, if cathodic reduction of oxygen was the mechanism responsible for increasing the iron corrosion rate, increased corrosion rates due to the presence of oxygen should have only been observed within the first hour of the corrosion experiment while oxygen remained present.

However the effect of oxygen on corrosion rate was sustained over 200 h (Figure 3.11). In fact, the oxygen induced increase in corrosion rate continued for at least 500 h (Figure 3.12).

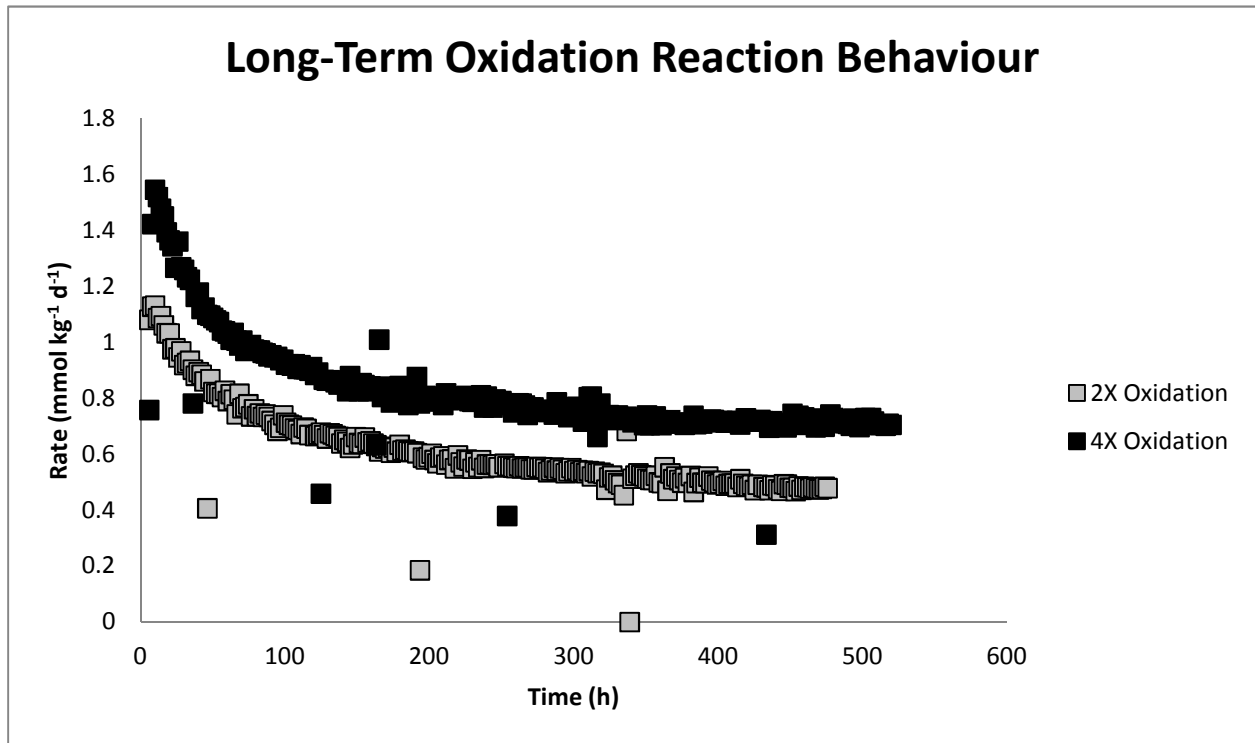


Figure 3.12: Comparison of Alfa Aesar iron corrected corrosion rate curves for the X run with 43 mL of oxygen addition and the 2X run with 86 mL of oxygen addition. The hydrogen evolution rate increased with increasing oxygen addition and the effect was sustained for at least 500 h of corrosion.

The sustained increase in corrosion rate of the X and 2X corrosion runs, even after complete consumption of the added oxygen, may be due to increased cracking of the iron as a result of oxygen addition. Previous researchers (Isselin et al., 2011, Otsuka et al., 2011, Was and Bruemmer, 1994) have identified an increase in crack initiation and propagation of metals as a result of dissolved oxygen. Increased crack initiation and propagation of iron would increase the surface area of exposed iron metal. This would increase the corrosion rate of the metal and the effect would be sustained in the absence of oxygen as was observed for Alfa Aesar iron.

It is reasonable to assume that the 2X Alfa Aesar run contained twice as many oxygen induced cracks than the X Alfa Aesar run because crack initiation and propagation have been observed to be proportional to dissolved oxygen concentration (Otsuka et al., 2011). Therefore, assuming no gaseous iron oxide reduction, the increase in hydrogen production of the 2X corrosion run above

baseline hydrogen production should be twice the increase in hydrogen production of the X run above baseline hydrogen production. However, the 2X run contained more iron oxides, and consequently a higher potential for hydrogen consumption due to iron oxide reduction, than the X run. Therefore, if gaseous reduction of iron oxides occurred during the corrosion reactions, the apparent hydrogen production of the 2X run above the baseline run would be less than twice the hydrogen production of the X run above the baseline run.

Calculating the integrals of the corrected corrosion rate curves determined that the baseline run produced 2.33 mmol H₂, the X run produced 3.21 mmol H₂ and the 2X run produced 4.21 mmol H₂ after 200 h of corrosion. Therefore, the addition of 43 mL of oxygen increased the hydrogen production by 0.88 mmol above the baseline hydrogen production and the addition of 86 mL of oxygen increased the hydrogen production by 1.88 mmol above the baseline hydrogen production. In other words, the increase in hydrogen production of the 2X run above the baseline run was 2.14 times the increase in hydrogen production of the X run above the baseline run. Hydrogen production of the 2X run above the baseline run that is approximately twice the hydrogen production of the X run above the baseline run indicates that no gaseous reduction of iron oxides occurred within the reaction cells. Figure 3.13 indicates that the increased hydrogen evolution rate of the 2X corrosion run above the baseline was essentially twice the increased hydrogen evolution rate of the X corrosion run above the baseline for the entire duration of the 200 h reaction.

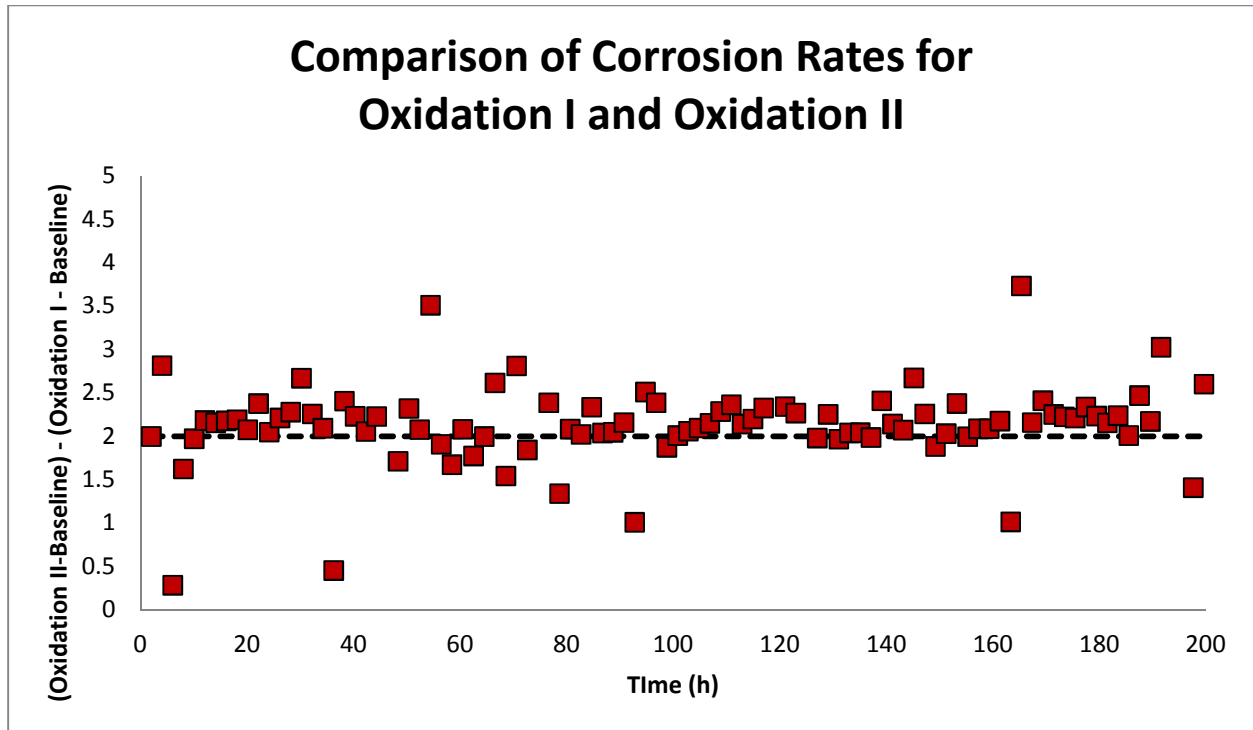
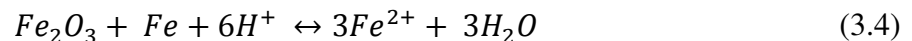


Figure 3.13: The hydrogen evolution rate of the 2X corrosion run above the baseline run was approximately twice the hydrogen evolution rate of the X corrosion run above the baseline run for the entire duration of the 200 h reaction. This indicates no hydrogen consumption by iron oxide reduction.

The results indicate that gaseous reduction of iron oxides did not occur during the Alfa Aesar iron corrosion experiments. However, iron oxide reduction occurs in iron/water systems through another process known as reductive dissolution:



Reductive dissolution of iron oxides was proposed by Odziemkowski and Gillham (1997) and Ritter et al. (2002) to explain the decrease in the presence of ferric oxides such as hematite, limonite, goethite and maghemite and the increase in the presence of the ferric/ferrous oxide magnetite during contact between iron and aqueous solutions. Whether the presence of hydrogen gas accelerates the reductive dissolution process has not previously been investigated.

For reductive dissolution to occur, H^+ must be present in the solution. A small amount of H^+ may form by the dissociation of water in iron-water systems, however the majority of the H^+ is formed from the dissociation of hydrogen gas. For hydrogen gas to produce H^+ , anionic

impurities must exist in the iron to charge balance the produced H^+ . In pure irons, such as Alfa Aesar iron (99.98% Fe), significant H^+ production would not occur from the dissociation of $H_{2(g)}$ due to the absence of anodic impurities. Therefore hydrogen treatment would likely not influence the reductive dissolution reaction on pure irons. However, irons such as H₂OmetTM56 and Connelly iron contain anionic impurities such as S, P and Cl. Therefore, it is possible that H^+ would be formed in a solution with these irons from the dissociation of $H_{2(g)}$. For irons with anionic impurities, hydrogen treatment may influence the reductive dissolution reaction and therefore the surface film properties and corrosion rate of the irons. The results of the iron oxidation experiments suggest that gaseous iron oxide reduction does not occur during iron corrosion at ambient temperatures, however further work is required to evaluate the effect of hydrogen treatment on the reductive dissolution reaction.

3.3.6 Hydrogen Induced Pitting

Hydrogen induced pitting corrosion has been well documented in corrosion literature (Li et al., 2012, Glowacka et al., 2006, Yu et al., 2002 and others) and is another possible effect of hydrogen on iron corrosion rate. Pitting corrosion is a localized type of corrosion in which a hole develops in an otherwise unaffected portion of oxide film leading to a deep opening in the protective surface coating (Schweitzer, 2010). Researchers believe that hydrogen enhances the pitting of metals by decreasing the stability of the passive film (Li et al., 2012).

Microscope images of low treated (left) and high treated (right) Connelly iron (Figure 3.14) depict the presence of more exposed bare iron metal on the high treated iron than the low treated iron. Hydrogen induced pitting corrosion is a possible explanation.



Figure 3.14: Microscope image of low-treated (left) and high-treated (right) Connolly iron. More areas of exposed iron metal are observed on Connolly iron that was treated under high hydrogen pressure conditions than on Connolly iron that was treated under low hydrogen pressure conditions. This is indicative of hydrogen induced pitting corrosion.

Areas of exposed bare iron metal on the high treated Connolly iron should increase the corrosion rate of the high treated iron compared to the low treated iron as a result of more exposed areas for direct electron transfer. However, no significant difference was observed between low and high treated Connolly iron corrosion rates (Figure 3.6).

In a previous investigation, Reardon (1995) investigated the effect of the addition of chloride salts, another species known to induce pitting, on the corrosion rates of Master Builders iron and found that the corrosion rates decreased with increasing chloride concentration. These results appeared to contradict extensive literature that chloride induces pitting and therefore should cause an increase in corrosion rate. Reardon (1995) argued that corrosion rate does not increase as a result of pitting corrosion because pitting corrosion is a type of *localized* corrosion which does not influence corrosion rate as significantly as *uniform* corrosion. The same can be argued here. Although a review of the literature and the physical appearance of the Connolly granules

indicate that hydrogen treatment induced pitting corrosion, the effect of hydrogen induced pits is small compared to the overall *uniform* corrosion of the iron granules and an increase in the high treated corrosion rate did not appear to occur as a result of pitting.

3.3.7 Implications for PRB Design

The results indicate that sustained contact with high pressures of hydrogen may have accelerated the iron dissolution-precipitation reaction on some irons by the process of hydrogen enhanced anodic dissolution. Hydrogen enhanced anodic dissolution appeared to cause rapid formation of corrosion species which reduced the post-treatment corrosion rate of some hydrogen treated irons.

The formation of corrosion species on reactive iron materials has traditionally been considered a hindrance on the reaction capabilities of the iron by reducing the rate of the electron transfer reaction (Liou et al., 2005, Klausen, 2001). However, the effect of surface films on the efficiency of the remediation reaction depends on the target contaminant. Some metal contaminants are treated through immobilization by surface complexation reactions with (hydr)oxide films (Henderson and Demond, 2007, Klausen, 2001). Certain oxide films can increase the metal surface area by orders of magnitude and create favourable conditions for contaminant adsorption (Klas and Kirk, 2013). Therefore, although hydrogen treatment increases the rate of surface film formation and decreases the corrosion rate of certain irons, increased surface film formation may be favourable to the remediation reaction depending on the target contaminant.

The initial oxide film characteristics of the iron material are also important to consider when evaluating the effects of hydrogen treatment on the remediation reaction. If the iron of interest is bare iron (Alfa Aesar) or contains a discontinuous oxide film (H₂OmetTM56), hydrogen is able to accumulate in the iron which may allow hydrogen enhanced anodic dissolution to occur.

Hydrogen enhanced anodic dissolution may enhance the dissolution-precipitation process and create a more extensive oxide film which slows the corrosion reaction. However, on irons with a continuous oxide film (Connelly), hydrogen enhanced anodic dissolution may be inhibited by the oxide film and the effects of hydrogen treatment may be less important.

Hydrogen pressures similar to those used in this study are reached within the PRB environment depending on the iron corrosion rate, the groundwater flow rate through the PRB and the depth

below the water table. Assuming a PRB thickness of 50 cm, porosity of 0.6 and an iron density of 6.7 g/cm^3 , Reardon (1995) determined that hydrogen pressures within a Connelly iron PRB can exceed 300 kPa for groundwater flow rates less than 5 cm/d. Since Connelly iron is highly oxidized, it corrodes more slowly than most granular irons used in PRBs. Therefore, under the same conditions, PRBs containing most other irons would reach hydrogen pressures in exceedance of 300 kPa.

Ventilation is a possible approach for mitigating the effects of hydrogen buildup in PRBs (Zhang and Gillham, 2005). Ventilation could maintain hydrogen pressures in the PRB that are favourable for certain surface film developments. However, whether PRB ventilation would be beneficial to the remediation reaction depends on several factors such as the target contaminants, initial properties of the iron and the confining pressures of the PRB. Further research is required to fully understand the effects of hydrogen on iron corrosion and reactivity before field-scale application of this knowledge is possible.

3.4 Conclusion

After 14 d of sustained hydrogen contact, corrosion rates were collected for two irons, H₂OmetTM56 iron and Connelly iron. The post-treatment corrosion rate of low treated H₂OmetTM56 iron was a factor of two higher than the post-treatment corrosion rate of high treated H₂OmetTM56 iron. The post-treatment corrosion rates of low and high treated Connelly iron were not statistically different.

SEM images of low and high-treated H₂OmetTM56 iron taken after the corrosion experiments revealed the presence of tubercles and a more uniform oxide film on the high treated sample compared to the low treated sample. These features suggest that the high treated H₂OmetTM56 iron reached a more advanced stage of iron corrosion than the low treated iron in the same time period.

Hydrogen enhanced anodic dissolution is a possible explanation for the lower corrosion rate of and the more advanced stage of corrosion observed in the SEM images for high treated H₂OmetTM iron. Experiments conducted using 99.98% Alfa Aesar iron supported an explanation based on hydrogen enhanced anodic dissolution. The observation that the post-treatment corrosion rate of high treated Connelly iron did not differ significantly from low treated Connelly

iron was attributed to the presence of a continuous oxide film on Connelly iron that prevented hydrogen from accumulating in the iron metal and causing hydrogen enhanced anodic dissolution.

No evidence for gaseous reduction of iron oxides was provided by experiments with Alfa Aesar iron. High hydrogen pressures may accelerate the reductive dissolution of iron oxides on irons with anionic impurities such as H₂Omet™ 56 and Connelly iron, however further research is required to evaluate the effect of hydrogen treatment on the reductive dissolution reaction. Hydrogen induced pitting corrosion was observed on Connelly iron but the influence of the hydrogen induced pits on the iron corrosion rate were negligible compared to the uniform corrosion rate of the iron.

Knowledge of how sustained hydrogen contact can affect the corrosion properties of iron is important to understanding the performance of PRBs. Hydrogen treatment may be favourable or unfavourable to the remediation reaction depending on the mechanism of target contaminant removal, initial characteristics of the oxide film and confining pressures of the PRB. Ventilation of the PRB to reduce hydrogen pressures is a possible approach for mitigating the effect of hydrogen on iron corrosion rate. Further research is required to more completely understand the effect of hydrogen pressure on iron corrosion rates before this knowledge can be applied in PRB performance considerations.

4 SUMMARY OF CONCLUSIONS

Hydrogen gas produced by anaerobic corrosion of iron can impart significant changes on the performance of permeable reactive barriers. The majority of studies investigating the effect of hydrogen gas on PRB performance have focused on the physical effects of hydrogen on PRBs such as changes to PRB porosity and permeability. In addition, hydrogen may chemically affect the reactivity of iron granules. The purpose of this thesis was to investigate hydrogen absorption into iron and changes to iron corrosion rates caused by hydrogen-iron interactions.

The absorption of hydrogen into iron may benefit PRB performance by preventing hydrogen from escaping the PRB and creating a stored electron resource within the iron that may be used in remediation reactions. To date, hydrogen absorption by granular irons has been largely unexplored in PRB performance investigations. In this study, factors governing hydrogen absorption by granular irons were investigated using corrosion rates developed from hydrogen evolution experiments in closed reaction vessels. The rate of hydrogen absorption was found to be related to the overall corrosion rate of the iron as indicated by a linear relationship between k and corrosion rate. This relationship between k and corrosion rate was attributed to accumulation of hydrogen at iron granule surfaces as a result of the rate of hydrogen production exceeding the rate of hydrogen diffusion. The presence of an oxide film was found to influence the proportion of hydrogen absorption with more oxidized irons absorbing higher proportions of hydrogen than irons with bare surfaces.

Preliminary investigations into ultrasound for the removal of lattice stored hydrogen indicated that ultrasonic treatment was not effective at releasing hydrogen from H₂OmetTM56 iron however, temperature fluctuations caused by the cavitation process introduced challenges in interpreting the corrosion rate data.

The effect of hydrogen on iron corrosion rates was also evaluated. Treatment of iron granules under high pressures of hydrogen for 14 d reduced the corrosion rate of H₂OmetTM56 iron and did not change the corrosion rate of Connelly iron. Hydrogen enhanced anodic dissolution is a possible explanation for the observed effect of hydrogen on H₂OmetTM56 iron corrosion rates. The extensive ferric oxide film on Connelly iron appears to have prevented hydrogen from penetrating to the iron surface and inhibited the effect of hydrogen enhanced anodic dissolution. No evidence for the reduction of iron oxides by hydrogen gas was observed but reductive

dissolution of iron oxides remains a possible influence of hydrogen on iron corrosion rates. Hydrogen induced pitting corrosion was observed in microscope images of Connelly iron but did not appear to influence the overall corrosion rate of the iron.

Strategies for managing the effects of hydrogen on iron corrosion rates on a field scale depend on several factors including the initial oxide film characteristics of the iron and the removal mechanism for the target contaminant. The effect of hydrogen on corrosion rate is more pronounced on irons with exposed iron metal than irons covered in a continuous oxide film due to inhibition of hydrogen enhanced anodic dissolution by the oxide film. If hydrogen enhanced anodic dissolution occurs, increased oxide film precipitation results. This can be beneficial to the remediation reaction if the target contaminant is treated by surface complexation reactions, as is the case for some metals, because oxide film growth enhances the surface area of the reactive medium. Ventilation of the PRB to remove accumulated hydrogen is one possible method of maintaining conditions within the PRB that are advantageous to the groundwater treatment process.

5 RECOMMENDED FUTURE WORK

An important area of further work is to investigate whether the observed relationship between k and corrosion rate applies generally to a spectrum of granular iron materials. Better understanding of this relationship could assist in developing a universal equation for removal of discontinuities from corrosion rate curves and provide a better understanding of how hydrogen absorption by iron is affected by the rate of hydrogen gas production.

Further research should also be conducted on methods of hydrogen release from iron.

Preliminary investigations into ultrasonic treatment demonstrated that ultrasonic methods were not effective at releasing hydrogen from H₂Omet™56 however additional experiments making use of different irons and different ultrasonic frequencies could prove useful. Methods allowing for improved control of temperature fluctuations under ultrasonic treatment conditions should be considered. Ongoing work on hydrogen release should also include an investigation of chemical and microbiological methods of hydrogen release.

Questions also remain regarding the effects of hydrogen treatment on iron corrosion rates. Of particular interest is whether reductive dissolution of iron oxides is enhanced in the presence of hydrogen. In addition, further hydrogen treatment experiments making use of different iron materials could prove useful in understanding how irons with different physicochemical properties are affected by hydrogen treatment.

Significant further research is required to better understand the effects of hydrogen on iron reactivity in PRB systems. An understanding of these effects would be of great assistance in promoting PRBs as the preferred solution for long-term groundwater treatment challenges.

Appendix A - Materials

H₂Omet™56 Iron



Figure A1: Physical appearance of H₂Omet™56

Table A1: Particle size distribution for H₂Omet™56 iron.

U.S. mesh	+30	+70	+200	-200
μm	+600	+212	+75	-75
wt%	<1	45	40	14

Table A2: Chemical composition of H₂Omet™56 iron.

	C	O	S	P	Mn	Si	V	Ti	Cu	Fe
H ₂ Omet™56	3.2	2.6	0.01	0.01	0.01	0.01	0.02	0.02	0.03	>93

H₂Omet™58 Iron



Figure A2: Physical appearance of H₂Omet™58

Table A3: Particle size distribution for H₂Omet™58 iron.

U.S. mesh	+12	+30	+50	+100	+200	+325	-325
µm	+1680	+600	+300	+150	+75	+45	-45
wt%	<1	19	35	25	14	3.5	2.8

Table A4: Chemical composition of H₂Omet™58 iron.

	C	O	S	P	Mn	Si	V	Ti	Cu	Fe
H ₂ Omet™58	3.2	3.0	0.01	0.01	0.01	0.01	0.02	0.02	0.03	>93

H₂Omet™86 Iron



Figure A3: Physical appearance of H₂Omet™86.

Table A5: Particle size distribution for H₂Omet™86 iron.

U.S. mesh	+60	+100	+200	+325	-325
μm	+250	+150	+75	+45	-45
wt%	<1	6	49	24	21

Table A6: Chemical composition of H₂Omet™86 iron.

	C	O	S	P	Mn	Si	V	Ti	Cu	Fe
H ₂ Omet™86	0.05	0.18	0.01	0.01	0.01	0.01	0.02	0.02	0.03	>99

Connelly Iron



Figure A4: Physical appearance of Connelly iron.

Alfa Aesar Iron



Figure A5: Physical appearance of Alfa Aesar (99.98%) iron.

Appendix B - Reaction Apparatus



Figure B1: Stainless steel reaction vessel outfitted with Swagelok fittings.



Figure B2: Omega pressure transducer used to monitor pressure changes.

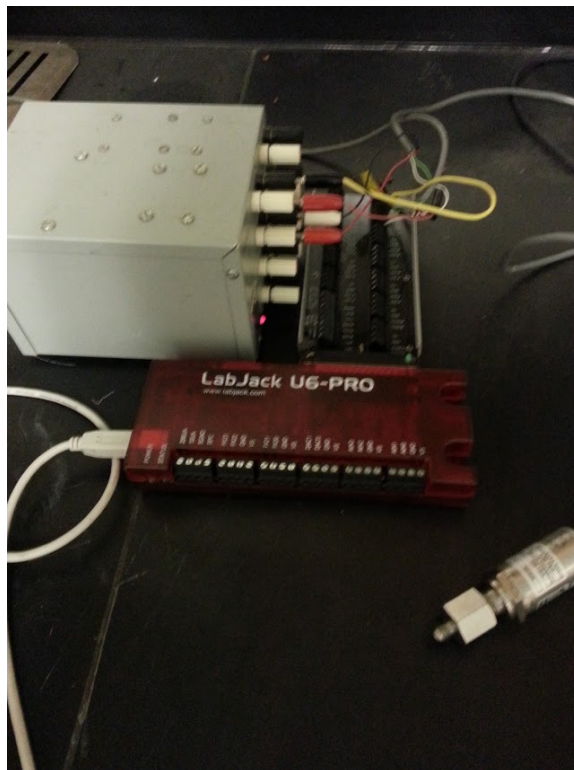


Figure B3: LabJack U6-PRO data acquisition board.

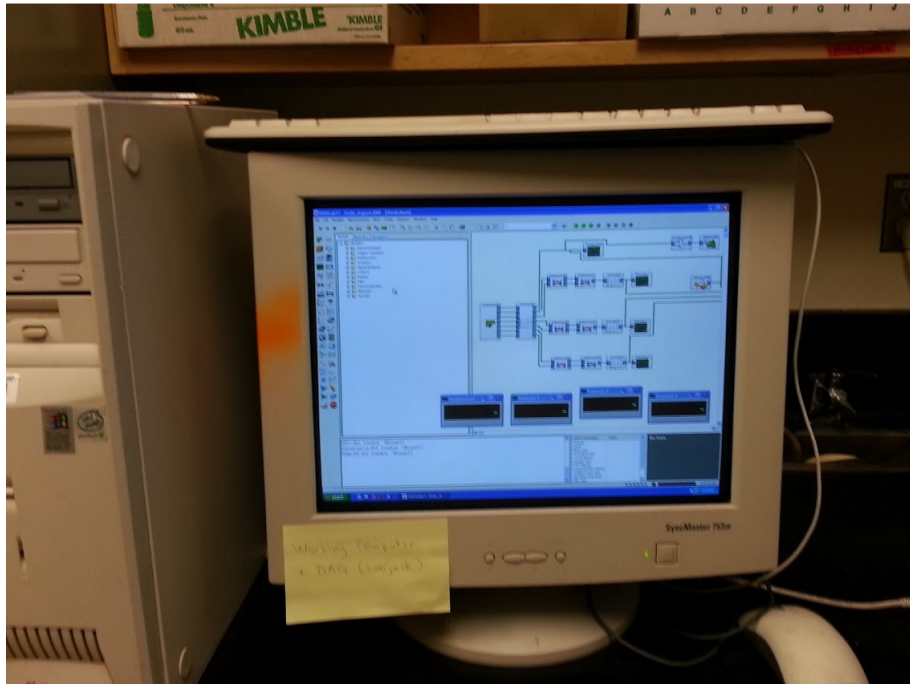


Figure B4: DASyLab v. 11.0 data acquisition software.

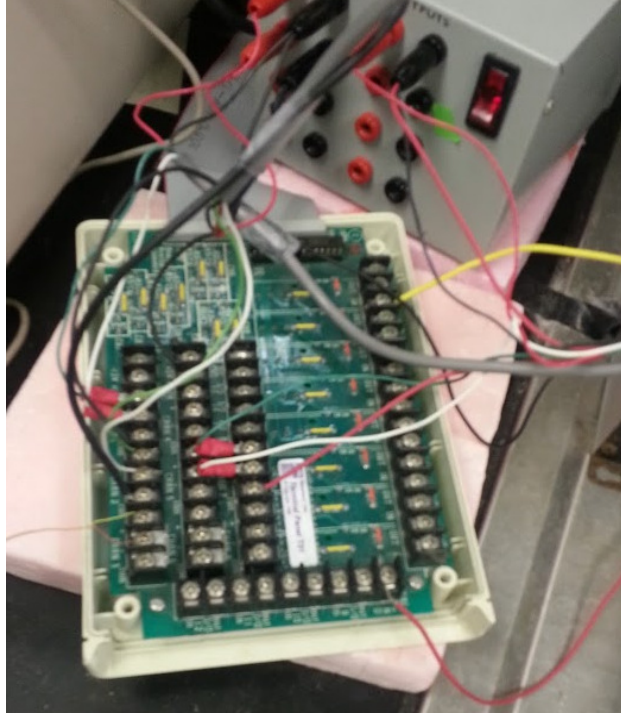


Figure B5: Strawberry Tree 16-bit data acquisition board.

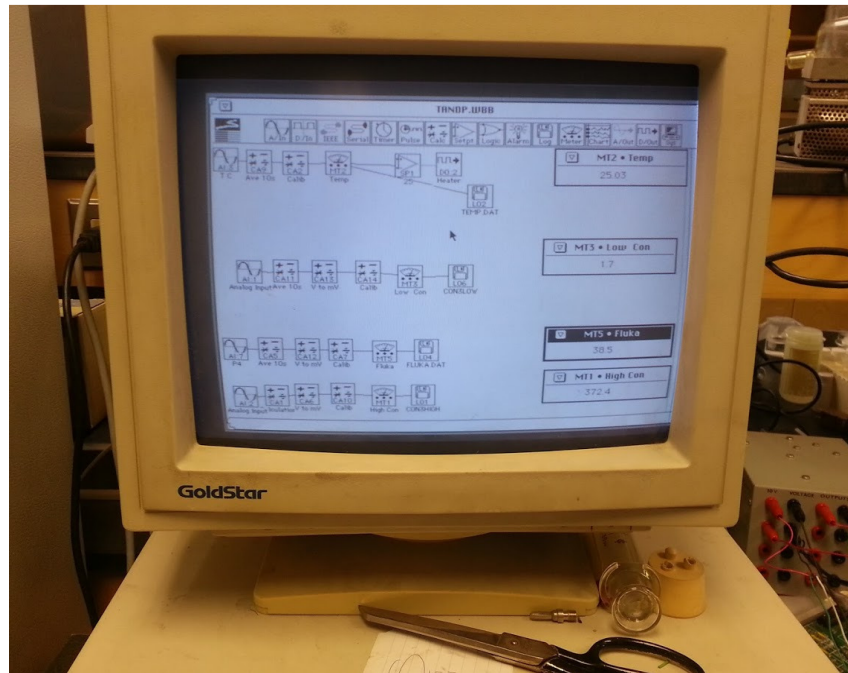


Figure B6: WorkBench PC v. 2.3.1 data acquisition software.

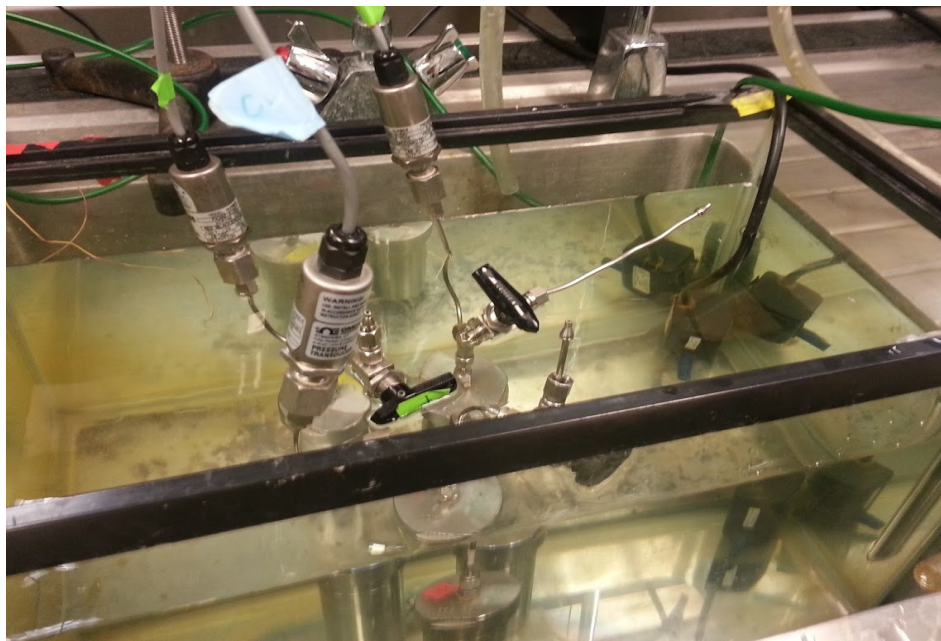


Figure B7: Constant temperature bath used to maintain reaction cells at $25 \pm 0.1^\circ\text{C}$.

Appendix C - Chapter 2.0 Supplemental Information

Table C1: Table of values used for k versus corrosion rate relationship.

Iron Material	k (mmol kg⁻¹ d⁻¹ kPa^{-0.5})	R_{corr} (mmol kg⁻¹ d⁻¹)
<i>H₂Omet</i> TM 56	0.13	2.011
<i>H₂Omet</i> TM 58	0.30	7.352
	0.40	9.855
	0.35	8.486
<i>H₂Omet</i> TM 86	0.39	12.020
	0.47	14.384
	0.56	18.463
	0.69	23.100
	0.82	27.768
	1.0	32.781

Table C2: Student's t-test for H₂OmetTM56 iron ($k = 0.13 \text{ mmol kg}^{-1} \text{ d}^{-1} \text{ kPa}^{-0.5}$).

$n_1 =$	12
$n_2 =$	12
$x_1 =$	2.163526
$x_2 =$	2.253593
$\sigma_1 =$	0.27736
$\sigma_2 =$	0.364369
$\sigma_1^2 =$	0.076929
$\sigma_2^2 =$	0.132765
$\sigma_d^2 =$	0.017474
$\sigma_d =$	0.132191
$t =$	0.681341
Tabulated T Value ($p=0.05$)	2.07
Calculated T Value	0.681

Table C3: Student's t-test for H₂OmetTM58 iron ($k = 0.30 \text{ mmol kg}^{-1} \text{ d}^{-1} \text{ kPa}^{-0.5}$).

$n_1 =$	12
$n_2 =$	12
$x_1 =$	7.717068
$x_2 =$	7.755198
$\sigma_1 =$	0.126154
$\sigma_2 =$	0.146483
$\sigma_1^2 =$	0.015915
$\sigma_2^2 =$	0.021457
$\sigma_d^2 =$	0.003114
$\sigma_d =$	0.055806
$t =$	0.683247
Tabulated T Value ($p=0.05$)	2.07
Calculated T Value	0.683

Table C4: Student's t-test for H₂OmetTM86 iron ($k = 0.39 \text{ mmol kg}^{-1} \text{ d}^{-1} \text{ kPa}^{-0.5}$).

$n_1 =$	12
$n_2 =$	12
$x_1 =$	12.40988
$x_2 =$	12.45784
$\sigma_1 =$	2.046613
$\sigma_2 =$	4.856258
$\sigma_1^2 =$	4.188624
$\sigma_2^2 =$	23.58324
$\sigma_d^2 =$	2.314322
$\sigma_d =$	1.52129
$t =$	0.031523
Tabulated T Value ($p=0.05$)	2.07
Calculated T Value	0.032

Appendix D - Chapter 3.0 Supplemental Information

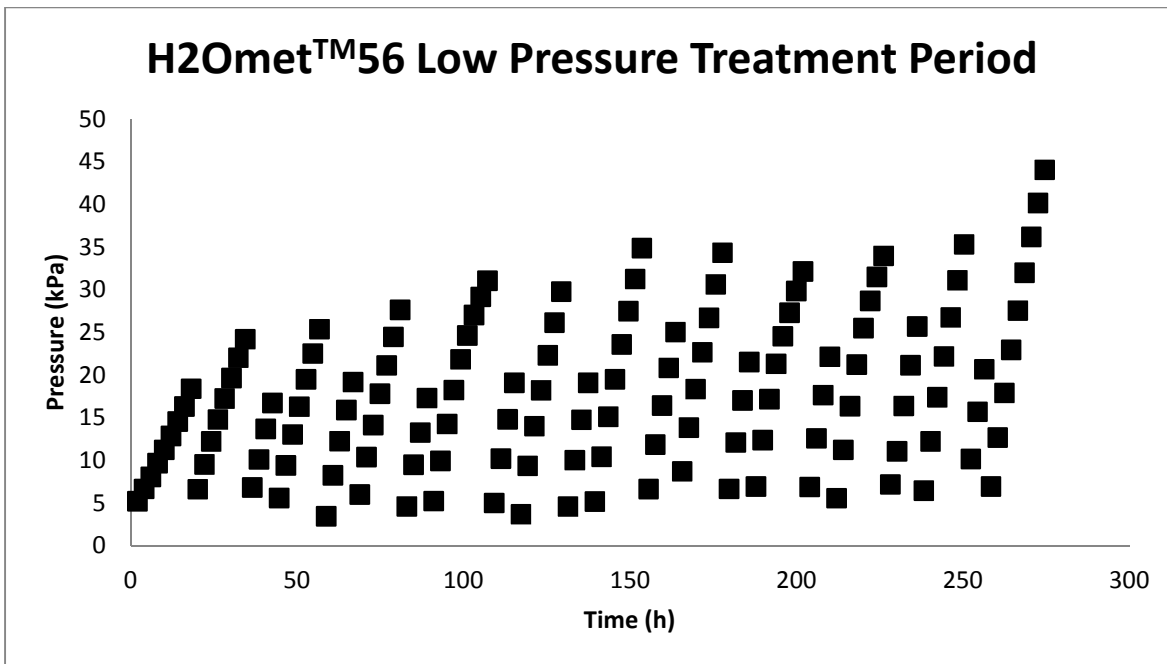


Figure D1: H₂Omet™56 low pressure treatment period for hydrogen treatment corrosion experiments. Pressures were maintained below 45 kPa.

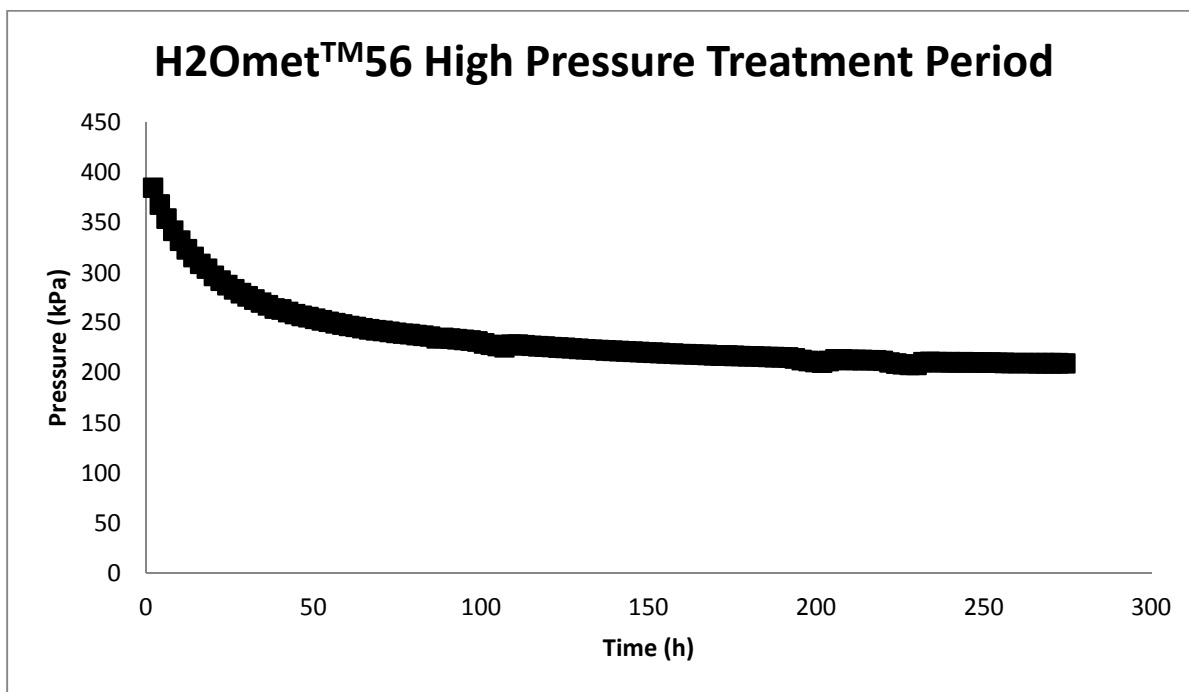


Figure D2: H₂Omet™56 high pressure treatment period for hydrogen treatment corrosion experiments. Pressures were maintained above approximately 200 kPa.

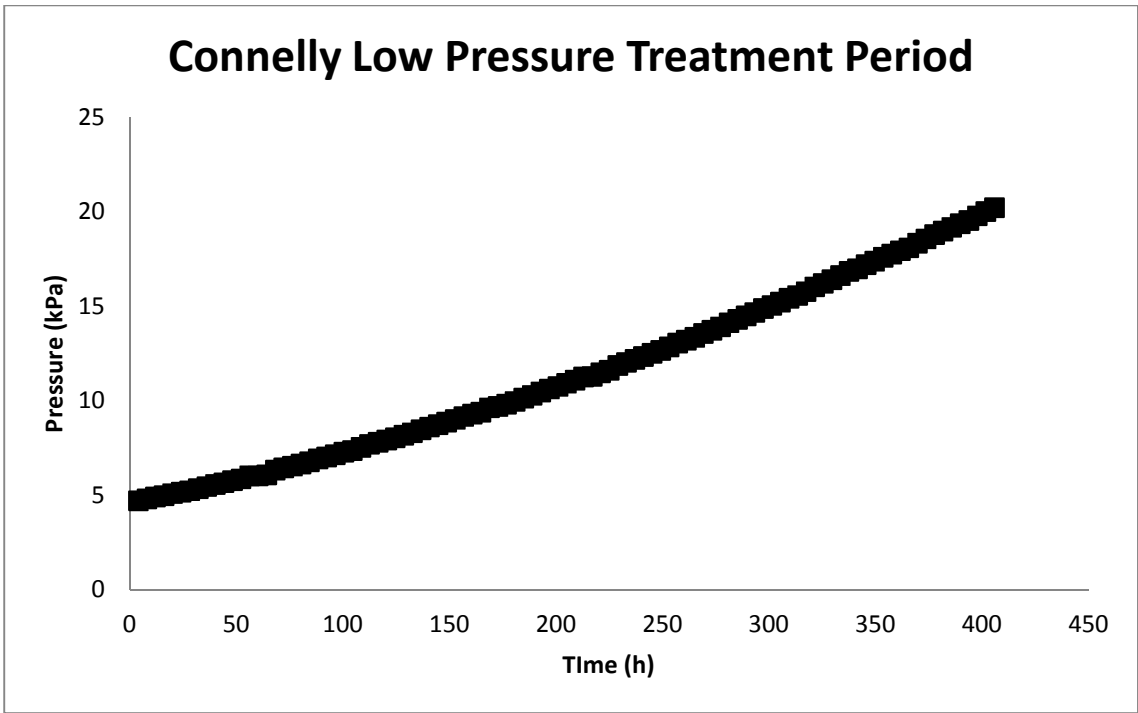


Figure D3: Connelly low pressure treatment period for hydrogen treatment corrosion experiments. Pressures were maintained below 20 kPa.

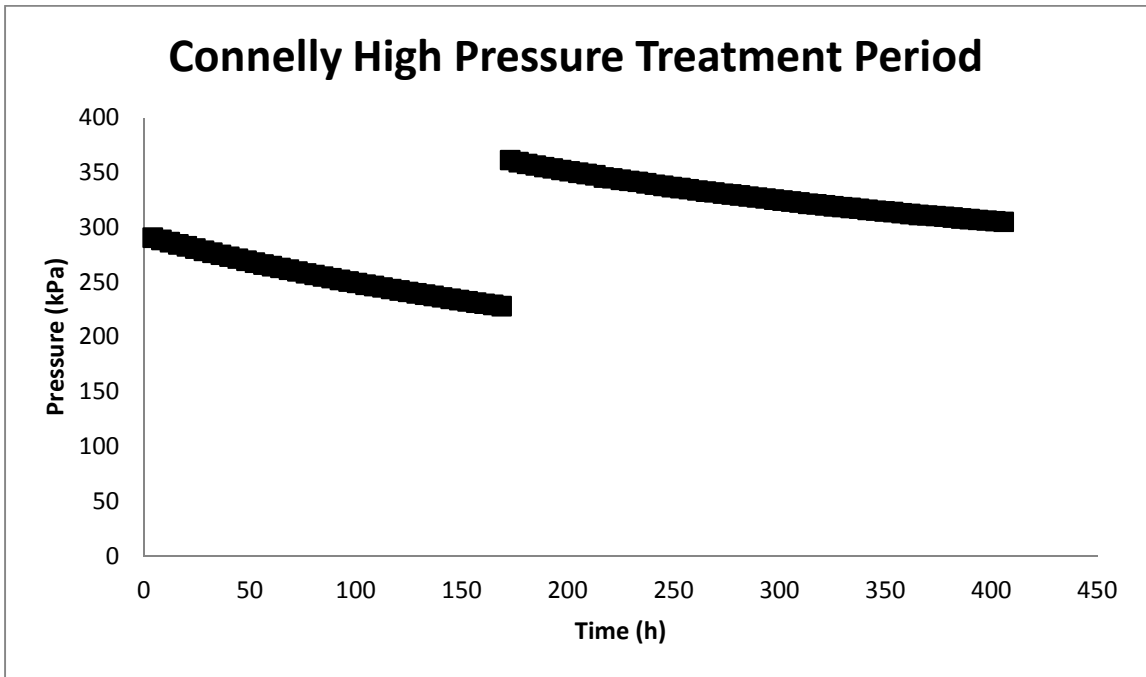


Figure D4: Connelly high pressure treatment period for hydrogen treatment corrosion experiments. Pressures were maintained above approximately 200 kPa.

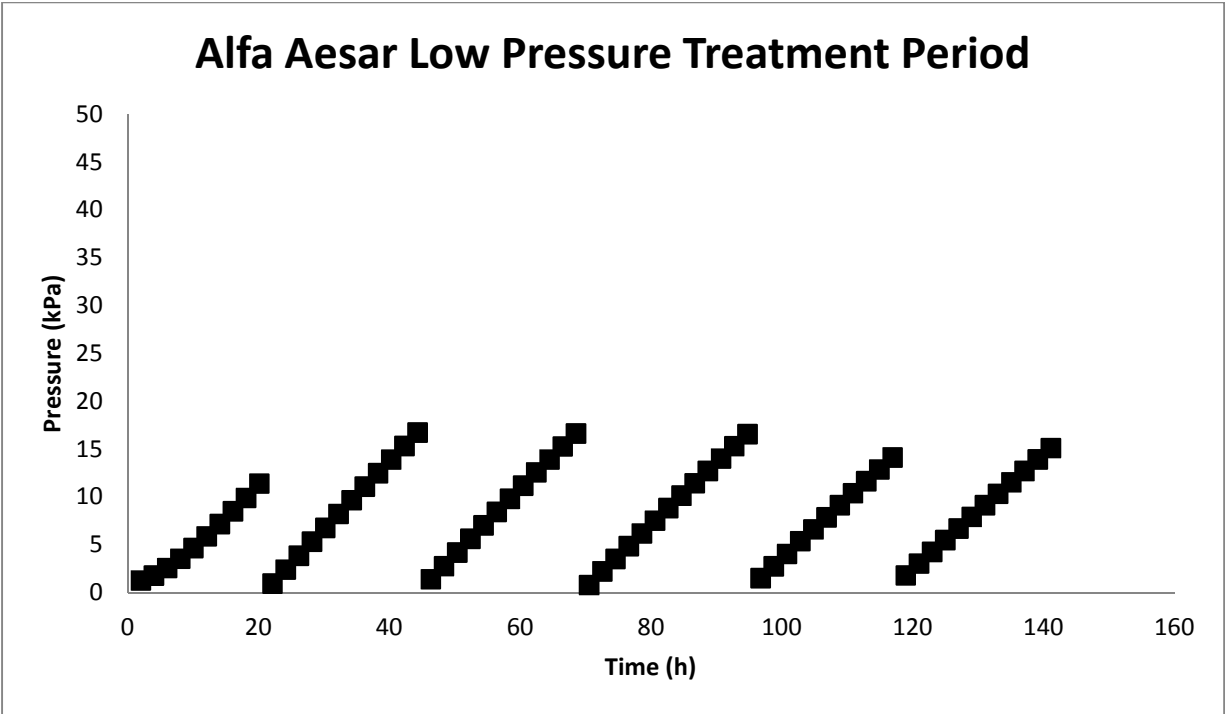


Figure D5: Alfa Aesar low pressure treatment period for hydrogen treatment corrosion experiments. Pressures were maintained below 20 kPa.

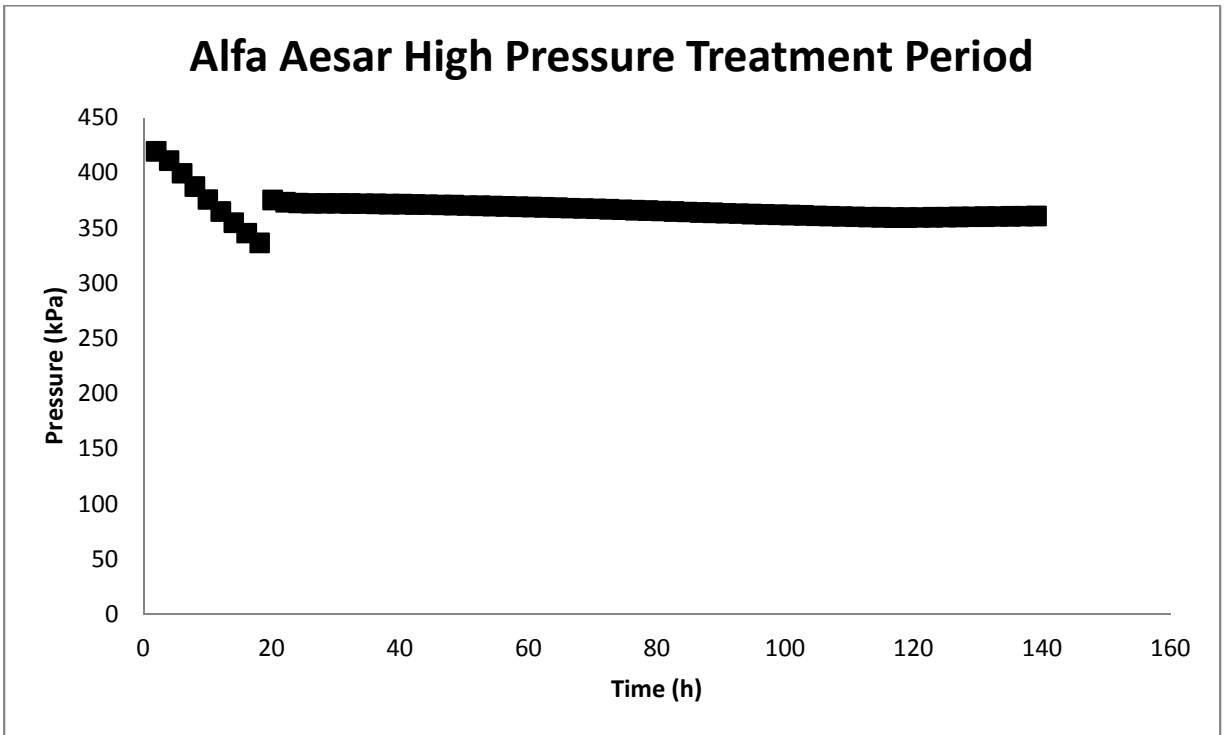


Figure D6: Alfa Aesar high pressure treatment period for hydrogen treatment corrosion experiments. Pressures were maintained above 350 kPa.

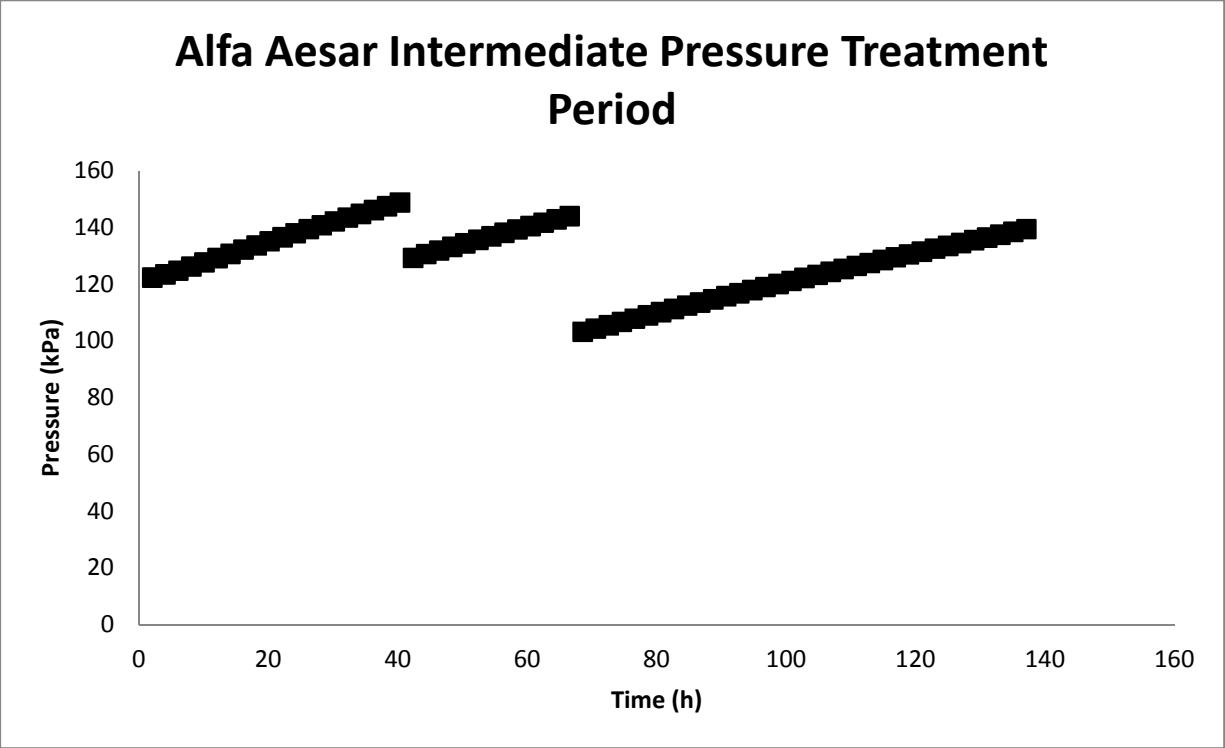


Figure D7: Alfa Aesar intermediate pressure treatment period for hydrogen treatment corrosion experiments. Pressures were maintained below 150 kPa and above 100 kPa.

References

- Amos, R.T. and K.U. Mayer. 2006. Investigating the role of gas bubble formation and entrapment in contaminated aquifers: Reactive transport modelling. *Journal of Contaminant Hydrogeology*, **87**(1-2), 123-154.
- Blowes, D.W., C.J. Ptacek, S.G. Benner, C.W.T. McRae, T.A. Bennett and R.W. Puls. 2000. Treatment of inorganic contaminants using permeable reactive barriers. *Journal of Contaminant Hydrology*, **45**(1-2), 123-137.
- Cantrell, K.J., D.I. Kaplan and T.W. Wietsma. 1995. Zero-valent iron for the in situ remediation of selected metals in groundwater. *Journal of Hazardous Materials*, **42**(2), 201-212.
- Choo, W.Y. and J.Y. Lee. 1982. Thermal analysis of trapped hydrogen in pure iron. *Metallurgical and Materials Transactions*. **13**(1), 135-140.
- Dafft, E.G., K. Bohnenkamp and H.J. Engell. 1979. Investigations of the hydrogen evolution kinetics and hydrogen absorption by iron electrodes during cathodic polarization. *Corrosion Science*. **19**(7), 591-612.
- Dan, T., T. Shoji, Z. Lu, K. Sakaguchi, J. Wang, E.-H Han and W. Ke. 2010. Effects of hydrogen on the anodic behaviour of Alloy 690 at 60⁰C. *Corrosion Science*. **52**, 1228-1236.
- Foroulis, Z.A. 1979. The influence of velocity and dissolved oxygen on the initial corrosion behaviour of iron in high purity water. *Corrosion*. **35**(8), 340-344.
- Gandhi, S., B.-T. Oh, J.L. Schnoor and P.J.J. Alvarez. 2002. Degradation of TCE, Cr(VI), sulfate and nitrate mixtures by granular iron in flow-through columns under different microbial conditions. **36**(8), 1973-1982.
- Geiger, C.L., C.A. Clausen, D.R. Reinhart, C.M. Clausen, N. Ruiz and J. Quinn. 2003. Using ultrasound for restoring iron activity in permeable reactive barriers, in: S.M. Henry, S.D. Warner (Eds), Chlorinated Solvent and DNAPL Remediation: Innovative Strategies for Subsurface Cleanup, American Chemical Society: Distributed by Oxford University Press, Washington, DC, pp. 86-303.

- Gillham, R.W. and S.F. O'Hannesin. 1994. Enhanced degradation of halogenated aliphatics by Zero-valent iron. *Groundwater*, **32**(6), 958-967.
- Glowacka, A., M.J. Wozniak, G. Nolze, W.A. Swiatnicki. 2006. Hydrogen induced phase transformations in austenitic-ferritic steel. *Solid State Phenomena*. **112**, 133-140.
- Gong, C. and D. P. Hart. 1998. Ultrasound induced cavitation and sonochemical yields. *Journal of the American Chemical Society*, **104**(5), 2675-2682.
- Gu, B., J. Luo and X. Mao. 1999. Hydrogen-facilitated anodic dissolution-type stress corrosion cracking of pipeline steels in near-neutral pH solution. *Corrosion*. **55**(1), 97-106.
- H₂OmetTM: Groundwater Remediation the Natural Way. 2010. *H₂OmetTM Manufacturing Process*. Retrieved from <http://www.h2omet.com/en/page.ch2?uid=Technology>.
- Henderson, A.D. and A.H. Demond. 2011. Impact of solids formation and gas production on the permeability of ZVI PRBs. *Journal of Environmental Engineering*, (**137**), 689-696.
- Henderson, A.D. and A.H. Demond. 2007. Long-term performance of zero-valent iron permeable reactive barriers: A critical review. *Environmental Engineering Science*, **24**(4), 401-423.
- Hirth, J.P. 1980. Effects of hydrogen on the properties of iron and steel. *Metallurgical and Materials Transactions*. **11**(6), 861-890.
- Huang, Y., F.-Z. Xuan, S.-T. Tu and T. Itoh. 2011. Effects of hydrogen and surface dislocation on active dissolution of deformed 304 austenitic stainless steel in acid chloride solution. *Materials Science and Engineering*. **A 528**, 1882-1888.
- Isselin, J., R. Kasada and A. Kimura. 2011. Work hardening, sensitization and potential effects on the susceptibility to crack initiation of 316L stainless steel in BWR environment. *Journal of Nuclear Science and Technology*. **48**(12), 1462-1470.
- Iyer, R.N. and H.W. Pickering. 1990. Mechanism and kinetics of electrochemical hydrogen entry and degradation of metallic systems. *Annual Reviews of Materials Science*. **20**, 299-338.

- Jeen, S.-W., R.T. Amos and D.W. Blowes. 2012. Modeling gas formation and mineral precipitation in a granular iron column. *Environmental Science and Technology*, **46**, 6742-6749.
- Jeen, S.-W., R.W. Gillham and D.W. Blowes. 2006. Effects of carbonate precipitates on long-term performance of granular iron for reductive dechlorination of TCE. *Environmental Science and Technology*, **40**(20), 6432-6437.
- Johnson, H.H. 1988. Hydrogen in iron. *Metallurgical and Materials Transactions*. **19**(10), 2371-2387.
- Klas, S. and D.W. Kirk. 2013. Advantages of low pH and limited oxygenation in arsenite removal from water by zero-valent iron. *Journal of Hazardous Materials*. **252-253**, 77-82.
- Klausen, J., J. Ranke, and R.P. Schwarzenbach. 2001. Influence of solution composition and column aging on the reduction of nitroaromatic compounds by zero valent iron. *Chemosphere*. **44**, 511-517.
- Li, M., L.Q. Guo, L.J. Qiao and Y. Bai. 2012. The mechanism of hydrogen-induced pitting corrosion in duplex stainless steel studied by SKPFM. *Corrosion Science*. **60**, 78-81.
- Lien, H.-L. and R.T. Wilkin. 2005. High-level arsenite removal from groundwater by zero-valent iron. *Chemosphere*, **59**(3), 377-386.
- Liou, Y.H., S.-L. Lo, C.-J. Lin, W.H. Kuan and S.C. Weng. 2005. Effects of iron surface pretreatment on kinetics of aqueous nitrate reduction. *Journal of Hazardous Materials*. **B126**, 189-194.
- Mackenzie, P.D., D.P. Horney and T.M. Sivavec. 1999. Mineral precipitation and porosity losses in granular iron columns. *Journal of Hazardous Materials*, **68**(1-2), 1-17.
- Mao, S.X. and M. Li. 1998. Mechanics and thermodynamics on the stress and hydrogen interaction in crack tip stress corrosion: Experiment and Theory. *Journal of the Mechanics and Physics of Solids*. **46**(6), 1125-1137.

- Mason, T. J. and J. P. Lorimer. 1988. *Sonochemistry: theory, applications and uses of ultrasound in chemistry*. Chichester, West Sussex, England: Ellis Horwood Limited.
- Matheson, L.J. and P.G. Tratnyek. 1994. Reductive dehalogenation of chlorinated methanes by iron metal. *Environmental Science and Technology*, **28**, 2045-2053.
- National Research Council. 1994. *Alternatives for Ground Water Cleanup*. Washington, DC: National Academy Press.
- Ningshen, S., U. Kamachi Mudali, G. Amarendra, P. Gopalan, R.K. Dayal and H.S. Khatak. 2006. Hydrogen effects on the passive film formation and pitting susceptibility of nitrogen containing type 316L stainless steels. *Corrosion Science*. **48**, 1106-1121.
- Odziemkowski, M.S., T.T. Schumacher, R.W. Gillham and E.J. Reardon. 1998. Mechanism of oxide film formation on iron in simulating groundwater solutions: Raman spectroscopic studies. **40**(2/3), 371-389.
- Odziemkowski, M.S. and R.W. Gillham. 1997. Surface redox reactions on commercial grade granular iron (steel) and their influence on the reductive dechlorination of solvent. Micro raman spectroscopic studies. *213th ACS National Meeting, San Francisco, CA. Extended Abstracts Division of Environmental Chemistry*. **37**, 177-180.
- O'Hannesin, S.F. and R.W. Gillham. 1998. Long-term performance of an in situ "iron wall" for remediation of VOCs. *Groundwater*, **36**(1), 164-170.
- Oriani, R.A. 1993. *The physical and metallurgical aspects of hydrogen in metals*. in *ICCF4, Fourth International Conference on Cold Fusion*. 1993. Lahaina, Maui: Electric Power Research Institute 3412 Hillview Ave., Palo Alto CA 94304.
- Otsuka, Y., S. Nagaoka and Y. Mutoh. 2011. Effects of dissolved oxygen on fatigue characteristics of austenitic stainless steel in 0.9wt% sodium chloride solutions. *Procedia Engineering*. **10**, 1333-1338.
- Peden, C.H.F., B.D. Kay and D.W. Goodman. 1986. Kinetics of hydrogen absorption by chemically modified Pd(110). *Surface Science*. **175**, 215-225.

- Peing, T.P. and J.K. Wu. 2003. A brief note on mechanisms of hydrogen entry into metals. *Materials Letters*. **57**, 3437-3438.
- Peters, D. 1996. Ultrasound in materials chemistry. *Journal of Materials Chemistry*, **6**(10), 1605-1618.
- Pineau, A., N. Kanari and I. Gaballah. 2007. Kinetics of reduction of iron oxides by H₂ Part II. Low temperature reduction of magnetite. *Thermochimica Acta*. **456**, 75-88.
- Pineau, A., N. Kanari and I. Gaballah. 2006. Kinetics of reduction of iron oxides by H₂ Part I: Low temperature reduction of hematite. *Thermochimica Acta*. **447**, 89-100.
- Puls, R.W., C.J. Paul and R.M. Powell. 1999a. The application of in situ permeable reactive (zero-valent iron) barrier technology for the remediation of chromate-contaminated groundwater: A field test. *Applied Geochemistry*. **14**(8), 989-1000.
- Puls, R.W., D.W. Blowes and R.W. Gillham. 1999b. Long-term performance monitoring for a permeable reactive barrier at the U.S. Coast Guard Support Center, Elizabeth City, North Carolina. *Journal of Hazardous Materials*, **68**(1-2), 109-124.
- Qiao, L.J. and J.L. Luo. 1998. Hydrogen-facilitated anodic dissolution of austenitic stainless steels. *Corrosion*. **54**(4), 281-288.
- Reardon, E.J. 2013. Capture and storage of hydrogen gas by zero-valent iron.
- Reardon, E.J. 2005. Zerovalent irons: Styles of corrosion and inorganic control on hydrogen pressure buildup. *Environmental Science and Technology*. **39**(18), 7311-7317.
- Reardon, E.J. 1995. Anaerobic corrosion of granular iron: Measurement and interpretation of hydrogen evolution rates. *Environmental Science and Technology*. **29**, 2936-2945.
- Repta, C.J.W. 2001. Evaluation of nickel-enhanced granular iron for the dechlorination of trichloroethene. (Master's Thesis), Department of Earth Sciences, University of Waterloo, Waterloo, Ontario.

- Ritter, K., M.S. Odziemkowski, R.W. Gillham. 2002. An in situ study of the role of surface films on granular iron in the permeable iron wall technology. *Journal of Contaminant Hydrology*. **55**, 87-111.
- Robertson, W.D., J.L. Vogan and P.S. Lombardo. 2008. Nitrate removal rates in a 15-year-old permeable reactive barrier treating septic system nitrate. *Groundwater Monitoring & Remediation*. **28**(3), 65-72.
- Sarin, P., V.L. Snoeyink, D.A. Lytle and W.M. Kriven. 2004a. Iron corrosion scales: Model for scale growth, iron release, and coloured water formation. *Journal of Environmental Engineering*. **130**(4), 364-373.
- Sarin, P., V.L. Snoeyink, J. Bebee, K.K. Jim, M.A. Beckett, W.M. Kriven and J.A. Clement. 2004b. Iron release from corroded iron pipes in drinking water distribution systems: Effect of dissolved oxygen. *Water Research*. **38**, 1259-1269.
- Sastri, M.V.C, R.P. Viswanath and B. Viswanathan. 1982. Studies on the reduction of iron oxide with hydrogen. *International Journal of Hydrogen Energy*. **7**(12), 951-955.
- Schweitzer, P.A. 2010. *Fundamentals of Corrosion: Mecanisms, Causes and Preventative Methods*. Boca Raton, Florida: CRC Press.
- Sieverts, A. 1929. Absorption of gases by metals. *Zeitschrift fur Metallkunde*. **21**, 37-46.
- Suslick, K.S. and G. J. Price. 1999. Application of ultrasound to materials chemistry. *Annual Review of Materials Science*. **29**, 295-326.
- Timmins, P.F. 1997. *Solutions to hydrogen attack in steels*. Materials Park, Ohio, USA. ASM International.
- Thangavadivel, K., M. Megharaj, R.S. Smart, P.J. Lesniewski and R. Naidu. 2010. Sonochemical destruction of chloroform by using low frequency ultrasound in batch and flow cell. *Journal of Environmental Science and Health*, **45**(4), 483-489.

- Vogan, J.L., R.M. Focht, D.K. Clark and S.L. Graham. 1999. Performance evaluation of a permeable reactive barrier for remediation of dissolved chlorinated solvents in groundwater. *Journal of Hazardous Materials*, **68**(1-2), 97-108.
- Wagner, D., O. Devisme, F. Patisson and D. Ablitzer. 2006. A laboratory study of the reduction of iron oxides by hydrogen. *Sohn International Symposium, San Diego, CA*. **2**, 111-120.
- Was, G.S. and S.M. Bruemmer. 1994. Effects of irradiation on intergranular stress corrosion cracking. *Journal of Nuclear Materials*. **216**, 326-347.
- Wu, J.M., H.S. Huang and C.D. Livengood. 1995. Development of an ultrasonic process for soil remediation. Argonne, Illinois: Energy Systems Division.
- Yu, J.G., C.S. Zhang, J.L. Luo and P.R. Norton. 2003. Investigation of the effect of hydrogen on the passive film on iron by surface analysis techniques. *Journal of the Electrochemical Society*. **150**(2), B68-B75.
- Yu, J.G., J.L. Luo, P.R. Norton. 2002. Electrochemical investigation of the effects of hydrogen on the stability of the passive film on iron. *Electrochimica Acta*. **47**, 1527-1536.
- Zakroczymski, T. 1985. Entry of hydrogen into iron alloys from the liquid phase. In: Hydrogen Degradation of Ferrous Alloys. Oriani, R.A., J.P. Hirth and M. Smialowski (Eds) Noyes Publications, Park Ridge N.J., *Chapter 8*, pp 888.
- Zhang, Y. and R.W. Gillham. 2005. Effects of gas generation and precipitates on performance of Fe⁰ PRBs. *Groundwater*, **43**(1), 113-121.
- Zhao, C. 2010. The effect of H₂ gas treatment of granular iron on dehalogenation reactions (Bachelor's Thesis). Department of Earth and Environmental Science, University of Waterloo, Waterloo, Ontario.
- Zhao, C. and E.J. Reardon. 2012. H₂ gas charging of zero-valent iron and TCE degradation. *Journal of Environmental Protection*. **3**(3), 272-279.